THE UNIVERSITY *of* EDINBURGH

Structure and dynamics of filled liquid crystals.

Navneeta Katyan

Doctor of Philosophy
The University of Edinburgh
Dec 2019

Abstract

In the formulation world, rheological properties like flow behavior and viscoelastic response determine the quality of the product. For the first time, we explore and explain the dynamic response of filled nematic thermotropic liquid crystal phases. We then discuss the behavior in lyotropic filled nematic liquid crystalline (NLCs) media and compare it with the more commonly understood filled lamellar phases. Conventional rheometry, coupled with polarizing microscopy, was used to formulate an understanding of the microstructure of the colloids and their effect on the flow behavior of the colloids and LCs composite.

A class of soft solids exhibiting exceptional stability is made from dispersing PMMA microspheres in thermotropic nematic liquid crystal (NLCs). When a microsphere induces weak homeotropic anchoring in NLCs, the director around the colloid elastically distorts to accommodate the particle giving rise to disclinations or defect lines. The type of defect present depends on the anchoring strength, (W), between colloid and NLCs, the elasticity of the NLCs, (K), and the size of the dispersed particle, (r). For $\frac{Wr}{K} \ll 1$, the colloid induces a Saturn-ring defect in NLCs. These Saturn-ring defects remain isolated without interacting with each other in the dilute composite. As the concentration of the colloids in NLCs increases, the encircling loops of these Saturn-rings no longer remain isolated but entangle to form a more stable topological structure which holds the colloid in the defect matrix — thus forming a stable gel composite. Dynamic moduli of these composites increase with volume fraction with G' and $G'' \propto \phi^2$, possibly because each colloid supports a two-dimensional Saturn-ring. These ring defects can connect at different points around the circumference of the disclinations and therefore the number of percolating paths increases quadratically with the volume fraction. For the first time, we show that G'' $\propto \omega^{1/2}$ on yielding. We derive a theory that describes this yielding behaviour is governed by the Ericksen number, E_r, associated with confined nematic region

within the composites. We find that the frequency dependence of the composites is independent of the volume fraction, ϕ, indicating that it is neither an active or passive filled system and that the behavior of composite is determined by the intrinsic properties of the nematic phase. The colloids merely serve to create and support Saturn-ring defects.

The structure and dynamics of filled lyotropic NLCs were studied for the first time. Uncharged PMMA particles were dispersed in surfactant and water-based lyotropic mesophase to form a class of composites similar to the thermotropic system. Filled lyotropics exhibit similar rheological behavior to their thermotropic counterpart. However, the surface charge of colloids disrupts the composite properties in the charged micellar nematic liquid crystal system. A comparison of micrographs showed clustered networks for the uncharged composite but a disconnected array-like structure for anionic composites. Nematic emulsions made from dispersing PDMS droplets in lyotropic nematics show similar rheological behavior like the solid-sphere dispersion up to $\phi \leq 0.54$ but deviate near the glass transition volume fraction.

The flow behavior of these unique NLCs composites was also examined from steady-state measurements. The flow behavior of filled nematic is complex, owing to the coupling between the flow field and the director field. Both thermotropic and lyotropic composites showed remarkable shear-thinning behavior with the viscosity curve following power-law behavior. The breaking of the network structure into smaller clusters further explains this exceptional shear-thinning behavior on the application of shear. These clusters then align along the direction of flow, thus providing less resistance to flow, reducing the viscosity, and some evidence of shear-banding is evident. Relative viscosities ($\eta_r = \frac{\eta_\phi}{\eta_{LCs}}$) at high shear follow Krieger-Dougherty relation for the lyotropic composites. However, the deformable colloids (PDMS) in nematic emulsion diverts from Krieger-Dougherty relation beyond $\phi \geq \phi_g = 0.58$.

Through extensive rheological experiments and microscopy, we describe the physical properties of a new type of gel with exceptional stability and shear-thinning performance that could find wide application in the formulation industries.

Lay summary

This thesis, for the first time, studies the microstructure and flow behavior of a new class of soft solid. These soft solids are made by mixing colloids ($\sim$ 1 μm, invisible to the naked eye) in a liquid crystal material. Liquid crystal (LCs), as the name suggests, is a state of matter between crystalline solid and liquid. These unique materials can flow like a liquid but can align their molecules in a preferred direction. Nematic liquid crystal is the simplest phase of liquid crystal made up of rod-like or disk-like molecules, thus having only orientational order. In this thesis, we have explored the composite made from dispersing colloids in micellar based nematic LCs. On the addition of colloids, the alignment of nematic liquid crystal breaks to accommodate colloids in the medium. These soft solid form stable gel-like structure when the concentration of colloids increases beyond 20%. We suggest these soft solid may have a wide range of applications in the formulation industry; thus, in this thesis, we explore their structure and response to deformation using a technique called (*Rheology*) in terms of mechanical strength and viscosity to formulate a fundamental understanding.

In the first part of this thesis, we show that the soft solid composites made form mixing solid colloids in nematic LCs have exceptional stability in the absence of any external force. However, on the application on the force, the microstructure of these composites changes, giving rise to two different regions: (a) stable region - where the structure is not deformed and (b) yielding region - where the structure has deformed and changed according to the force applied. These two regions were further investigated by making a range of soft solid with different particle concentrations. The result suggested that the concentration of colloids ($>$ 20%) does not affect the stability of these composites but only enhances its mechanical strength. Microscopic images of these composites show a network like structure spanning over space. However, charged colloids disrupt the composite properties in the charged micellar nematic liquid crystal system. A comparison

of micrographs showed clustered networks for the uncharged composite but a disconnected array-like structure for anionic composites. After studying the solid colloid composites, we investigated the behavior of oil in nematic LCs emulsion underflow. It was observed that the oil droplets behave as solid colloids up to a concentration of 54% beyond which they start to touch each other and coalesce.

In the second part of this thesis, we study the viscosity profile of these composites. The viscosity of these composite in the absence of force is considerably higher compared to colloidal suspension in an isotropic solvent. However, on the application of force (shear), the composite viscosity decreases remarkably on the application of shear (force). The sharp decrease in viscosity was attributed to the breaking of the network structure into smaller clusters and their alignment in the direction of applied force. Thus, the viscosity after the breaking of the microstructure resembles that of dense colloidal suspensions.

Collectively, through extensive rheological experiments and microscopy, we suggest that filled nematic liquid crystal can offer an alternative route to creating a new type of formulation with exceptional stability and highly tunable viscosity without using any polymers.

Declaration

I declare that this thesis was composed by myself, that the work contained herein is my own except where explicitly stated otherwise in the text, and that this work has not been submitted for any other degree or professional qualification except as specified.

Parts of this work have been published in a Patent aplication 1908811.1 and three manuscript under preparation [90–92].

(*Navneeta Katyan, Dec 2019*)

Acknowledgements

I was honored to get a chance to pursue Ph.D. at the University of Edinburgh. Moreover, I will like to thank everybody who made this dream a reality.

First of all, I will like to thank my supervisor Dr. Tiffany Wood for introducing me to the colorful world of liquid crystal. She encouraged and inspired me to do independent research. Her constant support both in the scientific world and the personal world helped me to remain focussed and achieve some exciting results. She was always available and ready to help, and under her guidance, my scientific understandings have evolved remarkably. I will also like to extend my thanks to my internal examiners Paul Clegg and Job Thijssen, for their continuous support in monitoring my Ph.D. progress. My sincere thanks to Andrew Schofield for providing me the particles whenever needed; my Ph.D. would not have been complete without his timely support. I will also like to thank Davide Marenduzzo for giving insights on my work, which otherwise I would not have thought. I wish to extend my gratitude to all my colleagues, especially the people in the soft matter group who have provided me with valuable inputs at different points of this doctoral thesis.

I like to thank all my friends, especially Ankita, Arpita, Mohanish, Poonam, Shahana and Shilpi without whose support this thesis would not have seen the light of the day. Thank you for being my family away from home. I am indebted to my family, especially mama and chacha, for taking care of my younger brother while I was away fulfilling my dream of pursuing a Ph.D. I will like to extend my heartfelt gratitude to my mama for always being supportive of my decisions. A special mention to my sister, Shrishti, who have made me laugh on the toughest days of these four years.

My heartfelt thanks to Imtiyaz for his unconditional support and love in making our life happy, comfortable, and secured. I am thankful to my parents for giving wings to my dreams, and I am highly indebted to them for all the sacrifices they made. I want to say sorry to my brother, Navneet, for not being there when you needed me the most. I am very grateful for all you have done for me. Lastly, I dedicate all my achievement to my *ma* who made me what I am today, a strong independent woman. Thank you!!

Two roads diverged in a wood,
and I—
I took the one less traveled by,
And that has made all the difference.

- Robert Frost , 1916

Contents

List of Figures

List of Tables

Chapter 1

Introduction

There are no limits to what science can explore.

- Ernest Solvay

1.1 Motivation

Complex fluids form an integral part of our daily life. We interact with them in the form of our personal care products, the food we eat, in the screens of our smartphones, television, computer, and so forth. Some of the most common examples of complex fluids include polymeric solutions and melts [56], colloidal suspension [176], liquid crystals, and their composites [200] forming superstructures such as gels, foams, and emulsions. Complex fluids can be distinguished from Newtonian liquids, and crystalline solid from their structural ordering length scales, which are greater than the atomic length scales yet smaller than the world visible to the human eye; thus, the length scales are in the range of 1nm - 10 microns. They are used extensively in food processing, pharmaceutical formulations, paints and coatings, personal care, and cosmetic products. In the formulation world, rheological properties like flow behavior and viscoelastic response determine the success and failure of the quality of the product. Thus, the rheology of complex fluids becomes a vital tool to probe the microstructure of the formulations under external shear. In this thesis, we couple rheology measurements with microscopy to study the structural properties of a class of soft solid formed by dispersing colloids in liquid crystalline media.

Liquid crystal (LCs) [149] is a mesophase between crystalline solid and Newtonian liquid. In this thesis, we explore the interaction of colloids in both lyotropic and thermotropic nematic LCs. We concern ourselves with the class of lyotropic liquid crystals formed from mixtures of amphiphilic molecules in a solvent that form liquid crystalline phases at a specific temperature and concentration ranges [33],[6],[36],[57]. A lyotropic liquid crystal composed of a ternary system of surfactant, co-surfactant, and water along with thermotropic 5CB liquid crystal [44] is studied. Thermotropic liquid crystals are widely used in display technology of low energy costs and many sensor devices. The study of lyotropic mesophase is essential because of a wide range of applications in the formulation industry, including detergents and cosmetics [54], pharmaceuticals, and drug delivery [49]. This Ph.D. project was associated with a Royal Society Industry Fellowship held by Dr. Tiffany Wood in collaboration with The Mentholatum Company Limited. One of their most popular products, Deep heat, is a topical cream made from dispersing colloids in lyotropic lamellar liquid crystal to deliver an active to relieve body pain. Thus, we hoped to develop new knowledge on colloidal dispersions in lyotropic liquid crystalline phases to explore whether there may be alternative routes to improve the efficacy of topical creams. Studying the structure and dynamic properties of lyotropic phases are very important from both fundamental and practical points of view, especially considering their potential for applications in the formulation industry.

1.2 Thesis outline

This thesis is divided into nine chapters. The first two chapters describe the background science used in this thesis. Chapter 2 sets the context for the materials that will be explored by introducing different types of complex fluids materials, liquid crystals, and composites. Chapter 3 provides a brief description of the experimental rheometry followed by different rheology models used in different complex fluids discussed in chapter 2.

Chapter 4 gives a full description of the material and experimental methods used in this thesis.

The results of the thesis are covered in chapters 5 - 8. Chapter 5 explores the microstructure and viscoelastic property of uncharged colloids dispersed in thermotropic nematic liquid crystals (LCs). We have, for the first time, studied

the effect of both hard-sphere colloids and oil droplets, which are deformable in lyotropic nematic liquid crystals. Chapter 6 focuses on the effect of surface charge on the colloidal particle has on the oscillatory rheology of colloids and liquid crystal composite. The microstructure of charged composites is further studied using microscopy. In chapter 7, we discuss steady-state shear rheology of both charged and uncharged colloidal composites in nematic liquid crystals. The viscosity curve of the composites is studied, and the effect of filler concentration is described. Finally, in chapter 8, we describe the microstructure and rheology of colloids dispersed in the lyotropic lamellar phase to set the context with the nematic composites.

Lastly, in chapter 9, we summarize the main findings of this research. Then we discuss the potential application of the colloids, forming a gel in lyotropic nematic liquid crystal. Lastly, we conclude by summarizing the research and its future perspective.

Chapter 2

Complex fluids in the context of liquid crystals

Complex fluids are those with internal microstructures whose evolution affects the macroscopic dynamics of the material, especially their rheology. Some of the examples include polymer solutions and melts, liquid crystals, gels, suspensions, emulsions and micellar solutions [12].

2.1 Colloids

A colloidal dispersion is a heterogeneous system in which particles or liquid droplets of size 10 μm or less are dispersed in a liquid medium. If the particles are small enough to minimize the effect of gravity they move in a random fashion known as Brownian motion with thermal energy, k_BT. In conventional hard-sphere colloidal dispersions, the particles often interact via attractive force such as van der Waals forces and repulsive force such as electrostatic forces in addition to the hydrodynamic forces. These forces are isotropic, and their range does not usually exceed a few tens of nanometers.

Suspensions can be classified as Brownian and non-Brownian. Brownian suspensions are dilute suspensions composed of small particles (r $\ll \mu$m) which can be disturbed by thermal motion. The minimum energy required to fluctuate these suspensions from their equilibrium position is equal to thermal energy, k_BT, where k_B is Boltzman constant and T is the temperature. Non-Brownian

suspension have larger particles in them. Colloidal glasses have motion within their *cages* due to Brownian motion [122]. The transition from Brownian to non-Brownian motion is defined by P*é*clet number, (Pe).

$$Pe = \frac{r^2\dot{\gamma}}{D_s} \tag{2.1}$$

where r is particle radius, $\dot{\gamma}$ is the shear-rate and $D_s = \frac{kT}{6\pi\eta r}$ the short-time diffusion coefficient which is dependent on the particle volume fraction, ϕ. Peclet number defines the effect of Brownian motion on the viscosity of the colloids. Viscosity becomes independent of Peclet number at Pe $> 10^3$, at this regime the hydrodynamic interaction suppresses Brownian motion [76]. The effect of inertia on the viscosity of the suspension is governed by the particle Reynolds number [182]. Reynolds number has the mathematical form given by Equation: [**?**], where ρ is the density of the suspension.

$$Re = \frac{\rho r^2\dot{\gamma}}{\eta} \tag{2.2}$$

2.2 Polymers

Polymers are giant molecules which are essential for our existence. They are the main constituents of the formulation world, for example as starch and protein in foods, as nylon and polyester in the clothes we wear and as thickeners and emulsifiers in our personal care products. They can be classified as (a) homopolymer where all monomer links are identical, (b) co-polymers which are made up of different monomers and (c) block co-polymer - made up of two long sequences of different monomer. The structure of polymer can be linear, branched or network like with cross-links. Their larger sizes lead to much stronger intermolecular forces leading in turn to much higher melting points, and the characteristic properties of hardness and flexibility. On application of external force, the structure of polymer distorts like an elastic spring. The elasticity of these polymer decreases with increasing temperature. Polymers show strong viscoelastic properties such as shear-thinning and time-dependent rheology because the polymers are long and easily distorted even at low stress values.

In this chapter, we review the underlying physics of liquid crystalline materials

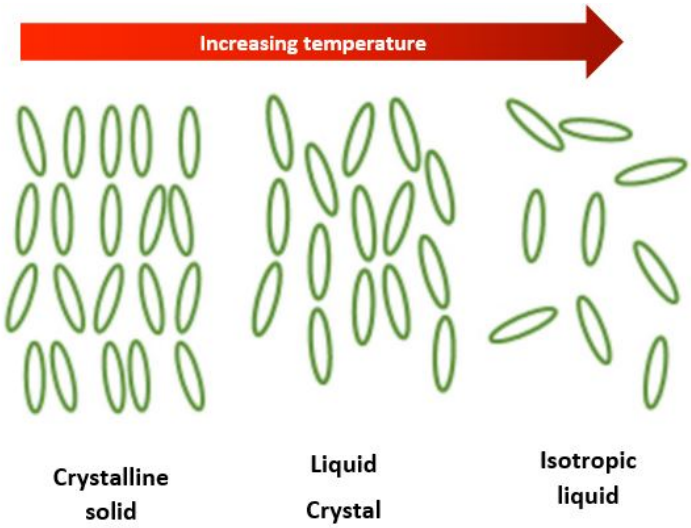

Figure 2.1 *Schematic of phase transition from crystalline solid to liquid crystal to isotropic liquid on increasing temperature.*

and focus on the nematic mesophase before moving onto the physics of colloidal dispersion in nematic LCs mixture.

2.3 Liquid crystalline materials

Liquid crystals are a class of complex fluid intermediate between a crystalline solid and a liquid [149, 173]. Liquid crystallinity is expected to occur in the presence of elongated molecules like rod-shaped and disc-shaped because of their high aspect ratio. In a liquid crystalline phase, the basic building blocks display orientational order (e.g., ordering of molecules in nematics); however, some mesophases can even show positional order as in smectic mesophase. A liquid crystalline phase transition to the isotropic liquid phase occurs on increasing the temperature. Liquid crystals (LCs) can be further classified into thermotropic and lyotropic phases. In thermotropic LCs, the phase transition is governed by the change in temperature only. Figure 2.1 shows the transition of crystals to the liquid crystal to isotropic liquid with increasing temperature. Thermotropic LCs are widely used in display technology and sensory devices. Lyotropic liquid crystals, on the other hand, are formed in a particular concentration range. Their mesomorphic properties change with the change in the relative concentration of constituent molecules in addition to the temperature. The basic units of lyotropic LCs studied here are the self-assembles amphiphilic molecules, which can form shapes of rod

and discs [5, 7, 57, 150], however lyotropic LCs phases are also found in nature in the form of nano-crystalline cellulose and lipids [3]. The ordering of molecules in LCs leads to different classes of mesophases. In both thermotropic and lyotropic LCs, the nematogens (building blocks) are often rod-shaped. In thermotropic LCs, nematogens are anisotropic molecules, whereas, in the lyotropic LCs, they can be uni-axial micelles or rod-shaped nanoparticles like clays and cellulose. Nematogens usually have an aspect ratio greater than 3. Our focus in this thesis will be on the rheology of both thermotropic and lyotropic LCs.

2.3.1 Lamellar liquid crystal

Lamellar liquid crystalline phases have a bilayer structure formed by amphiphilic molecules separated by water layers and show homeotropic or focal-conic (threadlike, mosaic or oily streaks patterns), [166], [85] texture under cross-polarisers, see Figure: 4.8. The stability of the long range periodicity in lamellar phases is determined by a balance between fundamental interactions such as the van der Waals attraction, the electrostatic repulsion for charged membranes, and the short-range repulsive hydration interactions which, for instance, prevent phospholipid bilayers in water from coming into close contact with each other. As one-dimensional crystals of parallel layers, the lamellae possess translational symmetry and thus exhibit dislocations (screw and edge dislocations) [137]. They play a crucial role in determining many properties of these materials and may be involved in shear induced structural transformations. Lamellar phases are known to exist in at least two configurations. In addition to a planar or continuous lamellar phase, where the bilayers are ordered in sheets, lamellar phases exist with the bilayers ordered in closed concentric shells. The structural units in the latter phase are often referred to as "onions", multilamellar vesicles, or lamellar droplets. These phases have a wide range of applications in the formulation industry, thus have been studied extensively.

2.3.2 Nematic liquid crystal

In the nematic phase of LCs, nematogens align themselves in a preferred direction. This preferred direction is called the Frank director, $(\vec{n})$. Thus the aligned molecules are free to move in three translation directions and rotate around the director. However, the mean distance between molecules is smaller than their

diameter, so rotation is not completely free. These LCs are turbid in appearance because their scattering index is 10^6 times higher than the isotropic fluid. In the nematic phase $(\vec{n})$ and $(-\vec{n})$ are equivalent and the order parameter (OP) is given by Equation: 2.3 which defines the equivalence of both $(\vec{n})$ and $(-\vec{n})$ [149].

$$OP = \frac{3\cos^2\theta - 1}{2} \tag{2.3}$$

It characterizes the distribution of oriented molecules. It is defined as the average over all of the second Legendre polynomial [183], where θ is the angle between a molecule and the director, $(\vec{n})$. OP is equal to unity when all the molecules are aligned parallel to $(\vec{n})$ and is zero when the distribution of orientations is random, as for the isotropic phase.

Free energy

When a force exerts onto a spring, the spring deforms by either getting extended or suppressed. A spring has a characteristic elasticity (k) that resists deformation, $\vec{F} = k\vec{x}$. Similarly, the liquid crystals are effectively elastic media that resist external perturbations. When the external force exerted exceed a threshold value, the director deforms elastically, leading to a change in the relative orientation of LCs molecules. The molecules will be forced to splay, twist, saddle splay, and bend as shown schematically in the Figure: 2.2. When the system is in equilibrium, it is in the minimum energy state. The director configuration can thus be explained in terms of free energy. The Equation : 2.4, gives the total free energy of a nematic LCs consisting of both surface and bulk terms. This expression was first developed by Oseen, Zocher, and Frank [58, 138, 206]. This is then minimized to get director configuration.

$$F_n = F_{el} + F_{24} + F_S = \int (f_{el} + f_{24} + f_H)\, d_r^3 + \int f_S\, dS \tag{2.4}$$

The first two terms are the elastic energy term arising from any deviation from its spatially uniform director. And they are called Oseen-Zocher-Frank free energy density [58, 138, 206], which consists of two parts given by Equation: 2.5 and 2.6.

$$f_{el} = \frac{1}{2}[K_1\vec{n}^2 + K_2(\vec{n}\cdot\nabla\times\vec{n})^2 + K_3(\vec{n}\times\nabla\times\vec{n})^2] \tag{2.5}$$

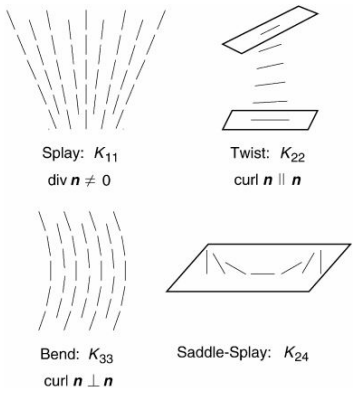

Figure 2.2 *Schematics of characteristic deformation in a nematic LC: splay, twist, bend and saddle splay.Taken from [111].*

where $K_1; K_2; K_3; K_{24};$ denote, respectively, the splay, twist, bend, and saddle-splay elastic constants.

$$F_{24} = -\frac{K_{24}}{2}[\nabla \cdot (\vec{n} \cdot \nabla \cdot \vec{n} + \vec{n} \times \nabla \times \vec{n})] \tag{2.6}$$

A relation between K_{24} follows from the Maier Saupe molecular approach [117].

$$K_{24} = \frac{(K_{11} + K_{22})}{2} \tag{2.7}$$

$K_1; K_2; K_3; K_{24}$ are of the same order of magnitude, an assumption only valid for thermotropic LCs often used to simplify the equations. The surface free energy of Rapini-Papoular is used to take into account the interaction between the director and the surface boundary:

$$f_S = \frac{W}{2}[1 - (\vec{n} \cdot \hat{v})^2] \tag{2.8}$$

The unit vector $\hat{v}$, denotes some preferred orientation of the director at the surface, and **W** is the coupling constant or anchoring energy and has unit of kJ per mol. By comparing the Frank free energy and the surface energy one arrives at the extrapolation length shown in Equation: 2.9,

$$\xi_S = \frac{K_3}{\mathbf{W}} \tag{2.9}$$

ξ_S signifies the strength of anchoring and has a unit of length, which becomes

relevant when discussing the behavior of colloids in LCs. For example, take a particle of radius a in a nematic LC, which has a uniform director field at infinity. The Frank free energy of this system is proportional to $K_3 a$, whereas the surface energy is to $\mathbf{W}a^2$. At strong anchoring, i.e., for $\mathbf{W}a^2 \gg K_3 a$, or $\xi_S \ll a$, the surface energy dominates and turns the director away from its preferred direction $\vec{n}$. If $\xi_S \geq a$, then weak anchoring occurs, where the effect of the surface term is not dominant, and the bulk elasticity, K, dominates.

Nematodynamics

The flow behavior of nematics are complex compared with an isotropic fluid for two main reasons; (a) the translation motion during flow is coupled with the inner orientation of nematic, thus changing the alignment and (b) a change in the director alignment in the presence of external force induces flow. Ericksen-Leslie [53, 104, 105] and Parodi were the first to propose a dynamic equation of the director field of LCs using a macroscopic approach based on classical mechanics. A microscopic approach has been employed by Harvard and group [32, 87], but both the approaches give a similar equation.

Ericksen-Leslie assumed LCs as a continuum, possessing both translational and orientational degrees of freedom. The full set of equations was derived from the balance of linear and angular momentum and is mathematically written as a function of velocity field *v(r)*, which defines the flow and $\vec{n}$, which defines the orientation of nematic molecules. In cartesian co-ordinates director, $\vec{n}$ can be written in terms of θ and ϕ as:

$$\vec{n(r)} = (n_x sin\theta cos\phi, n_y cos\theta cos\phi, n_z sin\phi) \tag{2.10}$$

$$\vec{v(r)} = (u(x,y,z), v(x,y,z), w(x,y,z)) \tag{2.11}$$

$$\vec{P} = P(x,y,z) \tag{2.12}$$

Here n_x, n_y and n_z are the unit vectors, P is the pressure of nematic fluid and $\vec{v(r)}$ is the velocity vector. The conservation equation is then written as:

$$\nabla.v(\vec{r}) = 0 \tag{2.13}$$

$$\rho\frac{dv(\vec{r})}{dt} = \nabla.\Sigma \tag{2.14}$$

$$\Sigma = -P + \Sigma^0 + \Sigma' \tag{2.15}$$

where $\nabla.\Sigma$ is the divergence of stress tensor $(\Sigma) = \nabla_j\Sigma_{ij}$. From Equation: 2.15 it is seen that stress tensor consists of a pressure term and two other terms shown in Equation: 2.16 and Equation: 2.17.

$$\Sigma^0_{ij} = -\frac{\partial f_b}{\partial(\nabla_j)\vec{n}_k} \tag{2.16}$$

$$\Sigma'_{ij} = \alpha_1 n_i n_j n_k n_l \vec{A_{kl}} + \alpha_2 n_j \vec{N_i} + \alpha_3 n_i \vec{N_j} + \alpha_4 A_{ij} + \alpha_5 n_j n_k \vec{A_{ik}} + \alpha_6 n_j n_k \vec{A_{jk}} \tag{2.17}$$

where f_b is the Frank free energy term excluding surface anchoring term (f_S) and Σ^0 is the stress tensor due to elastic distortion. Σ' gives information about the viscous part of stress tensor, A_{ij} is the symmetric gradient of the velocity field given by: $A_{ij} = \frac{1}{2}(\nabla_i v_j + \nabla_j v_i)$, α_1, α_2 and α_3 are called Leslie coefficient of viscosities. Finally, the total torque on the director should be zero by balancing elastic (τ^0) and viscous (τ') part.

$$\vec{n}X(\tau^0 - \tau') = 0 \tag{2.18}$$

where

$$\tau^0_i = \nabla_j(\frac{\partial f_b}{\partial\nabla n_i} - \frac{\partial f_b}{\partial n_i}) \tag{2.19}$$

$$\tau'_i = \gamma_1\vec{N_i} + \gamma_2\vec{A_{ij}}n_j \tag{2.20}$$

N denotes the rate of change of the field relative to the fluid motion. $\vec{N} = \frac{d\vec{n}}{dt} - \varpi \times \vec{n}$, where $\varpi = \frac{1}{2}(\nabla \times \vec{v})$. And $\gamma_1 = \alpha_3 - \alpha_2$ and $\gamma_2 = \alpha_2 + \alpha_3$. The first term of the viscous torque (τ'_i) describes the viscous process due to the rotation of neighboring molecules with different anguar velocity. Thus, γ_1 is called the rotational viscosity. The second term describes the torque on the director due to

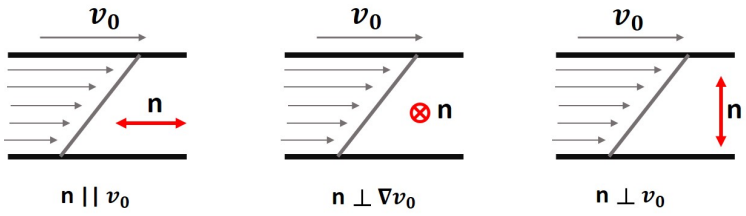

Figure 2.3 *Schematic representation of three different director directions with respect to plate velocity direction.*

shear flow.

In the parallel-plate geometry under shear flow, the sample flow can be described by three different cases (see Figure: 2.3). Here the upper plate moving with a constant velocity ($\vec{v_0}$).

The viscosity of the nematic LCs in all the cases is given by;

$$\eta_1 = \frac{\alpha_3 + \alpha_4 + \alpha_6}{2} \tag{2.21}$$

$$\eta_2 = \frac{\alpha_4}{2} \tag{2.22}$$

$$\eta_3 = \frac{\alpha_4 + \alpha_5 - \alpha_2}{2} \tag{2.23}$$

These are called Miesowicz viscosities. In the literature, 5CB has been characterized thoroughly, the Miesowicz viscosities are $\eta_1 = 0.088$ Pa.s, $\eta_2 = 0.094$ Pa.s and $\eta_3 = 0.015$ Pa.s and the rotational viscosity $\gamma_r = 0.081$ Pa.s [39, 83, 132, 160].

2.3.3 Topological defects in nematic LCs

Topological defects are the defects that arise from breaking the continuous symmetry of the system and cannot be fixed by any local rearrangement of molecules. Topological defects are important in determining the properties of physical systems. In superfluid helium, they are called vortices; in periodic crystals, one refers to dislocations, and in liquid crystals, they are disclinations [149]. The defect dynamics of these phases contribute to the rheological properties. There are two types of defects found in nematic LCs. These are either

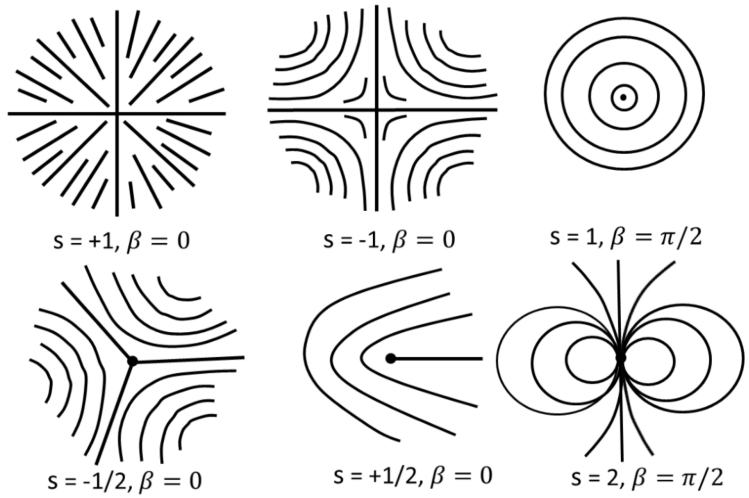

Figure 2.4 *Schematic representation of a few defects with different winding numbers. Continuous lines represent the director field around the singularity.*

line defects, known as disclinations (showing the discontinuity in the inclination of molecules) or point defects (hedgehogs and boojums), where the director cannot be defined. There are two important aspects of topological defects in liquid crystals. Firstly, the topological defects are regions of reduced orientational order of the liquid crystal molecules in addition to the strong elastic deformation of LCs molecules. Secondly, in addition to free energy, topological defects are, mathematically speaking, points or loops where the ordering field is singular, i.e., the field is not defined in those regions. These defects cannot be eliminated by continuous deformation of the order parameter field; hence, they are topologically stable [32]. They are characterized by strength or winding number $'s'$, which is denoted by an integer or half-integer number. The strength $'s'$ determines the number of times the director rotates around the singularity when one encircles the defect core [173]. Two oppositely-charged defects can annihilate one other. The orientation of the nematic director field (Ψ) surrounding the defect can be expressed in terms of defect strength ($'s'$) [149].

$$\Psi = s\alpha + \beta \tag{2.24}$$

where $\alpha = \tanh(y/x)$ and β is a constant. Here, the defect strength $'s'$ depends on the symmetry of the medium. In the nematic phase, $'s'$ is the multiple of $\pm\frac{1}{2}$, as the director has $(\vec{n}) = (-\vec{n})$ symmetry. Figure: 2.4 shows the schematic representation of the director structure of a few defects. Readers are directed to

appendix 1 for a comprehensive review on line and point defects in nematic LCs.

2.3.4 Single particle in the nematic LCs

In this section we explore the director configuration around a single particle dispersed in the nematic solvent aligned uniformly at infinity. This one particle problem will be a guide to the understanding of more complex situations like many-particle interactions in a nematic LCs. For spherical particles in a nematic environment, elastic interactions are highly anisotropic and can lead to a host of self-assembled structures ranging from linear and branched chains. When a single particle is dispersed in LCs molecules, the molecules align along the curved surface of the particle for planar alignment and perpendicular to the surface of the particle in homeotropic alignment. The LCs molecules are frustrated, as they prefer to align along with their director the way they do in the absence of particle. This inability to fill the space with a uniformly aligned nematic LCs results in a strong elastic distortion. The director field around a sphere exhibits quadrupolar symmetry for tangential anchoring and dipolar or quadrupolar symmetry for homeotropic anchoring.

The director field configuration is found by minimizing Frank Free energy. A plausible director distribution function can be formulated with the director deviation angle of $\beta(a)_r$ [97]:

$$\beta_a(r) = \theta - \frac{1}{2}\arctan\frac{\sin 2\theta}{(a/r)^2 + \cos 2\theta} \tag{2.25}$$

where a is the radius of the disclination ring, and this reflects quadrupole symmetry as $\vec{n}$ has its deformation in the form $\delta n(\vec{r}) = \frac{a}{r}^2$.

The Frank free energy is written in one constant approximation without the surface term (see Equation: 2.28):

$$F = \int \frac{1}{2}(\nabla \cdot \vec{n}^2 + (\nabla \times \vec{n})^2)\, d^3r \tag{2.26}$$

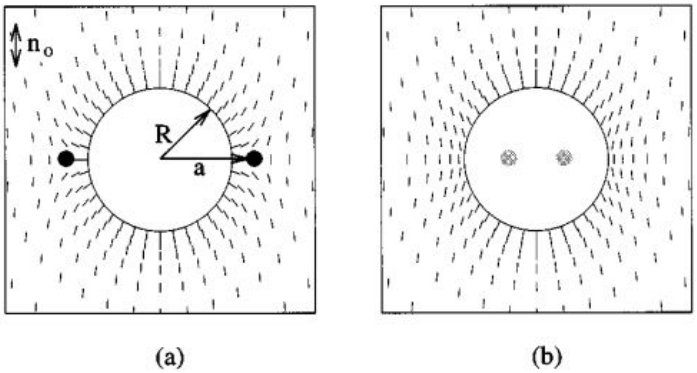

Figure 2.5 *(a) Particle of radius R with rigid radial boundary conditions and a disclination ring of radius a in the plane perpendicular to* $\boldsymbol{n}$*, (b) The particle with weak radial anchoring on the surface has a regular director distribution, which may be treated as an "image" disclination ring with R. [97]*

The anchoring energy is defined using the Rapini approximation [58].

$$F_S = -\int \frac{1}{2} W(\vec{n} \cdot \hat{v})^2 dS \tag{2.27}$$

In the next section, the director configuration in weak and strong anchoring conditions between colloids and the nematic host is discussed.

1. Weak Anchoring

   The differential equation found by minimizing free energy is generally not solvable analytically but if an assumption is made that in the case of weak anchoring the deviation of the director field is small then the problem can be linearized. In Figure 2.5, the director can be defined (using spherical co-ordinates) by two principal angles $n_z = cos\beta(r); n_x = sin\beta(r)cos\phi; n_y = sin\beta(r)sin\phi$, here ϕ is azimuthal angle and θ is the polar angle. After applying the boundary condition on the particle surface at $r = R$. The differential equation becomes:

   $$\nabla^2 \beta - \frac{\sin 2\beta}{2r^2 \sin^2 \theta} = 0 \tag{2.28}$$

   The particle is dispersed in an uniform nematic environment, hence azimuthal symmetry is appl ied in the above equation:

   $$\frac{\delta \beta}{\delta r} = -\frac{W}{2K} \sin(\theta - \beta) \tag{2.29}$$

Since the director deviates only by a small amount $\beta(r) \ll 1$, so the Equation: 2.29 becomes,

$$\nabla^2\beta - \frac{\beta}{(r^2 \sin 2\theta)} = 0 \tag{2.30}$$

$$\frac{\delta\beta}{\delta r} + \frac{\beta}{r} = \frac{-W}{2K} \sin 2\theta \tag{2.31}$$

The general solution of the above two equations is given by Legendre Polynomial,

$$\beta = \Sigma_k \frac{C_k}{r_{k+1}} P_k^1 \cos\theta \tag{2.32}$$

where P_k^1 is the associated Legendre Polynomial [163]. The boundary conditions on a particle selects a particular mode *k=2* with $C_{k\neq 2} = 0$. Thus the director rotation angle takes the form:

$$\beta = \frac{WR}{4K} \left(\frac{R}{r}\right)^3 (sin2\theta) \tag{2.33}$$

if $\beta \ll 1$, then $WR/K \ll 4$. Weak anchoring corresponds to values, $W \leq 10^{-7} J/m^2$, taking the typical value of elastic constant $K \approx 10^{-12}$ N, R $\ll$ 0.5 mm. Even for anchoring as strong as $W \approx 10^{-5} J/m^2$, R < 5-6μm will satisfy linear approximation of the director field deviation satisfied by β. The decay rate of deformation of director field $\beta = 1/r^3$. This is because an assumption has been made that the particle is at the origin.

2. Strong Anchoring

   In strong anchoring one cannot assume that $\beta \ll 1$, in the vicinity of the particle and there is no straightforward way to obtain the solution. One possibility is to interpolate the far-field behavior by comparison with Equation: 2.34. A new trial function is chosen which gives an asymptotic behavior, $\beta \approx \frac{\sin 2\theta}{r^3}$. To check the degree of accuracy of the function, the numerical solution in one constant approximation was considered [59, 82] for the director field rigidly anchored at $\beta = \theta$ on the spherical surface and $\beta = 0$ at infinity. *f(r)* is a function of r independent of θ and in far field limit, $f(r) = (\frac{r}{a})^3$ which adequately describes the director direction at $r \ll a$. In the other two values of r: $r = R, f(r) = 0$ (i.e. for rigid anchoring $\beta = \theta$ and at $r = a, f(r) = 1$ (i.e., disclinaton at $\theta = \pi/2$).

It has been seen that by fitting the universal function *f(r)* to the result provided by the numerical solution [114, 196] an interpolated expression is obtained, which satisfies all the above constraints and allows us to work with the "analytical" form of β_r, given by equation of *f(r)*: where A, B, and C are coefficients.

$$f(r) \approx (\frac{r}{a})^3 + A + B\frac{r}{a} + C\exp^{-r/a} \tag{2.34}$$

where A and B is given by Equation: 2.36 and $C = -\frac{4a-3R}{a-R}$. It is evident from the equation, that when $a \to R$ the function *f(r)* and β becomes unstable.

$$A = \frac{R^3}{a^2(a-R)^2}[R - a + \frac{a^2}{R^2}(4a-3R)(\frac{a}{R}\exp^{-R/a} - \exp^{-1})] \tag{2.35}$$

$$B = \frac{R^3}{a^2(a-R)^2}[a - R + (4a-3R)(\exp^{-}1 - \exp^{-R/a})] \tag{2.36}$$

After examining two limiting anchoring conditions: a) the weak anchoring situation when the director deviations are small in the whole system, and the exact analytical solution is possible and in the rigid anchoring case characterized by the disclination ring. In both situations, the far-field behavior of director is identical and is described by the cubic power decay of deformations. The interesting question is to find out at what values of anchoring energy, W, does the crossover between the two above regimes take place. One of the simplest ways is by balancing surface and bulk energies when the disclination is lying on the particle surface.

$$\beta = \frac{WR}{4K}(\frac{R}{r})^3 \sin 2\theta \tag{2.37}$$

$$\beta = (\frac{a}{r})^3 \sin 2\theta \tag{2.38}$$

This provides the estimate $W^* \approx \frac{4Ka^3}{R^4}$. Considering the equilibrium ring size as a =1.25R, then $(W^*R/4K) = 2$. Thus the deformation energy in both the cases is given by Equation: 2.39 and 2.40 . For weak anchoring the free energy increases with anchoring energy as W^2 and cubically with the particle radius (r)

and inversely proportional to K.

$$F_c \approx 0.2(\frac{W^2R^3}{K}) \tag{2.39}$$

For strong anchoring, the free energy linearly with elasticity of LCs (K) and particle radius (r),

$$F_c \approx 6.7\frac{Ka^6}{R^5} \rightarrow 13KR \tag{2.40}$$

2.4 Interaction between colloids in nematic liquid crystals

LC colloids are formed by dispersions of colloidal particles in the LCs host. Due to surface alignment, the director field is forced to align along a closed surface of the sphere, which results in the appearance of topological defects of the nematic orientational field. These deformations result in a strong elastic interaction between neighboring colloidal particles in the nematics. This interaction force triggers the spontaneous assembly of nematic colloids within seconds, where the process of pair interaction is strongly characterized by topological defects. Topological defects are, therefore, significant for the interaction of nematic colloids. The first study of colloidal dispersion in a LCs solvent was carried out by Brochard and de Gennes in 1970, where they studied a suspension of magnetic grains in a nematic phase and the resultant director distortion [25]. A bistable liquid crystal display was introduced based on a dispersion of silica spheres in a nematic host [102, 161]. Chains and clusters were observed in the dispersion of latex particles in a lyotropic liquid crystal [143, 157, 191]. Kuksenok and Terentjev [97] first studied the orientation of the director field around a spherical particle by both analytical and numerical models. They concentrated on Saturn-ring and surface-ring configuration. The experiments carried out by Philippe Poulin and his team on an inverted emulsion with water droplets dispersed in a nematic environment demonstrated a dipolar structure with the presence of a water droplet [155]. Interestingly, no Brownian motion was observed in the emulsion. This was attributed to the anchoring strength, **W**, between colloids and the nematic host, being 1000 times greater than the thermal energy (k_BT)

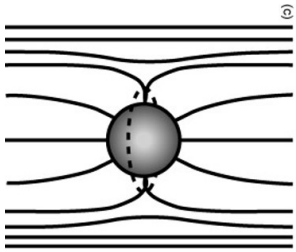

Figure 2.6 *A schematic representation of director distortion around colloid microspheres forming Saturn-ring defects.*

[1, 80]. Under a polarizing optical microscope, they saw that the water droplets spontaneously formed chains, which were directed along with the nematic director (the direction of the average orientation of liquid-crystal molecules). Although fluid, the water droplets did not coalesce into larger droplets but remained separated from each other by a topological defect that was spontaneously created in the vicinity of each droplet. This experiment was clear evidence of the existence of a new type of force that acts between colloidal inclusions in the nematic liquid crystals.

In the presence of small spheres, the nematic LCs director distorts homeotropically from the spherical surface to a uniform far-field orientation and thus forms a ring defect structure called Saturn-ring because of their resemblance to the rings of planet Saturn. Gu and Abbott [66] studied these Saturn-ring defects induced by weak anchoring between microspheres and the nematic medium. These ring defects form closed disclination loops around the particles. Figure 2.6 schematically represents the Saturn-ring defect formed around a colloidal particle. When micrometer-diameter colloidal particles are dispersed in the nematic, the strength of this force is typically tens of pN at a typical surface-to-surface colloidal separation of a micrometer [89]. The force has its origin in the ordering and elasticity of the nematic medium and, most importantly, in the alignment of the liquid crystal molecules along the closed surface of the colloidal inclusion. The range of the elastic forces is of the order of several colloidal diameters. The colloidal forces in the nematic solvent are much stronger than the forces present in colloids in isotropic solvent exceeding $\sim$ 1000 k_BT per micron-sized particle [89, 135]. These interactions are of long-range and in many respects similar to the electrostatic interactions between dipoles, quadrupole i.e. long-range attraction, and short-range repulsive. Aqueous suspension of rod-like and plate-like particles form liquid crystalline phases with an increase in concentration. It is known that aqueous suspension of sepiolite clay particles (rod-like) exhibit nematic liquid

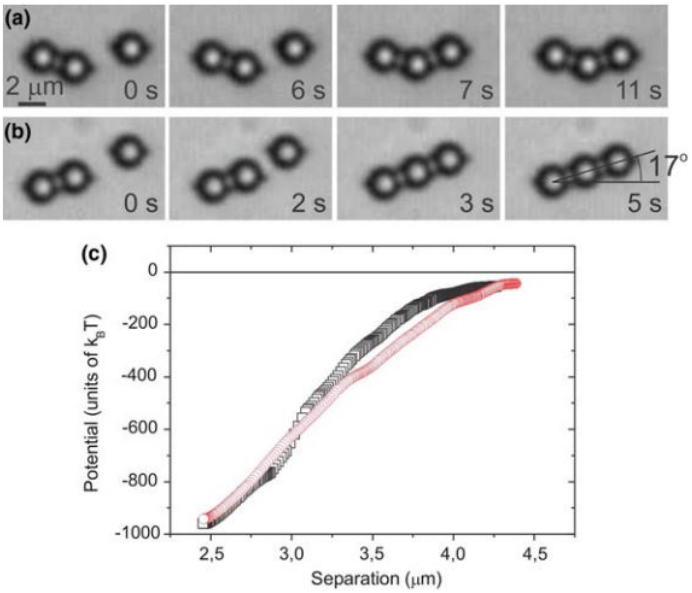

Figure 2.7 *Quadrupolar colloidal chains can grow in a form of kinked (a) or straight chains (b). (c) The quadrupole–quadrupole interaction as a function of separation between the particles. The black squares correspond to (a), the red circles correspond to (b).*

crystalline phase [201] and aqueous montmorillonite (plate-like) suspension gel at 1% volume fraction. Duijneveldt *et al.* [202] studied the formation of the nematic phase in a suspension of sepiolite and montmorillonite clay mineral particles. They showed that at low concentration, $\phi \sim 0.09$, the mixture shows three phases with nematic phase as one of them, but at high concentration, a gel was formed. This experiment suggested that it is possible to alter the behavior of rod and plate suspension to exhibit the nematic phase.

Isolated Saturn-ring defects

The force between the boojum quadrupolar colloids [193] in nematic LCs was first measured experimentally by Smalyukh *et al.* [180]. Sabot *et al.* [89] experimentally studied the interaction of quadrupole nematic colloids with homeotropic surface anchoring. They used 2-4 μm silica spheres covered with a monolayer of silane. Experimentally it was observed that quadrupole-quadrupole interaction was much weaker than dipole-dipole interaction [79, 107, 111, 135, 155, 158] and shows $\frac{1}{x^6}$ dependence where x is the separation between the quadrupolar pairs. This relation is similar to the interaction force dependence between two electrical quadrupoles. The pair binding energy, which is the work force

separating the particle from the bound state to infinity, was of the order of 100 k_BT [89], which is one order of magnitude less than the dipole-dipole interaction. As a consequence, inbound quadrupole colloids in NLCs are fragile and are easily perturbed by the flow.

Different topological configuration of quadrupolar colloids is represented in the Figure: 2.7. These colloids form kinked chains, as well as straight chains, Figure: 2.7b at 17° angle from the direction of rubbing. In both the formations, the pair binding energy between isolated Saturn-ring is $\sim 1000 k_B$T, as plotted in Figure: 2.7c. Readers can refer to [1, 78, 80, 106, 131, 179] for details on the experimental technique used to determine interaction potential among quadrupolar and dipolar colloids.

2.4.1 Multiple nematic colloids

In this section, we study the inetraction forces when more than one nematic colloids confined between thin layer ($< 100\mu$m) glass slides. These colloids assemble into irregular shaped connected clusters see Figure: 6.3. This observation demonstrates the existence of an attractive long-range force and a short-range repulsive force contrary to the interaction among hard-spheres in an isotropic solvent. At first we will discuss the hard-sphere inetraction followed by colloids in anisotropic solvent more specifically in nematic liquid crystalline media.

Hard-sphere interaction

Understanding the interplay of forces between colloids and colloids and solvent play an important role in determining the rheology and microstructure of the composites. Colloidal forces arise from inter-particle interactions either by direct contact between the particles or by indirect contact between the particles and the solvent.

Interparticle forces present in isotropic suspended system are well documented in [12, 16, 75, 164, 194**?**]. These are: London-van der Waals interaction, electrostatic repulsion, steric stabilisation and hydrodynamic forces between colloid and solvent. The total interparticle potential between two microspheres

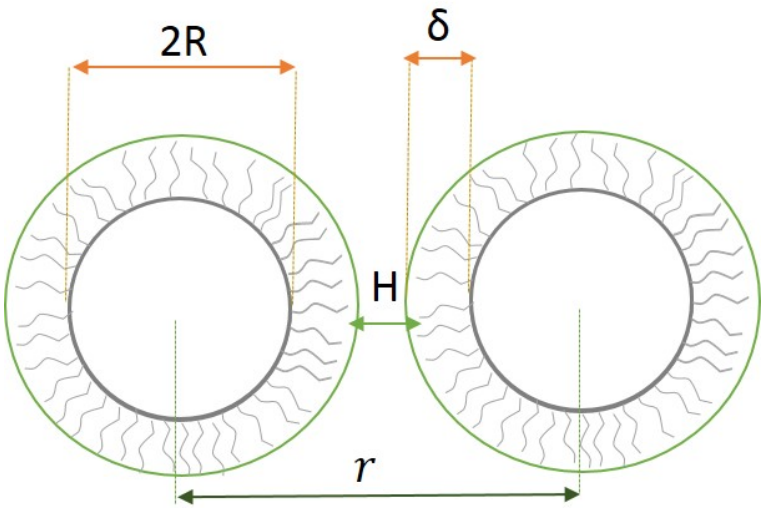

Figure 2.8 *Schematic represenation of two hard-spheres, where D is the diameter of the sphere, h is the inter particle separation between steric stabilised colloids, D^i is interparticle space and δ is the steric stabilisation layer .*

(see Figure: 2.8) $\vec{U_T}$ can be written as:

$$\vec{U_T} = \vec{U_{Vd}} + \vec{U_{el}} + \vec{U_s} + \vec{U_{dep}} \tag{2.41}$$

where $\vec{U_{Vd}}$ is the potential due to Van-der Waals interaction, $\vec{U_{el}}$ is electrostatic potential in the presence of charged particles, $\vec{U_s}$ = potential due to steric stabilisation and $\vec{U_{dep}}$ is the depletion potential. $\vec{U_{Vd}}$ is an attractive potential which can be expressed in terms of particle radius (r) and Hamaker constant (A) as:

$$\vec{U_{Vd}} = -\frac{A}{6}\left(\frac{2R^2}{2r^2 - 4R^2} + \frac{2R^2}{r^2} + \ln(1 - \frac{4R^2}{r^2})\right) \tag{2.42}$$

The Hamaker constant (A) is determined by the material properties of the particles and suspension medium. At two extreme conditions. a. when particles are close to each other (r $\sim$ 2R) Equation: 2.42 transforms to $U_{Vd} = -\frac{A}{12}(\frac{R}{r-2R})$ and when particles are at large inter-particle separations $U_{Vd} \sim -A(\frac{16}{9})(\frac{R}{r}^6)$. Thus, the attractive potential becomes infinite when particles are touching each other at r= 2R, this creates a potential minimum near this extreme which is greater than k_BT see Figure: 2.9. Suspended particles which are not stabilised will soon aggregate irreversibly under the influence of these strong attractions.

It is therefore necessary to provide some stabilisation mechanism providing repulsion potential greater than interaction. Two approaches are common for achieving this, electrostatic repulsion due to surface charge of particle and steric stabilisation.

Coulomb interaction between two charged particles, one finds a screened Coulomb interaction which exponentially decays in strength with distance. Suppose the particles are ionised. Overall charge neutrality will be maintained by a layer of counterions which will be attracted to the surface by the electrostatic field. Some of these counterions may be tightly bound to the surface (this layer of tightly bound ions is known as the Stern layer), but more will form a diffuse concentration profile away from the surface. There will be an electrostatic potential $\vec{U_{el}}$ at a distance r is given by:

$$\vec{U_{el}} = \pi\epsilon\epsilon_0 D\psi^2 \ln\left(1 + \exp^{-\kappa_{DL}r}\right) \tag{2.43}$$

where $1/\kappa_{DL}$ is the electric double layer thickness, ϵ and ϵ_0 is the dielectric constant of the medium and vacuum respectively and ψ is the surface potential.

Steric stabilisation is achieved by coating colloidal particles with layers of polymer. Many types of polymer are used for this purpose. The water based PMMA colloids used in this thesis were coated with PVP (MW=300,000) whereas oil based PMMA beads were chemically grafted with PHSA layer. Because of the difference in the type of polymer and chemical used for steric stabilisation of colloids the theory of charge and steric stabilisation are different. For e.g. in presence of polymer coated colloids, the close approach of these two coated particles causes compression of their interpenetrating polymer layers. The resulting strong repulsive force provides the steric stability. At larger interparticle separations, where layer interpenetration is still significant, more specific polymer-polymer interactions can be important. For coatings whose thickness is small compared to the particle radii the total polymer-polymer interaction occurs over a narrow range of interparticle spacing close to touching. Steric repulsion potential can be written as:

$$\vec{U_s} = \frac{4\pi RkT}{m}\phi_p^2(1/2 - \chi)(\delta - r/2)^2 \tag{2.44}$$

for $\delta < r < 2\delta$ and where m is the molar volume of solvent, ϕ_p is the volume of

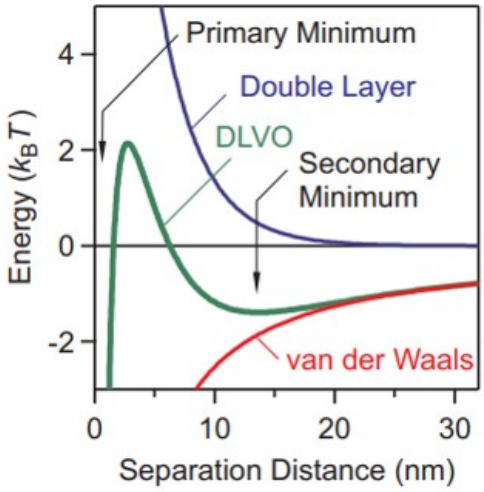

Figure 2.9 *Schematic of interaction potential between two hard-sphere colloids in an isotropic solvent.*

polymer molecules and k_B is the Boltzman constant and χ is the Flory-Huggins parameter. Depletion interaction is considered to be negligible in our system compared to colloid and nematic interaction. The different potential discussed above can be plotted as a function of particle separation (r), see Figure: 2.9.

Entanglement of Saturn-ring defects

In the section 2.4, the interaction energy between quadrupolar colloids in NLCs mediated by isolated Saturn-ring defects was discussed. However, as the concentration of particles in the nematic solvent increases, the number of defect lines surrounding them also increases, and the Saturn-ring defects are no longer isolated. The defects overlap, leading to different possible structures. Particles demonstrating a quadrupolar defect are weakly bound to LCs, and particle-particle interaction is mediated by the sharing of localized topological defects. Typically, the two colloidal particles are entangled by energy close to 10,000 k_BT [89]. When the experiments with the colloidal entanglement are performed in planar nematic cells where the liquid crystal is homogeneous, it is possible to entangle many colloidal particles into chains or colloidal wires. Guzman *et al.* [67] studied the orientation of topological defects in the presence of two closely placed quadrupolar colloids. They used dynamic field theory and numerical simulation to find a completely new three-ring structure instead of two separated Saturn rings. Araki and Tanaka followed this study further [10] and found a similar defect

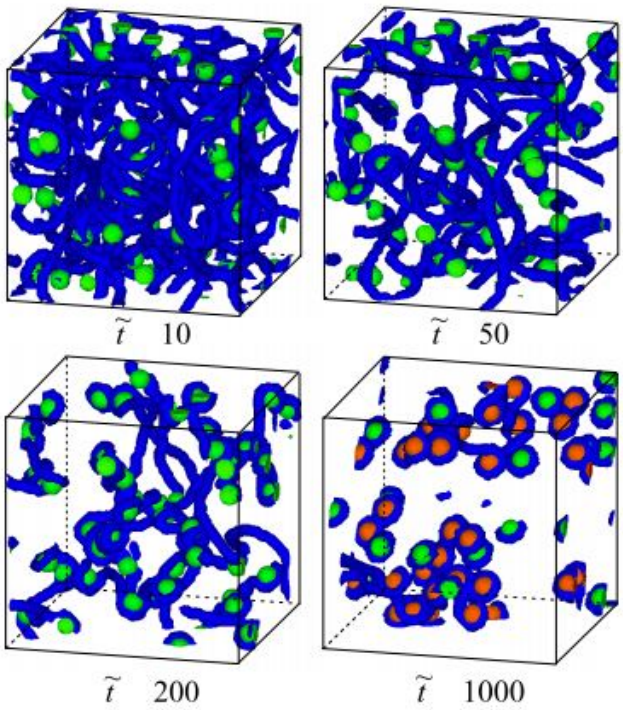

Figure 2.10 *The aggregation of many quadrupolar particles dispersed in nematic LCs. Blue lines represents the defect lines, green spheres are colloids and particles bound by disclination lines are drawn as red ones. Taken from [10].*

structure encircling the colloid in the form of figure eight. They showed that the particles are topologically arrested by a closed disclination loop and the particle centers, and their separation is $\frac{\Delta x}{2r} = 1.1$. Next, they showed the aggregation dynamics of a many-particle system, see Figure: 2.10. The simulation was carried out on a box of size 64^3, a total of 50 particles were immersed in nematic LCs at a volume fraction, $\phi = 0.0343$. At t=0, the system was quenched from isotropic to nematic phase in the absence of an external field. Nematic order took place just after the quenching with the appearance of defect lines. At t=10, particles trap the defect lines leading to the formation of elongated and entangled structure. However, when the elongated defect lines cannot support the tension arising from defect and viscous drag of the trapped particles, the entangled structure breaks. Moreover, isolated Saturn-ring defects are formed around individual particles, at t =1000, green spheres have isolated Saturn-ring defects around them, and red particles form topological arrested structure. It was noted that the population of isolated Saturn-ring defects was higher for dilute composites. This is attributed to the sizeable interparticle distance between particles exerting a higher tension on elongated defect lines leading to more frequent disconnection.

These numerical predictions were experimentally verified by using the laser tweezer technique to position two independent Saturn rings as close to each other as possible. Three entangled linear structures were formed with the rapid quenching of the nematic liquid crystal with colloidal particles: 'figure of eight,' 'figure of omega,' and 'entangled hyperbolic defect'. Compared to 'regular' elastic quadrupoles, all three provide for an order of magnitude stronger binding of particles in the direction of entanglement with the binding potential being of a string-like nature. Self-assembly by topological defects could be applied to other systems with similar symmetry. Entangled colloids are introduced as novel types of structures, where particles are topologically bound by delocalized defect loops, producing robust and possibly chiral structures. In these controlled conditions, the colloids assemble with defects entangling amongst each other, see Figure: 2.11.

The binding potential for the figure of eight structure is also shown in the Figure: 2.11d, inset shows the value of the force of entanglement as a function of particle separation (x) normalized to the particle diameter (d). It is observed that the binding force is of $\sim$ 10 pN and at the equilibrium state is the force of repulsion balances 0 as the force of entanglement. However, the binding potential of entangled colloids is $\sim$ 10000 k_BT, which is ten times greater than those created

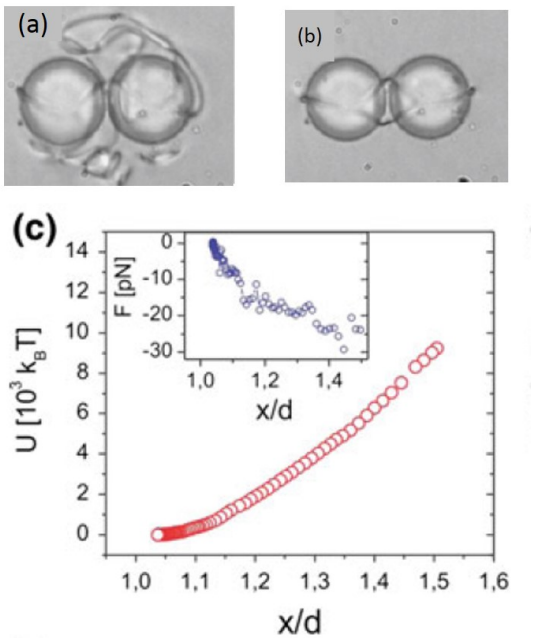

Figure 2.11 *Snapshot of two closely placed Satrun ring defect colloids (a) entangling of disclination loop before reaching equilibrium, (b) equilibrium entangled state forming figure of 8 around particle, (c) pair binding energy for the figure of 8 as a function of particle separation (x) normalised to particle diameter, D. [89].*

by isolated Saturn ring colloid pairs. The fundamental differences compared to non-entangled nematic quadrupolar colloids are: (a) defect loops that entrap and entangle particles, (b) a defect loop that entangles several particles has a topological charge that compensates the sum of the charges arising from all entangled particles, (c) shearing of a defect loops yield string-like behavior of the binding potentials, (d) an order of magnitude stronger inter-particle potentials along the direction of entanglement, (e) the possibility to spontaneously introduce chirality into non-chiral materials. By adding additional colloidal particles an array of particles are formed by manipulating the defect loops to continue the entanglement inevitably. Readers are directed to [35, 77] for a review on knot and link theory of multiple entangled quadrupolar colloids.

In this thesis, we are concentrating on dense quadrupolar colloids composites in nematic LCs, which gives rise to the entanglement of Saturn-ring defects, thus providing stability to the composites.

Chapter 3

Rheology

Complex fluids, unlike water, are Non-Newtonian and exhibit viscoelastic properties when exposed to external stresses. Different rheological models, the flow behavior of the complex fluid, and experimental rheometry will be described in this chapter. Rheological properties are extremely useful in the structural characterization of a colloid and medium, and the determination of how particle-particle interactions affect the stability of the mixture. An excellent introductory treatment of rheology is given by Barnes *et al.* [14]. A more fundamental treatment of colloid chemistry, including rheology, is given by Hunter *et al.* [75]. A material can be identified as viscous fluid or elastic solid, but, in everyday life, all materials have the property of both of these components, and they are classified as viscoelastic fluid. In an ideal viscous liquid, the energy of deformation is dissipated in the form of heat and cannot be recovered just by releasing the external forces, whereas, in an ideal elastic solid, the deformation is fully recovered when the stresses are released. Suspended particles in a viscoelastic material form the basis of most of the fast-moving consumer goods. In this thesis, we are concerned with investigating the consequences of the presence of particles on the rheological properties of nematic liquids, in particular, the shear viscosity and the non-linear viscoelastic properties. Before going into the experimental findings, a comprehensive review of the rheology principle is given, followed by the review of the rheology characteristics of different filled viscoelastic materials.

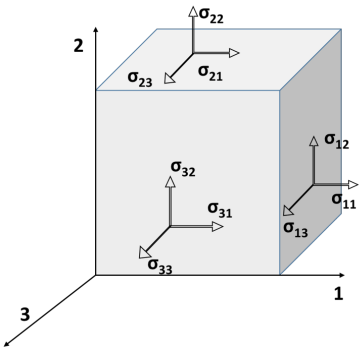

Figure 3.1 *Schematic representation of stress component acting on the faces of a cube. σ_{11} , σ_{22} and σ_{33} are normal components of stress and rest of σ_{ij} are tangential components.*

3.1 Rheology of continua

3.1.1 Stress tensor

The stress tensor, $\bar{\sigma_{ij}}$ in a continuous medium at a specific point under simple shear flow can be represented by a 3 X 3 matrix, given by

$$\sigma_{i,j} = \begin{vmatrix} \sigma_{11} & \sigma_{12} & \sigma_{13} \\ \sigma_{21} & \sigma_{22} & \sigma_{23} \\ \sigma_{31} & \sigma_{32} & \sigma_{33} \end{vmatrix} \tag{3.1}$$

Here i, j represents the orthogonal directions in the Cartesian coordinate system. The total force acting per unit volume in the presence of stress is represented by Equation: 3.2 where f_i is the body force [204]. The representation of various stress components acting on a cube of side L of a continuous medium is depicted by the Figure: 3.1.

$$f_i^* = f_i + \frac{\delta \sigma_{ij}}{\delta x_j} \tag{3.2}$$

In mechanical equilibrium condition, the total force acting on the medium becomes zero and rendering Equation: 3.3 as

$$f_i + \frac{\delta r \sigma_{ij}}{\delta x_j} = 0 \tag{3.3}$$

Equation: 3.3 is also known as Cauchy relation [61]. For a Newtonian fluid, this implies steady flow; for an elastic solid, it implies that the deformation of the body is not changing in time. In any material, the total stress tensor is the sum of both elastic and viscous stress given by:

$$\sigma_{ij} = -p\delta_{ij} + \tau_{ij} \tag{3.4}$$

where $\tau_{i,j}$ is viscous stress tensor, δ_{ij} is Kronecker delta and δ_{ij} =1 when i = j and 0 when i $\neq$ j and p is the mechanical pressure, $p = -1/3\sigma_{ii} = -\frac{1}{3}(\sigma_{11} + \sigma_{22} + \sigma_{33})$ [101].

3.1.2 Strain tensor

The state of deformation at a specific point on the application of stress is denoted by strain tensor, ϵ defined as the Equation: 3.5, where X(x,t) is the displacement of the material element at position x relative to a reference point [9].

$$\epsilon_{ij} = \frac{1}{2}\left(\frac{\delta X_i}{\delta x_j} + \frac{\delta X_j}{\delta x_i}\right) \tag{3.5}$$

It does not take into account the rotation of the medium as it does not change the relative position of the particles. Thus, one can define the strain rate tensor ϵ_{ij} as

$$\epsilon_{ij} = \frac{1}{2}\left(\frac{\delta v_i}{\delta x_j} + \frac{\delta v_j}{\delta x_i}\right) \tag{3.6}$$

The simplest strain and stress tensor constitutive relation for a simple shear flow is for Newtonian liquids where Equation: 3.4 translates to Equation: 3.7.

$$\sigma_{ij} = -p\delta_{ij} + 2\eta\epsilon_{ij} \tag{3.7}$$

where η is defined as the shear viscosity of the fluid. In the condition of simple shear flow, the velocity gradient is in 1 and 2 plane (see Figure: 3.1), thus Equation: 3.7 translates into a well known expression proposed by Newton, $\sigma_{12} = \eta\dot{\gamma}$ [110].

3.2 Types of fluids

Fluids can be classified as Newtonian or non-Newtonian depending upon the change in the value of their viscosity upon the application of external stress.

3.2.1 Newtonian fluid

The viscosity of a Newtonian liquid does not change on the application of stress, although it depends upon other factors like temperature and pressure. Isaac Newton was the first one to propose the basic relation between viscosity and stress for an ideal liquid under flow [14]. According to Newton's law of viscosity, the shear stress between adjacent fluid layers is proportional to the velocity gradient between the two layers. The ratio of shear stress to shear rate is a constant, for a given temperature and pressure, and is defined as the viscosity or coefficient of viscosity. Equation: 3.8 describes the Newtonian law of viscosity:

$$\sigma_{12} = \eta\dot{\gamma} \tag{3.8}$$

Some examples of common Newtonian fluids are water ($\eta_{No} = 0.001$ Pa.s), olive oil ($\eta_{No} = 0.1$ Pa.s) and honey ($\eta_{No} = 10$ Pa.s).

3.2.2 Non-Newtonian fluid

A non-Newtonian fluid exhibits a non-linear relation between the stress and strain tensor, implying that the Equation: 3.7 is no longer valid. The shear viscosity of these fluids is dependent upon the shear rate. Polymer solutions [12, 16], lamellar suspension, liquid crystalline suspensions [200], and molten polymers are non-Newtonian fluids. Detailed discussions on non-Newtonian fluids have been covered in several review articles and books [14, 75, 76]. A shear-stress versus shear-rate curve comparing Newtonian and non-Newtonian fluids is shown in the Figure: 3.2. Non-Newtonian fluids can be further classified as shear thinning, viscoelastic, dilatant, and thixotropic fluid. In this thesis, we are focusing on non-Newtonian fluids that have yield stress and exhibit shear-thinning properties.

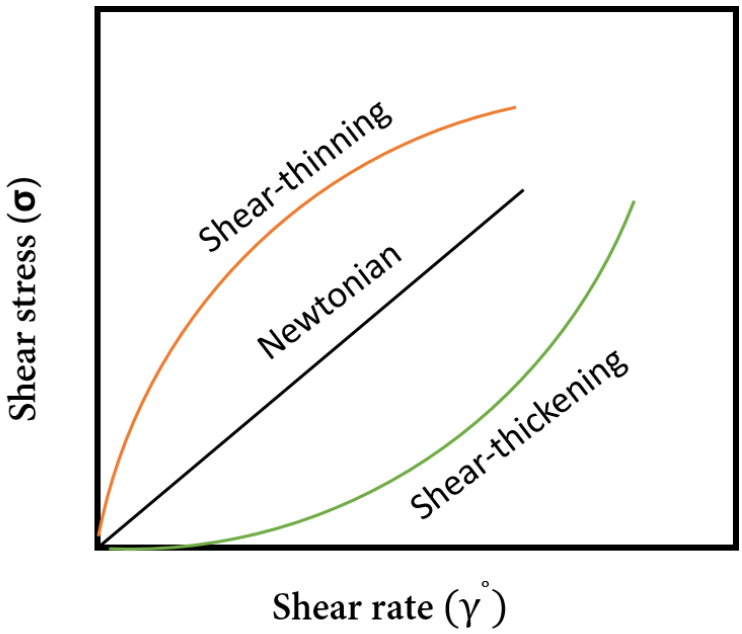

Figure 3.2 *Schematic stress curve of Newtonian, and non-Newtonian fluid.*

Shear-thinning fluids

The viscosity of shear-thinning fluids decreases with increasing shear rate. The nature of the curve is concave as represented schematically in the Figure: 3.2. Filled polymer solutions, dense, attractive colloidal suspensions [34, 76], and filled liquid crystalline composites are some examples of materials exhibiting shear-thinning properties.

3.3 Experimental rheometry

A rheometer offers an important tool to study the viscoelastic property of the material. Rotational rheometry also allows to control the stress and to record the angular velocity of the mobile part simultaneously. In this thesis, the viscoelasticity of colloids and liquid crystal composites were studied using a strain-controlled rotational rheometer - ARES G2. A rotational rheometer can be of two types: (a) strain-controlled where the strain rate is held fixed and the stress is deduced from the torque transmitted by the fluid, (b) stress-controlled, which can apply a force mode to material and measure the subsequent deformation. Figure: 3.3 shows the working principle of strain and stress-controlled rheometer [116].

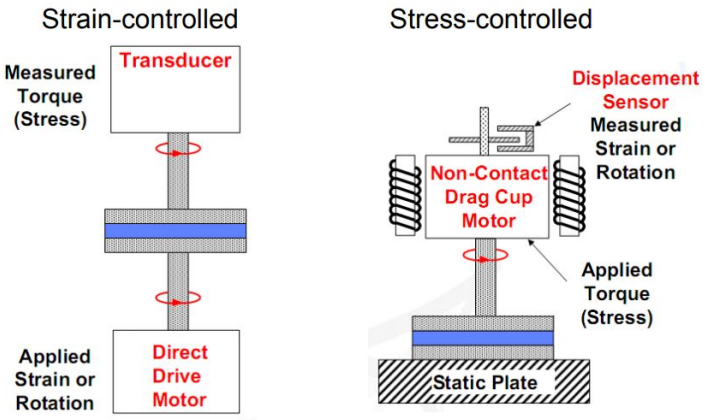

Figure 3.3 *Schematic of working principle of (a) strain controlled and (b) stress controlled rheometer [116].*

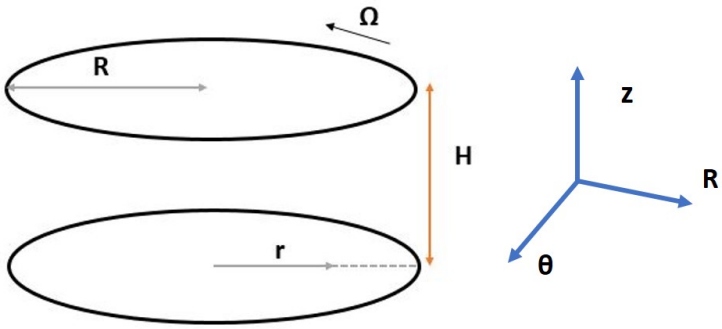

Figure 3.4 *Schematic representing parallel plate geometry, with disc radius R and gap between the disc denoted by H.*

3.3.1 Parallel-plate geometry

We have used a parallel plate, (PP), geometry for all rheology experiments because the gaps can be varied to accommodate a large size composite between the plates, unlike the cone-plate geometry, which must be operated at the gap for which it was designed. A schematic representing the parallel-plate configuration is shown in the Figure: 3.4. The sample is placed between two parallel-plates mounted vertically. PP fixtures exhibit maximum shear at the plate edges and zero along the vertical axis; that is, this geometry generates a radially inhomogeneous flow field. Thus the working Equation for torque, (τ), stress, σ, and shear-rate, $\dot{\gamma}$, in a schematic form and readers are directed to [116] for a detailed derivation.

The torque generated on the upper disk is measured as a function of the angular

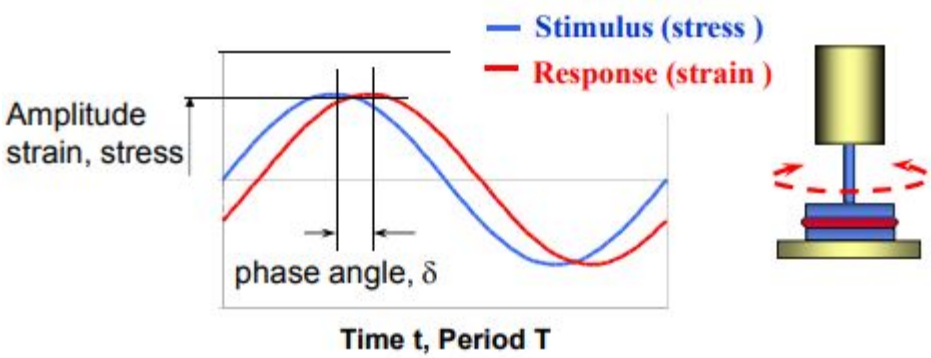

Figure 3.5 *Schematic showing stress and strain out of phase for viscoelastic fluids and parallel plate geometry used in standard rotational rheometer.*

velocity, Ω, of the lower disk. The maximum shear-rate at the disk edge is:

$$\dot{\gamma}_r = \frac{\Omega r}{H} \tag{3.9}$$

where H is the gap between the discs. The working Equation for torque (τ) and stress (σ) is given by:

$$\tau = \frac{\pi \Omega \eta R^4}{2H} \tag{3.10}$$

$$\sigma = \frac{\tau}{2\pi R^3}\left(3 + \frac{d\ln T}{d\ln \dot{\gamma}_r}\right) \tag{3.11}$$

It is also possible to measure the difference of normal stresses, $N_1 - N_2$ with parallel plates [116].

3.4 Small-amplitude oscillatory flow

The basic principle of oscillatory rheology experiment is that a sinusoidal strain ,γ, at a constant angular frequency ,ω, is applied to the sample to induce a sinusoidal shear deformation. The relation between stress, σ, and strain, γ, defines the property of the material. In oscillatory rheology, σ and γ vary sinusoidal with time with a phase difference of δ, where $0 < \delta < \pi/2$ (see Figure: 3.5) [37]. Using a standard rotational rheometer, the sample is placed between two parallel-plates, and a torque is applied, and a sinusoidal strain, γ, at a constant angular frequency, ω, is applied to the sample to induce a sinusoidal shear deformation. Thus, the

shear-rate varies sinusoidally given by the Equation: 3.12, whereas the shear stress varies sinusoidally as a function of frequency, ω, and an amplitude given by the Equation: 3.14. G' and G'' are linear viscoelastic material functions, respectively, referred to as the dynamic storage and loss moduli. Storage modulus, G', is the elastic term that gives the measure of the amount of energy required to deform the sample elastically, and loss modulus G'' is the viscous term which gives the amount of energy dissipated when the sample is deformed. Another term of importance is the ratio of loss to storage modulus, defined as loss tangent, $tan\delta = G''/G'$. And the ratio of loss modulus and angular frequency gives the value of kinematic viscosity, $\eta_{ke} = \frac{G''}{\omega}$.

$$\dot{\gamma} = \dot{\gamma}_o \sin(\omega t) \tag{3.12}$$

$$\sigma = \sigma_o \sin(\omega t); \tag{3.13}$$

$$\sigma = G'\omega \sin(\omega t) + iG''\omega cos(\omega t) \tag{3.14}$$

3.5 The rheology of complex fluids

The flow behavior of common complex fluid categories is reviewed to provide context for the rheology of the filled nematic composites reported in this thesis.

3.5.1 Rheology of colloidal dispersion

Colloidal particles, dispersed in an isotropic solvent such as water and oil, have gained a lot of attention in the past century because of their direct application in industry. Concentrated suspensions of particles in a low viscous matrix are well known in literature [12, 22, 34, 45, 55, 76, 84, 151, 152, 190]. They are relatively simple system, and their characteristics can give insights on the properties of a complex systems.

The linear viscoelasticity of dense colloidal dispersion near the glass transition ($\phi_g = 0.58$) has been studied by Mason and Weitz [122].

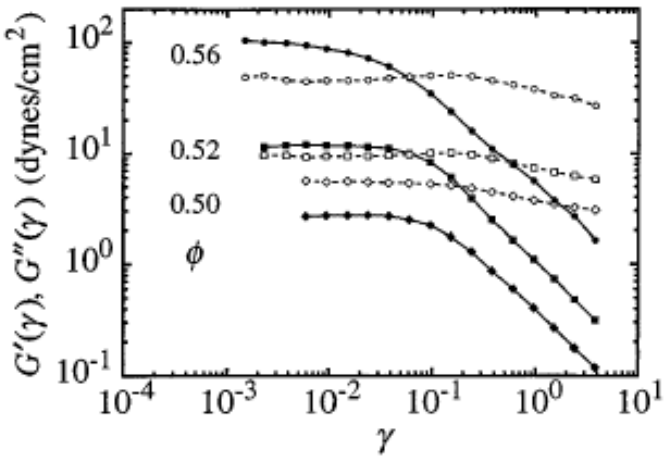

Figure 3.6 *The evolution of G' and G'' as a function of γ for different ϕ of uncoated silica spheres in ethylene glycol. The value of G' and G'' increases with the concentration of silica microspheres.[122]*

Oscillatory sweep

The oscillatory strain sweep of a dense suspension of silica microspheres in ethylene glycol is shown in the Figure: 3.6. The suspension starts to show elastic behavior, $G' > G''$ at $\phi \geq 0.52$. However, the value of yield strain, γ_c, where the crossover of G' and G'' occurs, decreases with increasing ϕ. The linear viscoelastic regime (LVR) for dense silica suspension is limited by low strain values, $\gamma \sim 0.1$. The frequency sweep is studied within the LVR. Figure: 3.7 shows the frequency sweep curve for silica suspension. It is observed that the storage moduli increase with frequency before plateau near the glass transition, ϕ_g, however, G'' exhibits a definitive minimum at low frequency before linearly increasing with frequency, $\sim \omega$. G' dominates G'' as the concentration increases over a certain range of frequency, $\omega \leq 10$ rad/s. But at a higher frequency, the rise in G'' is greater than G', and the viscous property takes over.

To explain the behavior of G' and G'', Mason and Weitz proposed a model based on the relaxation of density fluctuations of the spheres [192]. At high frequency, i.e. at short times, the relaxation of the density fluctuation reflects the localized motion of the individual spheres, entailing the full details of the hydrodynamic interactions. However, at low frequencies and at longer times particles are trapped in cages formed by the neighboring particles. The evolution of these cages with concentration determines the behavior of G' and G'' as a function of frequency. At concentration, $\phi < \phi_g$, cages can break slowly with $G'' > G'$, however at $\phi > \phi_g$ these cages do not break leaving the system more elastic. Cage dynamics

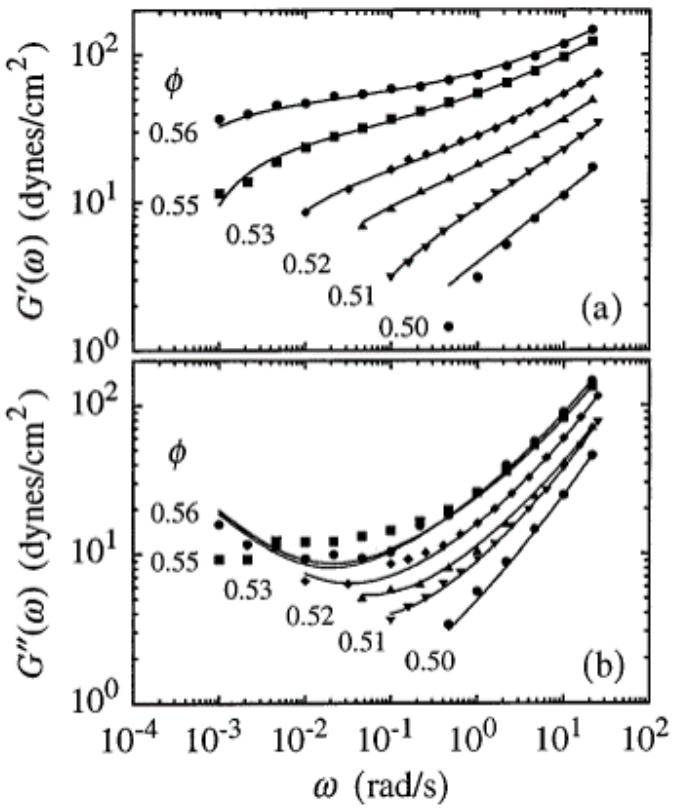

Figure 3.7 *The evolution of G' and G'' as a function of ω for different ϕ of uncoated silica spheres in ethylene glycol. The value of G' and G'' increases with the concentration of silica microspheres. [122]*

can be described by mode-coupling theory, and readers can refer to [40, 62] for details on theory and derivation, which is based on the light scattering data from hard spheres near the glass transition. Combining the mode-coupling theory and the effects of energy storage due to Brownian motion, the expression for G' can be written in the form Equation: 3.15; where τ_D is the diffusion time, c is the numerical constant, g(2a, ϕ) is the radial distribution function given by $\frac{0.78}{0.64-\phi}$ [122]. The elastic modulus has a contribution from thermal motion, the concentration of the colloidal particles (ϕ), and diffusion time as well on the applied angular frequency (ω).

$$G'_D(\omega) = c(\frac{k_B T}{a^3})(\phi^2)g(2a,\phi)(\omega\tau_D)^2 \tag{3.15}$$

The loss modulus is composed of two components and is linearly dependent on ω , such that$G''_D = G'_D + \eta\omega$, where η is the suspension viscosity. It has been shown by simulation that both G' and G'' diverge at $\phi = 0.64$, i.e. at random close packing [**?**]. In summary,

- $G' > G''$ with $G' \propto \phi^2$ at $\phi \geq 0.52$.
- G' has a linear viscoelastic plateau with $G' \sim \omega^0$ when $\phi \sim \phi_g$.
- G'' linearly increases with frequency, $G'' \sim \omega$ at $\phi \geq \phi_g = 0.58$.

Flow behavior

Three concentration regimes for determining flow properties of colloidal suspension were identified by Rutgers and Thomas [168]. These are (a) a dilute regime, restricted to $\phi < 0.1$ colloidal volume fractions, the viscosity showed linear behavior independent of shear-rate thus the rheology is Newtonian like [110], (b) the semi-dilute regime, $0.1 < \phi < 0.25$, where viscosity showed a higher-order dependence on ϕ, but the behavior is still approximately Newtonian and (c) the concentrated regime, $\phi > 0.25$, characterized by the rapid growth of apparent viscosity and increasingly non-Newtonian behavior (particularly shear-thinning) with volume fraction, ϕ. Einstein addressed the viscosity behavior theoretically for the dilute regime [52]. The equation is mathematically written as $\eta = \eta_o(1 + k\phi)$, where η is the measured viscosity, η_o is the Newtonian continuous phase viscosity, and k is called the intrinsic viscosity, which is calculated to be 2.5 for

hard spheres. This equation is only valid for dilute suspension at $\phi < 0.1$. The mechanics of dilute and semi-dilute suspensions are well understood, primarily due to the work of Einstein[52], Batchelor [18], and Batchelor and Green [19]. But, since in this thesis, we are dealing with a range of filler volume fraction from dilute to concentrated suspension, $0.1 \geq \phi \geq 0.5$ we use a semi-empirical relation proposed by Krieger and Dougherty [76]. The equation form of Krieger-Dougherty relation is given by Equation: 3.16, ϕ_m is the maximum packing fraction.

$$\eta_r = [1 - \frac{\phi}{\phi_m}]^{-k\phi_m} \tag{3.16}$$

The viscosities of suspensions consisting of uniform-size rigid spherical particles as a function of varying concentrations were measured by Chong *et al* and group [34]. The viscosities of colloidal suspension consisting of uniform-size rigid spherical particles were measured by Robinson [20] and Rutgers [168]. The effects of particle size distributions on viscosities have been investigated by Roscoe [165], Luckham [112], Parkinson [144] Sweeney, and Eeson. They studied the viscosity curve for a range of volume fraction of silica spheres in an isotropic solvent. The plot of relative viscosity as a function of ϕ is shown in Figure: 3.8, the linear theoretical relation is followed up to $\phi \leq 0.45$. However, these isotropic suspensions follow the Krieger-Dougherty relation up to random close packing (RCP) fraction of dense colloidal suspension.

The stress versus shear-rate curve for large (D $\sim 2000\ \mu$m) glass-sphere suspension at $\phi < \phi_g = 0.479$ and $\phi \sim \phi_g = 0.579$ is shown in Figure: 3.9. The curve is fitted with a Herschel-Bulkley relation. This model was developed by Herschel and Bulkley [71] specifically for describing shear-thinning fluids with yield stress. This model gives an empirical relation between shear stress σ and shear-rate $\dot{\gamma}$ denoted by the Equation: 3.17 where σ_y is the yield stress, k is a constant and n is the index < 1 for shear-thinning fluid and > 1 for the shear-thickening system. Both the hard-sphere suspensions have a value of n < 1, proving that dense suspensions exhibit shear-thinning behavior.

$$\sigma = \sigma_y + k\dot{\gamma}^n \tag{3.17}$$

In summary:

- The relative viscosity of colloidal suspensions follows the Krieger-Dougherty

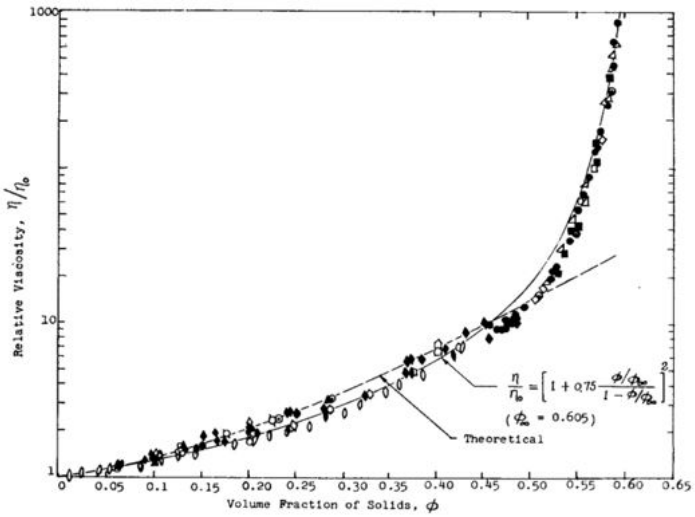

Figure 3.8 *Relative viscosity of colloids in isotropic solvent, Straight line depicts the linear relation between relative viscosity and volume fraction and curved line is the curve from Kreiger-Dougharty relation. [34]*

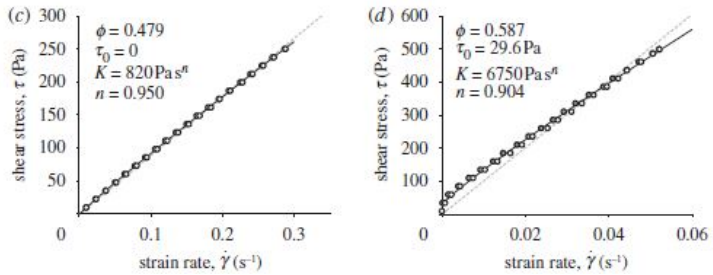

Figure 3.9 *Stress versus shear-rate curve for suspension of glass spheres (2000 μm) , at intermediate and high ϕ, the suspension viscosity depends on strain rate (shear-thinning, $n < 1$); at the highest ϕ, the suspensions are shear-thinning, and show additionally an apparent yield stress τ_0. Graphs are fitted with Herschel-Bulkley Model [71].*

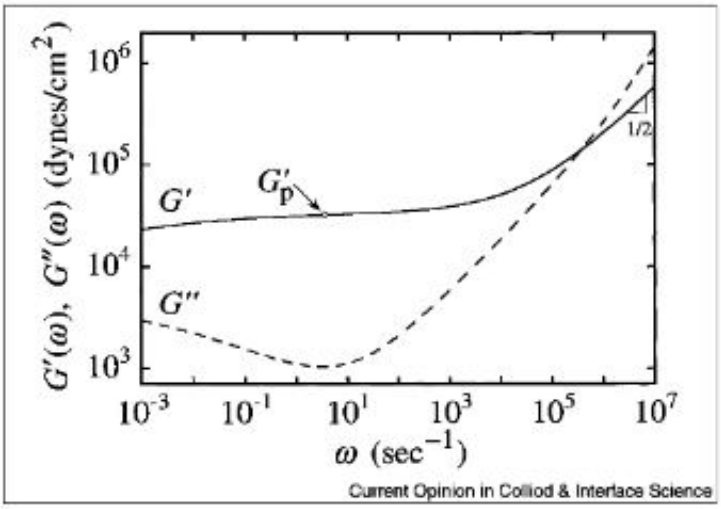

Figure 3.10 *the mechanical spectrum of dynamic moduli as a function o frequency for dense emulsion, $\phi = 0.8$, at low frequency G' plateaus and is greater than G'' before increasing as $\omega^{1/2}$ at high frequencies, however the G'' shows a definite minimum at intermediate frequency before increasing as ω and overtaking G' at higher frequencies. Taken from [120].*

relation up to RCP.

- Colloidal suspensions are shear-thinning, however at the highest $\phi \sim 0.58$ with the value of index $n \sim (0.70 - 0.95)$, there is a presence of yield stress.

3.5.2 Emulsion rheology

Emulsions are dispersions of two immiscible liquids such as oil droplets in water as a continuous medium stabilized with the addition of an inetrfacial stabiliser, such as surfactant [15]. Emulsion rheology plays a very important role in the processing of personal care [127], food, pharmaceutical, and paint industry. There have been some excellent reviews on the rheology of emulsion by Tadros [184] , Sherman [175], Madiedo [24], Carmen [113] and Barnes [17]. In this section, we will be discussing the rheology of concentrated PDMS emulsion.

Oscillatory rheology

The linear viscoelasticity of mono-disperse emulsions have been studied by Mason *et al.* [120]. At concentration, $\phi \leq \phi_g$ both the dynamic moduli exhibit the

response similar to hard-sphere glassy suspension [122] with G' exhibiting a plateau and G'' linearly increasing with frequency. However, at concentration greater than the glass transition, the behavior is different. Mason [120] studied a silicone oil-in-water emulsion with $\phi = 0.8$ and size of the droplets, a = 0.5 μm over nine decades of frequency (10^{-3} to 10^{7}) rad/s, see the Figure: 3.10. The plot suggests at low frequency, G' dominates over G'' and exhibit a linear viscoleastic plateau before increasing as $\omega^{1/2}$ at high frequency, $\omega > 10^{5}$ rad/s. the increase in G' was explained by slipping motion of the un-packed droplet structures [43, 109]. However, the loss modulus, G'', exhibits a definite minimum at intermediate frequency because of the slow glassy relaxation in the droplet structure before linearly increasing with frequency and finally overtaking G' at high frequencies, $\omega > 10^{5}$ rad/s.

The universal volume fraction, ϕ, dependence of the value of linear viscoelastic plateau value of G' is described by:

$$G'(\phi) = 1.5 \left(\frac{\sigma}{a}\right) (\phi - \phi_{RCP}) \tag{3.18}$$

where σ is the interfacial tension between oil droplets and water, a is the droplet radius and ϕ_{RCP} is the volume fraction at random close packing = 0.64 [121].

Flow rheology

Saiki and group [171] studied the flow rheology of concentrated, $\phi \geq 0.50$ PDMS emulsions in water. They investigated the effect of droplet deformation on the shear viscosity of the emulsion made from two different viscosities PDMS, 0.3 cP and 0.45 cP. For a plot of shear viscosity as a function of shear-rate for PDMS(0.3) emulsion exhibiting shear-thinning behavior, see Figure: 3.11. The data were fitted using the power-law equation. The power-law model was proposed by Ostwald [198],[141], and de Waele [140] and has since then been fully described by Reine [162]. It relates the two parameters of the viscosity curve (η and $\dot{\gamma}$) written in the form of an Equation: 3.19 where k is called the consistency and n_{PL} is the power-law index calculated from the slope of viscosity curve. The power-law index is a dimensionless quantity with a value of 1 for Newtonian liquid and tending towards 0 for shear-thinning non-Newtonian fluids. The power-law index reflects the structural changes occurring within the emulsion on the application

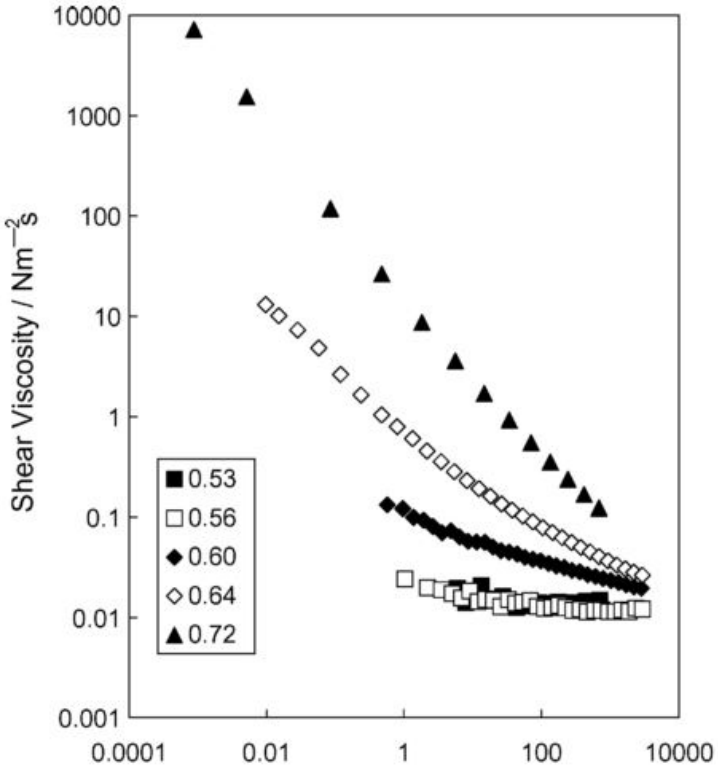

Figure 3.11 *Shear thinning plot of PDMS (0.3) emulsion for different volume fraction. [171]*

of shear. For highly shear-thinning fluid, the power-law index ≈ 0.2 - 0.3.

$$\eta = k\dot{\gamma}^{(n_{PL}-1)} \tag{3.19}$$

The power-law index, n_{PL}, was found to be less than 1 stating that the PDMS emulsions show shear thinning property.

The relative viscosity, ($\eta_r = \frac{\eta_\phi}{\eta_{media}}$) for different ϕ was studied and the plot comparing PDMS emulsion with hard-sphere silica suspension is shown in Figure: 3.12. It was observed that both PDMS emulsion and silica suspension show identical behavior at low concentration, $\phi \leq 0.4$ but as the concentration is increased, the relative viscosity (η_r) deviates from Kreiger-Dougharty fit. Thus it was concluded that at low concentration ($\phi \leq 0.4$) regime droplets do not touch each other and do not get deformed. At higher concentrations, due to particle-particle interaction and hydrodynamic stress, droplets get deformed. The collision between droplets causes frictional forces between them in addition to hydrodynamic interaction. The droplet deformation was quantified using the capillary number, N_{Ca}, which is the ratio of hydrodynamic stress and interfacial

tension mathematically written as:

$$N_{Ca} = \frac{\eta_{media} r \dot{\gamma}}{\sigma} \tag{3.20}$$

where η_{media} is the viscosity of the dispersion media, r is the droplet size, and $\dot{\gamma}$ is the shear-rate. Torza *et al.* [186] have derived an empirical equation for calculating the droplet deformability. It is based on the ratio of N_{Ca} and η_{media}.

$$\frac{L-B}{L+B} = \frac{5(19K+16)}{4(K+1)\sqrt{\frac{20}{N_{Ca}} + (19K)^2}} \tag{3.21}$$

where K = $\frac{N_{Ca}}{\eta_\phi}$ and L and B are the longer and shorter axis of the deformed droplets. It can be seen the the equation is directly proportional to η_ϕ, thus as the concentration of droplets increase the steady state shear viscosity will increase and the droplet deformation will be higher. Now from Figure: 3.12 it is observed that PDMS (0.3 cP) emulsion deviates from hard-spheres at $\phi \geq 0.4$ whereas PDMS (0.45 cP) emulsion deviates at $\phi_g = 0.58$. This discrepancy was further explained by hydrodynamic interactions in addition to collision between spheres. The hydrodynamic force between two spheres is, $F = \frac{6\pi\eta_{media}\dot{\gamma}r^3}{H}$, where H is the particle separation and can be evaluated from volume fraction, ϕ. $H = 2r[\frac{(\phi_{max}}{\phi})^{1/3} - 1]$. Putting $\dot{\gamma}$ =1000/s, $\phi_{max} = 0.68$ and r = 0.86μm and ϕ =0.4 the hydrodynamic force comes out to be 10 μN/m and critical deformation force, $F_{crit} \sim 20$ μN/m for PDMS (0.3) emulsion and 200μN/m for PDMS(0.45) emulsion. Thus, the hydrodynamic forces are supressed for PDMS (0.45 cP) emulsion and only particle interaction gives rise to droplet deformability whereas for lower visocisty PDMS (0.3 mPa.s) emulsion, hydrodynamic forces play a bigger role and the deviation from Kreiger-Dougharty relation occurs at $\phi < \phi_g$. Deformation can allow particles to move past each other easily on the application of shear, hence the emulsion will have low viscosity as compared to hard sphere suspension at the same volume fraction. The deviation from hard-sphere suspension for PDMS(0.45) emulsion is at $\phi = 0.58 = \phi_g$. ϕ_g is the glass transition volume fraction at which particles are caged by their neighbors which affects their rheology behavior.

In summary:

- At $\phi \leq \phi_g$ emulsion shows viscoelasticity behavior similar to hard-sphere

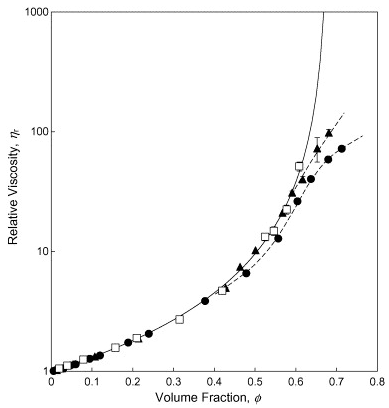

Figure 3.12 *Curve of relative viscosity (η_r) at $\dot{\gamma} = 1000/s$ as a function of ϕ for PDMS (0.3);closed circle, PDMS (0.45);closed triangle and silica spheres; open square. The line represent Kreiger-Dougharty fit[171], dotted line is from the theory proposed.*

glassy suspension, with $G' \sim \omega^0$ and $G'' \sim \omega$.

- At $\phi > \phi_g$, for frequency range ($\omega < 10^5$ rad/s), G' dominates G'' exhibiting a plateau however at $\omega > 10^5$ rad/s, $G' \sim \omega^{1/2}$. G'' shows a definite minimum at imtermediate frequencies before linearly increasing at higher frequencies.

- Emulsions also exhibit shear-thinning behavior beyond the glass transition.

- Both hard-sphere and emulsion show identical flow behavior at low concentration, $\phi \leq 0.4$, but as the concentration is increased, the relative viscosity (η_r) of emulsion deviates from Krieger-Dougherty fit beyond $\phi \geq 0.58$ because of droplet deformation.

3.6 The rheology of elongated structures (polymer and worm-like micelles).

A polymer is a macromolecule made from many repeating sub-units or monomer; in greek polymer means 'many parts'. They can be both synthetic polymer, for e.g. polystyrene, polyethylene, etc. and natural polymers like proteins, hemp, silk, etc. They are viscoelastic materials and are ubiquitous in our day to day life with a wide range of applications. For example, polystyrene is widely used in the packaging industry, glyptal is used for making paints and coatings, bakelite is used for making electrical switches and insulator, etc. Polymers are also used

in the personal care industry in the form of emulsifier, thickening agent, and rheology modifier [2]. Depending upon the state and concentration, polymers can be classified into:

1. Dilute solution: When a small amount of polymer, ($\phi \leq 0.1$), is added to a solvent and the motion of one polymer chain does not affect other than the polymer solution is diluted.

2. Semi-Dilute solution: When the concentration of polymer in the solvent is increased, such that the dispersed polymers in solvent just begin to touch each other at $0.1 \leq \phi \leq 0.4$.

3. Concentrated solution: When the concentration of polymer increases with $\phi \geq 0.4$, they began to overlap among leading to an entangled structure.

4. Molten polymer: A state of pure polymer which has been exposed to high enough temperature so that it melts. Molten polymers are always in motion and full of entanglements.

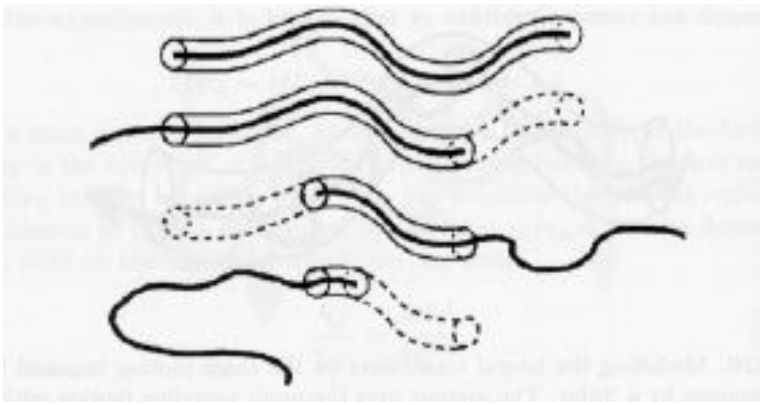

Figure 3.13 *Decomposition of the tube resulting from a reptative motion of the primitive chain. The parts which are left empty disappear. [12, 60]*

The elastic property of polymer melts was attributed to their entangled structure [28], [189]. The tube model proposed by Edward and Doi in 1967 [119] was the first model describing the dynamics of the entangled polymer network. According to this model, each polymer is confined in a tube-like region, and its motion is restricted by surrounding chains. A tube interaction potential was given for topological interaction. De Gennes in 1971 proposed that polymers do not move tangentially to the tube but move predominantly along the tube i.e., they reptate. This is the reptation model of polymer [60]. The motion of the surrounding chains

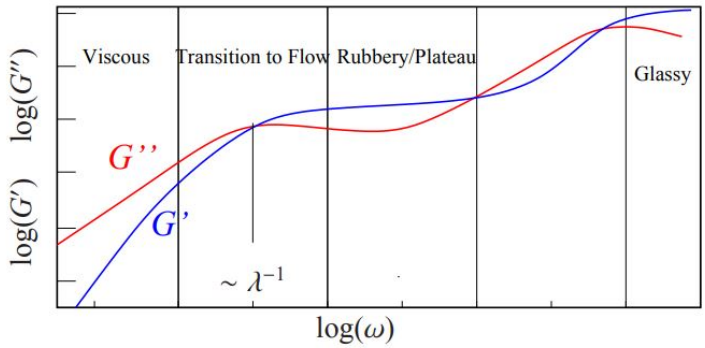

Figure 3.14 *Curve of G' and G'' as a function of frequency for polymeric melts [88].*

leads to the reorientation of the polymers. The reptation model was applied to the rheology of the entangled polymer by Doi and Edward. Their predictions are in agreement with the experimental findings.

3.6.1 Oscillatory response

To understand the elasticity of polymers, their structure can be considered as a spring that stretches and recoils. Recoil results from the elastic energy being stored during the restoration process. Polymers are not completely elastic, so it is important to study their linear viscoelastic response through rheology.

The general oscillatory response of a polymer melt system over a wide range of frequency is shown in the Figure: 3.14 [88]. The curve has four different regimes where dynamic moduli are exhibiting different frequency responses.

1. Viscous response at low frequency:
   At low frequency, the response is always viscous with $G'' > G'$. In this region, G' increase is quadratic with ω as $G' \approx G\lambda^2\omega^2$ whereas G'' increases linearly with ω as $G'' \approx \eta_0\omega$. This behavior is typical of Maxwell Fluid.

   The Maxwell model for viscoelastic fluids gives a relation between dynamic moduli (G', G'') and angular frequency (ω). Figure: 3.14 shows the oscillatory frequency sweep of a typical Maxwell fluid [12, 14, 16]. The storage (G') and loss moduli (G'') in terms of frequency are given by Equation: 3.23, where ω is angular frequency and λ is the relaxation time $= \eta/G''$.

$$G' = \frac{G(\omega\tau)^2}{1+(\omega\tau)^2}; \tag{3.22}$$

$$G'' = \frac{\eta\omega}{1+(\omega\tau)^2} \tag{3.23}$$

However, as the applied frequency is increased, G' begins to dominate, and solid-like behavior prevails. The determinant of which kind of behavior is determined by Deborah number, D_e which is the ratio of the relaxation time to the test time. The measure of $D_e = \omega\tau$. Hence, low Deborah numbers always indicate liquid-like behavior, whereas high Deborah numbers mean solid-like response. At the midpoint, where G'' goes through a maximum; $G' = G''$, and this takes place at a critical crossover frequency of $\omega = 1/\tau$, where τ is the relaxation time of the polymer. Some of the most common Maxwell fluids are a polymer that is used as a thickening agent such as hydrophobic ethoxylated urethane and worm-like surfactant micelles [181]. All polymer solutions exhibit Maxwell fluid-like behavior at low frequency but it is not always detected because some materials take a very long time to relax back to their original shape. The relaxation time can be calculated from the crossover of G' and G''.

2. Rubbery plateau:
   In this region, the elastic property dominates with $G' > G''$. G' shows a plateau independent of ω. A schematic curve of G' for different polymer systems is shown in the Figure: 3.15. The plateau region is clear and pronounced in high molecular weight polymers (with entanglements) in the concentrated solution and the melt states. Cross-linked polymers have a wide and predominant plateau region [88]. The link between the plateau region and the cross-linking suggests that the entanglement acts like a kind of constraint (like the cross-links) to the motion of the polymer contour, leading to the plateau region. Untangled melts do not have any plateau region, and directly make the transition to the Maxwell region.

3. High-frequency cross over-region:
   At high frequency also due to relaxation and dissipation mechanisms, the value of $G'' > G'$ again giving rise to a second-crossover frequency where $G' = G''$.

4. Glassy region:

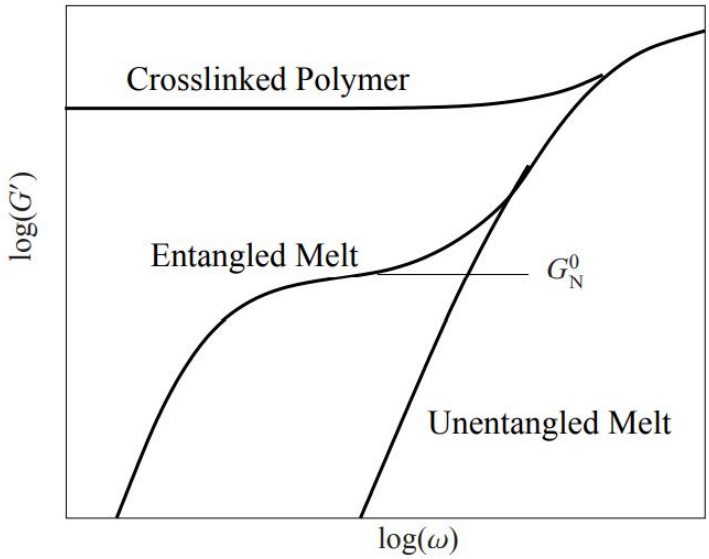

Figure 3.15 *G' response at low frequency for different polymers [88].*

At very high frequencies, the glassy behavior takes over with $G' > G''$ [174].

On a standard rotational rheometer, the range for a frequency sweep experiment is from 10^{-2} to 10^{2} rad/s. Thus, out of the above mentioned viscoelastic behavior, only two regions are usually seen depending upon the relaxation time of the material. If $\omega\tau \approx 1$, then viscous response and transition to flow is observed. But when $\omega\tau > 1$, a plateau region is observed with $G' > G''$ and when $\omega\tau < 1$ viscous response always dominates with $G'' > G'$.

3.6.2 Flow behavior

Zero shear-rate viscosity

The zero shear-rate viscosity , (η_{00}), is the viscosity of the polymer when shear-rate $\dot{\gamma} \to 0$.

- For dilute solution, $\eta_{sp} = \frac{\eta - \eta_s}{c\eta_s}$, where η_s is the viscosity of the solvent and c is the concentration of the polymer. It can be seen that the viscosity of dilute polymer solutions, η varies linearly with concentration.
- For semi-dilute solution, the specific viscosity, η_{sp} varies quadratically with concentration. $\eta_{sp} \sim c^2$.

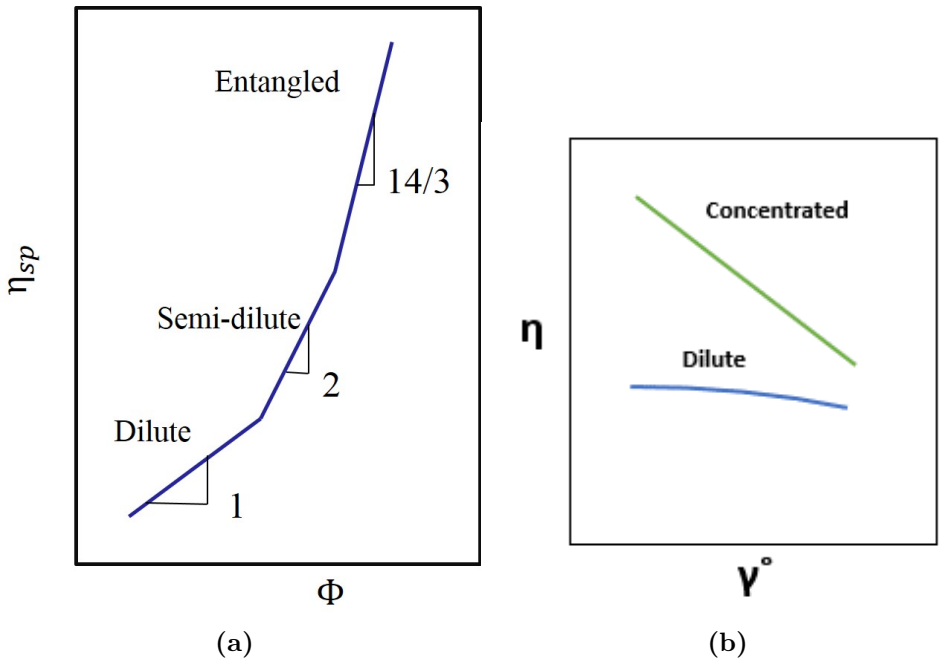

Figure 3.16 *(a) Scaling of the specific viscosity (η_{sp}) with concentration of polymers. The first transition denotes the semidilute regime and the second corresponds to the entangled regime [115], (b) Schematic of shear-thinning behavior with concentration of polymer.*

- In the concentrated and molten polymer state, which has entangled structures in them, the viscosity has a higher dependence on concentration. $\eta_{sp} \sim c^{3.4}$ [115]. Also the relaxation time, $\lambda_c \sim c^{3.4}$. This is because the relaxation time depends on the linear size of the polymer giving a direct bearing to the concentration and molecular weight of the polymer.

Shear-thinning behavior

The viscosity of polymer solutions decreases with increasing shear-rate, thus exhibiting shear thinning property. The shear-thinning rate is higher for a concentrated solution as compared to a dilute one. Figure: 3.16 shows the pronounced shear-thinning behavior for concentrated polymers as compared to dilute polymer solutions [16], [12]. In a concentrated solution, polymers entangle to form a network-like structure. These entanglements act like a node with energy dynamics equivalent to that of a covalent bond, thus restricting the motion of polymer. On the application of shear, these network structures begin to detangle and align along the direction of flow, thus providing less constraint to flow and exhibit shear thinning behavior.

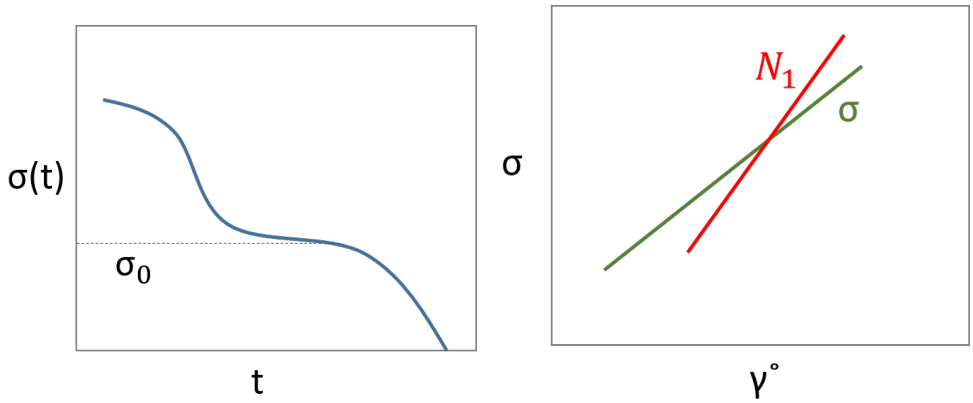

(a) (b)

Figure 3.17 *(a) Schematic representing stress relaxation behavior in concentrated polymer solution, (b) Schematic of the Normal stress (N1) curve as a function of shear-rate, it can be seen that the value of N1 becomes greater than the shear stress at higher shear-rate.*

3.6.3 Stress Relaxation

In the stress relaxation measurement, a constant strain is applied, and the decay of stress to the equilibrium value is studied. A schematic diagram of stress relaxation [88] is shown in Figure: 3.17. At the beginning of a small-time response, the polymer shows glassy behavior with a plateau at σ^0. The response is elastic at small time scales but the solutions begins to flow at large time scales.

3.6.4 Normal stress

The normal stress has two components defined by; $N_1 = \sigma_{11} - \sigma_{22}$ and $N_2 = \sigma_{22} - \sigma_{33}$, see Figure: 3.1, where 1 is the flow direction, 2 is the flow gradient direction and 3 is the vorticity direction. The difference between normal stresses for an isotropic liquid is zero. N_2 is usually zero for polymeric liquids, however, the value of N_1 can become larger than the value of shear stress for concentrated polymer solution and melts represented in the Figure: 3.17 b. The existence of N_1 for polymer fluids is because of the anisotropy in its molecular structure under flow. For example, when a polymer is in the equilibrium position, it is coiled up and at rest, but on the application of shear, the coiled structures recoil and stretch to align towards the shear direction. This results in an elongated structure with the restoring force in 11 and 22 planes to be of different values. These different plane restoring forces gives rise to normal stresses.

3.7 The rheology of filled polymers and their solutions.

Many different types of fillers are added to modify the mechanical properties of the material, enhanced durability, or cutting the cost of processing. Carbon fibers are added to polymers for enhanced strength and conductivity; particles are added in rubber to enhance its toughness, calcium carbonate is added to toothpaste formula for whitening effect on teeth, silica particles are added in cosmetic product to act as abrasives. Fillers can be metal, non-metal, organic, or inorganic compounds. They can have different shapes, sizes, surface charges, density, conducting properties, etc. These are carefully chosen to answer the needs of the formulation. In this thesis, we are concentrating on spherical fillers. Readers can refer to [174] for a detailed description of different types of filler particles, and their rheology behavior in polymer melts.

3.7.1 Active and In-active filler

Fillers can be broadly divided into two categories: active and in-active, often called passive depending upon their interaction with the dispersion medium. Active fillers strongly interact with the dispersion matrix, implying a strong mechanical reinforcement of the network, thus enhancing the gel strength [169]. The passive filler reduces the strength [47]. The effect of the filler also depends upon the value of both the moduli, G' and G'', the higher the elastic moduli of the dispersion matrix, the less the effect of the active filler, but the greater the effect of the inactive filler (and vice versa). This was discovered by Dickinson *et al.* [48], who studied the viscoelastic properties of heat-set whey protein emulsion gels containing protein-covered droplets and surfactant-covered droplets.

3.7.2 Rheology of filled polymer system

The rheology of filled polymer composites has been extensively studied by Barnes [16] and Shenoy [174]. Modeling of the rheological behavior of filled systems has been reviewed in depth by Shenoy [174], Macosko [116], and Han [69]. The main factors affecting the rheology of filled polymer composites are size, shape, nature, surface charge of the filler, the intrinsic viscosity of the polymer, and the

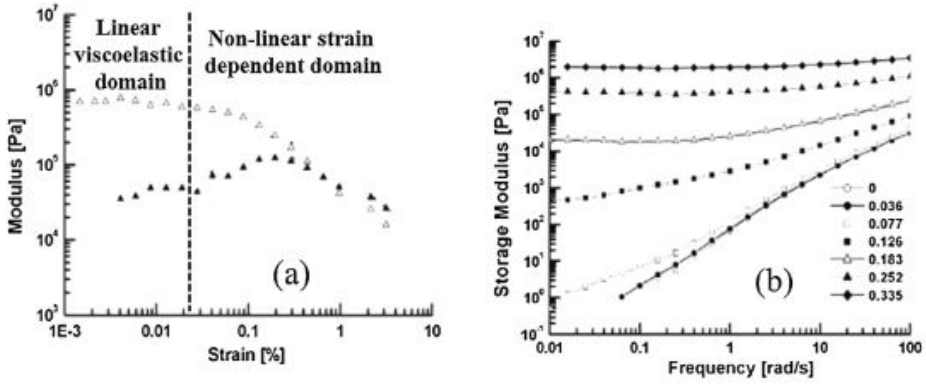

(a) **(b)**

Figure 3.18 *(a) Oscillatory strain sweep of $\phi = 0.252$ of $Mg(OH)_2$ in Poly(ethylene-co-octene) composites. (b) Frequency sweep of different ϕ values of $Mg(OH)_2$ in Poly(ethylene-co-octene) composites [118].*

maximum packing fraction of the filler.

3.7.3 Oscillatory response

An oscillatory strain sweep curve of $\phi = 0.252$ $Mg(OH)_2$ in Poly(ethylene-co-octene) composites is shown in Figure: 3.18 [118]. It is observed that beyond $\gamma = 0.8\% = \gamma_c$, the LVR regime is broken, and G' drastically decreases while G'' displays a maximum. All filled polymer systems exhibit non-linear response after a certain value of strain, γ_c. The value of yield strain, γ_c decreases with increasing ϕ. It has also been observed that as the value of ϕ increases, the extent of the linear viscoelastic regime decreases [31]. The value of storage and loss moduli systematically increases with the value of ϕ in the polymer [50, 70]. The increase in G' is attributed to the increase in rigidity of the composite on the addition of solid microspheres, whereas the increase in G" is due to the more pronounced dissipation process occurring at higher ϕ. Faulkner and Schmidt [51] first gave the relation between G', G'', and volume fraction ϕ. They conducted oscillatory strain sweep experiments on glass beads filled polystyrene system up to $\phi = 0.26$ and coined the expression for G' and G'' given by Equation: 3.25.

$$G'(\phi, \omega) = G'(0, \omega)(1 + 1.8\phi); \tag{3.24}$$

$$G''(\phi, \omega) = G''(0, \omega)(1 + 2\phi + 3.3\phi^2) \tag{3.25}$$

A similar relation between relative dynamic viscosity and reduced volume fraction (ϕ/ϕ_m) was given by Chong *et al* [34] and Polinski [153] and is shown in Equation: 3.26

$$\eta_r = (1 - \frac{\phi}{\phi_m})^{-2} \tag{3.26}$$

From the frequency sweep for different values of ϕ of $Mg(OH)_2$ in Poly(ethylene-co-octene) composites, it is observed that as ϕ increases the value of G' also increases. At low frequency, G' shows a plateau at volume fraction, ϕ ¿ 0.126. The plateau suggests a percolated network structure [70, 118]. The composites with $\phi \geq 0.126$ present solid-gel like response with G' independent of frequency. At low frequency, particle-particle interaction governs the dynamic response of the composites; however, at a higher frequency, particle-polymer interaction takes over [118].

3.7.4 Flow rheology

Concentrated filled polymer melts exhibit shear-thinning behavior [15], [12], [172], [154], [74], [153]. Figure: 3.19 illustrates the flow curve for glass spheres suspended in a thermoplastic polymer at 150^{deg}C at different filler concentration. It is seen that the Newtonian plateau becomes shorter with increasing ϕ. Shear-thinning is exhibited for all concentration [153]. The shear thinning index calculated from the power-law equation is ~ 0.4.

3.7.5 Structure and rheology of worm-like micelles

Worm-like micelles are elongated and semiflexible aggregates resulting from the self-assembly of surfactant molecules in aqueous solutions. When micelles grow and become worm-like, the aggregates are much like polymers, and as polymers, they entangle above a critical concentration. The aqueous solutions then become viscoelastic. There has been considerable research on the viscoelasticity of worm-like micelles [29, 68, 170, 178, 195, 199, 203]. Worm-like micelles are also considered as models for polymers because of their similar non-linear viscoelastic properties.

When submitted to steady shear, these viscoelastic fluids undergo a shear banding

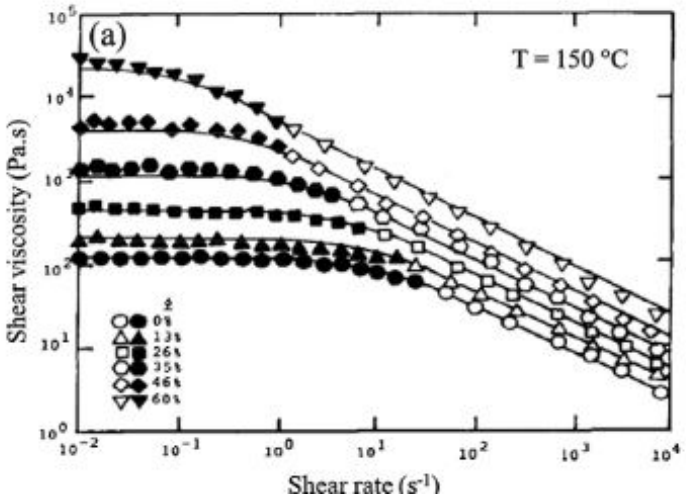

Figure 3.19 *Variation of steady shear viscosity with shear-rate for filled-glass-spheres at different ϕ in thermoplastic polymer. Solid and open symbols represent data set obtained by cone-plate geometry and capillary rheometer, respectively (Taken from [153])*

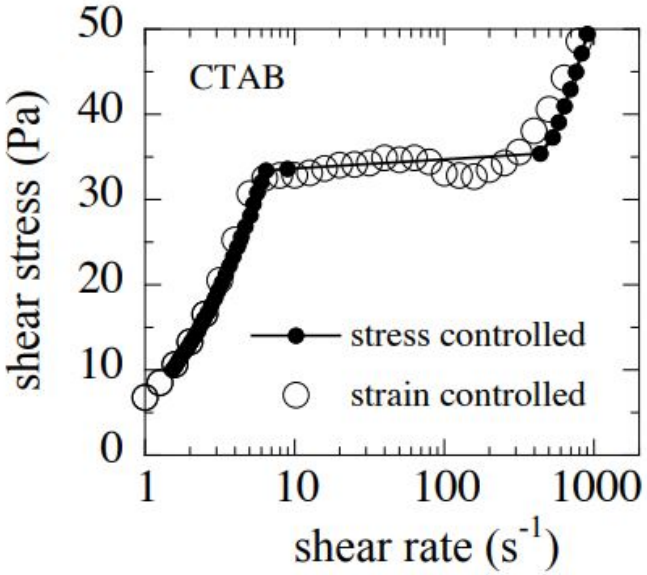

Figure 3.20 *Comparison between the steady state shear stress results obtained from controlled strain and controlled stress rheometry for CTAB-D2O wormlike micelles at c = 0.18 wt. [30]*

transition as represented in the Figure: 3.20, which is associated with a plateau in the stress versus shear rate curve [86]. The shear banding transition is a transition between a homogeneous and a non-homogeneous state of flow, the latter being characterized by a demixing of the fluid into macroscopic regions of high and low shear rates. The flow curve of the for CTAB-D2O wormlike micelles at $\phi = 0.18$ by weight at T = 32°C [30]. In the lower branch, the stress increases linearly up to at the critical value γ, followed by a stress plateau that stretches over more than a decade in shear rates. At high shear rates, there is a further increase in stress.

3.8 The rheology of liquid crystals

In this section, the rheology of unfilled lamellar and nematic liquid crystal followed by the filled liquid crystal composites will be discussed.

3.8.1 Lamellar liquid crystals

The coupling between shear flow and the internal structure in a lyotropic lamellar phase, is both of practical and fundamental interest. Shear flow deformation is known to induce many structural changes in the mesoscopic order. Firstly, a change in orientation of the layers [46, 205] and secondly shear induced formation of multi lamellar vesicles (MLV) [103, 137, 145]. There are some excellent reviews by Duke and Chapoy [51] on the rheology of lamellar phases, by Bohlin and Fontell [23, 99] for small oscillatory shear experiments on lamellar mesophases. The rheology of the lamellar mesophase formed by hen-egg lecithin and water was studied by Bourgoin and Shankland [41]. Hirsch *et al.* [72] studied the flow properties of a lamellar mesophase formed in a quaternary anionic surfactant/alcohol/hydrocarbon/water or brine system. They reported shear thinning behavior in quaternary lamellar mesophase. The transient viscous flow of the lamellar mesophase was analyzed by Gallegos *et al.* and Franco *et al.* They ascribed the stress decay with shear time not only to the orientation of liquid crystalline domains but also to their breakdown in smaller ones. McKay *et al.* [123] reported linear viscoelasticity results obtained by small-amplitude oscillatory shear for the lamellar mesophase formed by a double tail anionic amphiphilic lipid at a composition located on the border with a dispersion region.

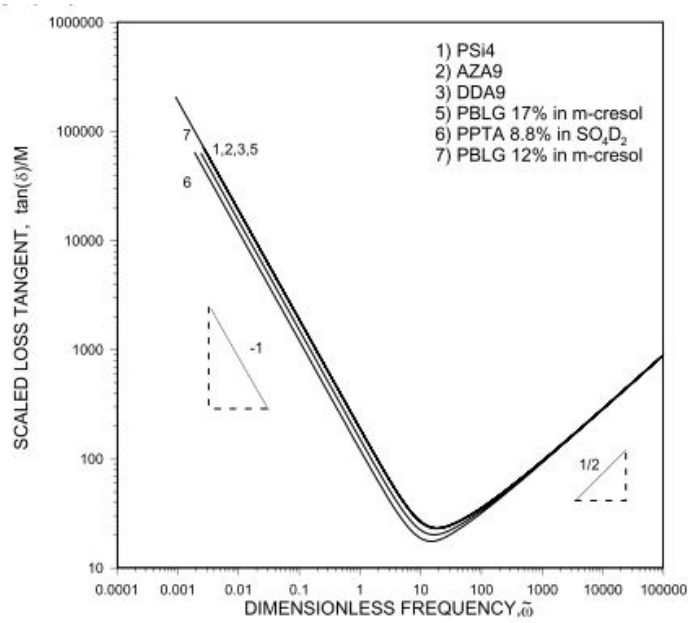

Figure 3.21 *Scaled loss tangent (tanδ/M) as a function of the dimensionless frequency (ω) for different NLC polymer. [108]*

He only described the behavior of G' as a function of frequency. His work was then carried forward by Robles Vazques [129], who characterized the entire viscoelastic spectrum of the lamellar phase. Oswald *et al.* [142] studied the rheology of a lyotropic lamellar phase, where they showed under shear the flow of how the dislocation loops cross and connect the layers and disturb the flow. Awad *et al.* have investigated the structure and rheology of an aqueous/fatty alcohol and anionic surfactant mixture. The resulting gel system was suggested to serve as a model system in the formulation industry. In the gel phase, the defect mobility is strongly reduced resulting in a high zero shear viscosity however the value of yield stress was not identified. The elastic modulus, measured from small linear deformations, decreased with increasing SDS content, suggested that SDS acts as a plasticizer. With increasing SDS, the increased disorder in the chain packing results in a softening of the bilayers and a decrease in the elastic modulus [11]. The rheology of colloidal particle in lyotropic hexagonal LCs were studied by Kulkarni and group [177]. They demonstrated that the rheology and the microstructure of colloidal particle in hexagonal composites depends on particle concentration , ϕ, shape and kinematics of phase transition. The value of the storage moduli, G', increased with the concentration of particles.

3.8.2 Nematic liquid crystals

Using the Leslie-Ericksen theory, Burghardt described the linear viscoelastic response of a nematic monodomain under small amplitude oscillatory flow for homeotropic anchoring at the substrates. One of the key characteristics of nematic LCs is the strong dependence of their viscoelasticity on the orientation of the director which is reflected in the anisotropy of the Meisowicz viscosities. The Ericksen number describes the competition between flow-induced and boundary-induced orientation within a nematic monodomain and is given by $E_r = \frac{\eta\dot{\gamma}L^2}{K}$, where K is the Frank elastic constant of the 5CB NLC, L is the relevant length sale, $\dot{\gamma}$ is the strain rate and η is generalised viscosity. Reorientation of the director can occur when $E_r > 1$. In both the low and high frequency limits, the response is entirely viscous since the director rotates in phase with the shear rate at low frequencies and rotates in phase with the applied shear strain at high frequencies. At intermediate frequencies the response becomes viscoelastic because the Frank elasticity resists distortion of the director [27]. Lima and Rey generalised the Leslie-Ericksen director-flow model using different superposition schemes for low and high frequencies, validating their approach against experimental data sets for a range of material parameters (including thermotropic and lyotropic LCs and flow-aligning and geometries including capillary, Poiseuille and simple shear flow and for bend, twist and splay distortion modes. It was observed for nematic monodomains the viscous response always dominates the elastic response [42]. Rey *et al.* provided a universal theoretical description of the dynamic rheological response of all nematic liquid crystals, valid for a broad range that included flow-aligning and tumbling, polymeric and lyotropic nematic materials [108]. Superposition through appropriate scaling of the moduli revealed identical viscoelastic response behaviour for which the loss modulus G'' is greater than the storage modulus G' at all frequencies and the ratio $\tan\delta = G''/G' \sim \omega^{-1}$ at low frequencies before increasing with $\tan\delta \sim \omega^{1/2}$ above a resonance frequency $\omega_r = 18.65$, a value that is independent of materials parameters, see Figure: 5.2. In 1990, Burghardt warned that 'in the presence of monodomains, the estimated time scale for director relaxation becomes short enough that distortional elastic effects may contribute significantly to the macroscopically observed viscoelastic response' [27].

Influence of filler

Nematic colloids form gels due to the dynamic arrest of the motion of colloids in the LCs matrix, such as jamming and percolation [188]. There have been several reports on the formation of gels by dispersing colloids in nematic LCs [4, 124, 200]. These gel possess mechanical properties associated with the long-range ordering and the elasticity of the LCs phase. These properties make them of interest in several applications. The making, mixing, and transfer of such materials generally require knowledge of the possible variation of viscosity with shearing rates as well as with concentration and particle size distribution. So, it is essential to understand the behavior of viscosity as a function of shear rate. However, despite the importance of the problem, few experimental data exist for the effects of solids concentration and particle size distribution on the rheological properties of concentrated suspensions in nematic LCs. Zapotocky *et al.* investigated the effect of about 1 μm silica particles in cholesteric LCs [159]. From the rheological studies, they showed the effect of the network of disclinations connecting the bigger clusters of particles. Meeker *et al.* have found an unusual soft–solid-state in 5CB (pentyl cyanobiphenyl) LC colloids prepared by dispersing PMMA (polymethylmethacrylate) nanoparticles (250 nm) [124]. Nanoparticles were mixed into the isotropic and then cooled, and the interface drives the clustering of colloids, thus forming solid cellular structures. Petrov *et al.* showed that solid cellular structures are formed in these systems, and the morphology of these cellular networks was studied by Anderson [8]. Poon and coworkers [124] dispersed PMMA-PHSA particles in 5CB LCs and demonstrated that slow cooling of the dispersion led to nucleation and growth of nematic domains and expulsion of the colloids ahead of the growing phase boundary. The growth of the nematic domains was arrested upon jamming of colloids between the domains.

Wood *et al.* conducted a study on concentrated filled thermotropic nematic composite [200]. They dispersed micron-sized PMMA-PHSA particles in nematic 5CB for a range of volume fractions, $0.005 \leq \phi \leq 0.5$, and performed oscillatory rheology. Figure: 3.22 shows the dependence of storage modulus on the volume fraction of the composites. It can be observed that beyond $\phi > 0.18$ there is a rapid increase in the value of G' consistent with the function; $G' \sim \phi^2$. They showed that it was due to the formation of a percolating network structure of disclination lines in the nematic structure. These lines are entangled with the particles giving a self-quenched defect glass state of line defects at $\phi >$

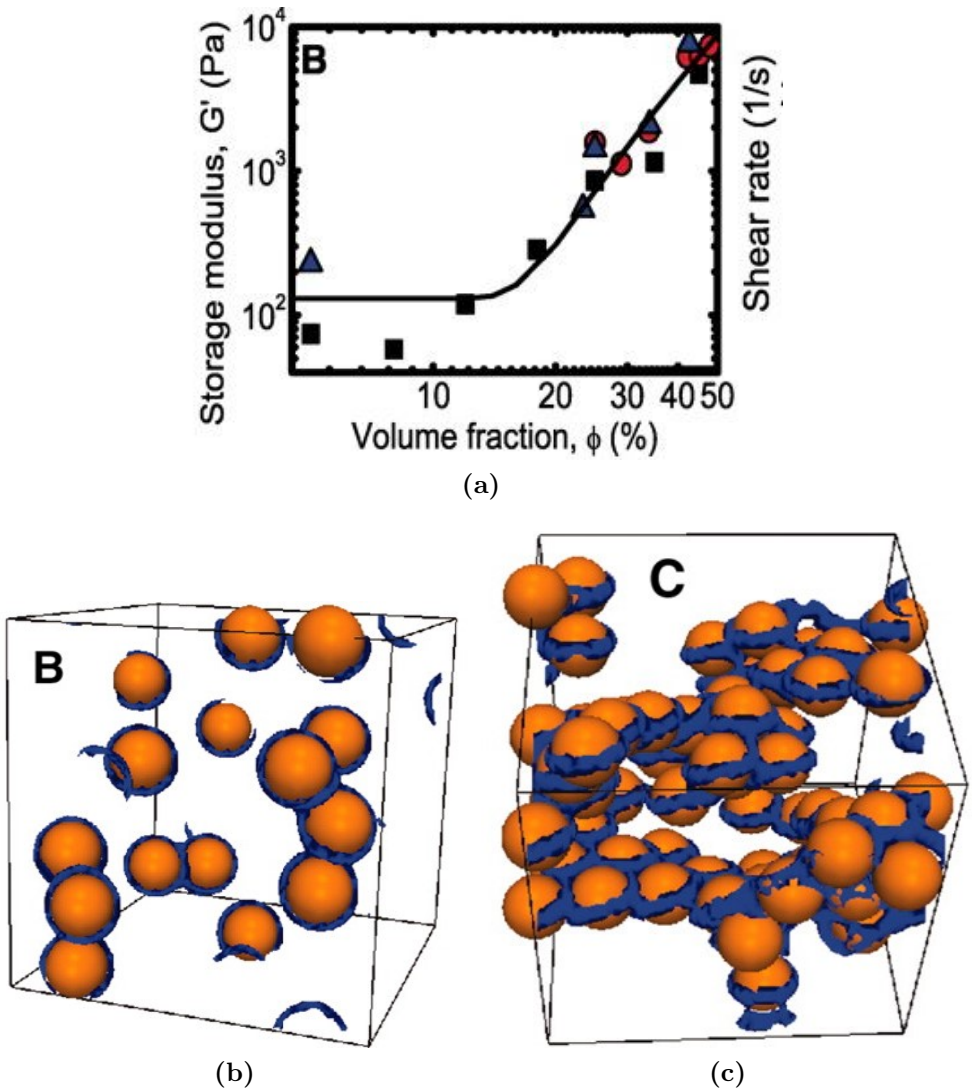

Figure 3.22 *(a) The value of maximum G' for filled nematic compoistes as a function of volume fraction, Simulation showing (b) isolated Saturn-ring defects at dilute ($\phi < 0.2$) concentration as compared to (c) entangled Saturn-ring defects for concentrated composites, $\phi \geq 0.2$.[200].*

0.2. A simulation in the dilute and concentrated regime (see Figure: 3.22 b and c) confirms the entanglement theory in accrodance with the prediction by Araki *et al.*. In the dilute concentrattion, the Saturn-ring defects remain isolated without interacting among them, however with concentration these ring defects come in close proximity with each other and entangle to form percolating network structure of defects. The microstructure is different from those formed by dispersing particles in istropic phase and cooling them into nematic phase [124]. Thus, providing certainity that topological defects play a crucial role in the bulk rheology of the composites.

A third pathway for the formation of the nematic colloidal gel was proposed by Bukusoglu, Abbott, and co-workers [26]. They reported the formation of a nematic colloidal gel by spinodal decomposition of colloids in an isotropic phase followed by nucleation of the nematic domain. On the cooling of dispersion, the onset nematic domain occurs. These nematic phases were observed to nucleate and grow within the pre-existing cellular microstructure formed during the quenching of isotropic to nematic phase. The nematic domain growth almost ceases when the nematic phase had filled each cell of the microstructure, thus forming a gel. This is in contrast to the previously described mechanism of formation of a CLC gel in which the microstructure of the gel formed during the isotropic-to-nematic transition.

Chapter 4

Materials and methods

Surfactant allow us to protect water surface and to generate these beautiful soap bubbles, which are delight for our children.

- Pierre-Gilles de Gennes

In this chapter, we focus on the specific colloidal particles and liquid crystal system studied in this thesis. Details on the characterization of colloids are presented, followed by the rheological protocol used for characterizing the colloid and liquid crystal composites. This chapter is divided into two sections, (a) Materials and (b) Methods.

4.1 Materials

The *filler* particles used in this thesis were selected based on their shape, size, density, charge, and compatibility with the solvent.

4.1.1 Solid spheres

A solid sphere colloidal dispersion is an assembly of impenetrable spherical particles that cannot overlap each other when suspended in a continuous medium - fluid [14]. They do not change their shape or spatial configuration when dispersed in the fluid. Four types of micron sized solid spheres colloids were

Table 4.1 *Physical properties of colloids used in this research.*

Colloids	Grafted Polymer	Refractive index	ρ (g/cm^3) at 25°C
PMMA	PHSA	1.500	1.188
PMMA	PVP (MW:360,000)	1.500	1.188
Ani PS	negative charge	1.580	1.040
Cat PS	positive charge	1.580	1.040

studied in this thesis. These are (a) poly-methyl-methacrylate (PMMA) spheres sterically stabilized by grafting a layer of short polymer chain onto their surface [65], (b) PMMA particles stabilized by PVP [147], (c) Anionic Polystyrene (Ani PS) spheres stabilized by the negative charge and (d) Cationic polystyrene (Cat PS) spheres stabilized by the positive charge. Table: 4.1 lists the physical characteristics of these particles. A schematic of charged and uncharged colloids is represented in the Figure: 4.1.

1. **PMMA-PHSA particles**

   Polymethylmethacrylate (PMMA) microspheres are often referred to as acrylic microspheres. PMMA polymer is an amorphous, transparent, and colorless thermoplastic that is hard and stiff. We have used two different solubility PMMA particles, (a) oil-based and (b) water-based. The choice of solvent plays an important role in determining the inter-particle interaction between colloids.

   Oil-based PMMA spheres were stabilized by covalently-grafted poly(12-hydroxystearic acid) (PHSA), which was synthesized in house by Andrew Schofield following the procedure of Antl *et al.* [73]. The covalently grafted PHSA chains provide repulsive steric stabilization and have a thickness of 10 nm [64]. The PMMA-PHSA particles were initially dispersed in a density matching solvent - decalin. To obtain dry particles, the decalin suspension was centrifuged and washed with hexane several times. After several trials, it was found that eight washes were sufficient to wash away all the solvents from the particles. The particles were then dried in a vacuum oven for 65°C for two days. To check the monodispersity of the particles, we imaged the particles under a Zeiss confocal microscope. Figure: 4.2 shows the confocal micrograph of PMMA particles in decalin which is a refractive index matching solvent ($n_{decalin}$ = 1.48 and n_{PMMA} = 1.50). PMMA particles are less hydrophobic than the charged polystyrene. The density of these beads, 1.188 g/cm^3, is considerably heavier than polystyrene particles,

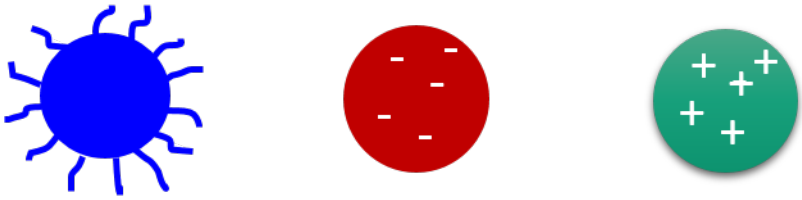

Figure 4.1 *Schematics of (a) PMMA particles sterically stabilised by grafting a layer of short polymer chain onto their surface, (b) Ani PS stabilised by negative charge and (c) Cat PS stabilised by positive charge.*

allowing more rapid separation and making them easier to concentrate by centrifugation. The particles typically have a hydrophilic anionic surface with a refractive index of 1.5 g/cm^3 at 20°C. Particle-size distributions were determined on dilution using a dynamic light scattering (DLS) [128] set-up and the diameter, d , was found to be (1.165 $\pm$ 0.121) μm.

2. **PMMA-PVP particles**

   Water-soluble PMMA particles were sterically stabilized with polyvinylpyrrolidone polymer having a molecular weight of 360,000. These particles were also centrifuged and washed with deionized water eight times before drying them in a vacuum oven at 40 °C for two days before use. The diameter (d) of water-based PMMA-PVP particles was calculated to be (1.250 $\pm$ 0.034) μm.

   The zeta potential (ξ) [164] of both - oil-based and water-based PMMA particles were measured using a Malvern Nano Z series zeta sizer. However, we were not able to get a definite value because the measured value was very low and not consistent as the particles were sterically stabilized. The PMMA particles were dyed with a fluorescent dye, NBD (4 chloro-7 nitrobenz-2 oxa 1,3 diazole), which absorbs radiation at 488 nm and emits fluorescent light at 525 nm.

3. **Anionic and Cationic Polystyrene particles**

   Water-based polystyrene beads stabilized by positive (Cat PS) and negative (Ani PS) charges were used to form charged composites in NC1 LCs. Prior to use, they were centrifuged eight times in water and then dried in a vacuum oven at 40°C for two days. The dried powder was dispersed in NC1 to form composites. The zeta potential of the charged polystyrene beads was measured and the surface charge was calculated by Gouy-Chapman model [136]. Table: 4.2 summarises the size, zeta potential (ξ) and surface charge (q) of the colloidal particles.

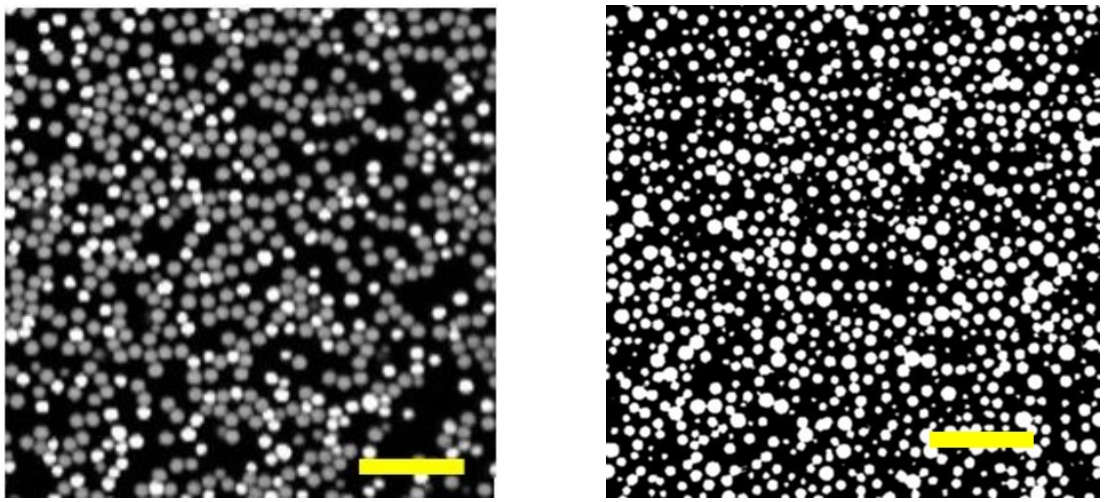

(a) (b)

Figure 4.2 *(a) PMMA particles dispersed in decalin as seen under confocal microscope, (b) Ani PS in water as seen under confocal microscope. The white spheres are particles and black medium is the solvent. Scale bar is 10 μm.*

Table 4.2 *Measured size, zeta potential (ξ) and surface charge (q) of colloids.*

Colloids	Diameter (2r) μm	ξ mV	σ ($\mu C/m^2$)
PMMA - PHSA	1.165 ± 0.121	0.112±0.091	-
PMMA- PVP	1.251± 0.178	-	0.087±0.079
Ani PS	1.389 ± 0.113	-54.63 ± 2.84	-29.42 ± 1.51
Cat PS	0.915 ± 0.045	+44.18 ± 3.68	+24.13 ± 2.14

4.1.2 Deformable colloids - PDMS- Polydimethyl Siloxane

The deformable colloids here refer to the colloids which can change their shape within the dispersing medium e.g., emulsion droplets. To make emulsions in the nematic solvent, we used PDMS - Polydimethylsiloxane. Two different kinematic viscosity (0.05 and 0.5) Pa.s PDMS (polydimethylsiloxane) materials were purchased from Sigma Aldrich and were used without any further purification. The emulsification process for making nematic emulsions will be covered in the sample preparation section.

Table 4.3 *Thermodynamic property of 5CB LCs.*

M (g/mol)	ρ (g/cm^3)	$T_{XN}\circ$ C	$T_{NI}\circ$ C
249.358	1.0024	24	35

4.1.3 Liquid crystals (LCs)

Out of the wealth of the liquid crystalline mesophases, we chose one of the well studied and characterised thermotropic nematic LCs, 4-cyano-4-pentyl-1,1-biphenyl (C18H19N) - 5CB. For the lyotropic system, we chose a ternary mixture surfactant, co-surfactant, and water liquid crystalline system. Nematic and lamellar lyomesophases are studied in this thesis.

1. **Thermotropic nematic liquid crystals - 5CB.**

   The thermotropic liquid crystal used in this thesis is 5CB. 5CB is the single component thermotropic nematic liquid crystal called 4-cyano-4-pentyl-1,1-biphenyl ($C_{18}H_{19}N$). It was purchased from Kingston Chemicals (UK) and used without any further purification. The molecular structure of 5CB (Figure: 4.3) consists of two consecutively bonded phenyl rings attached to a cyano group (CN) on one end and a five-carbon alkyl chain (pentyl, C_5H_{11}) on the other end. While the former renders the molecule strongly polar, the latter contributes to making it highly anisotropic in shape. The attachment of the nitrile and pentyl groups at the farthest relative separation results in the molecular length (around 2 nm) being much longer compared to its transverse dimension, which is 0.4 nm, leading to an evident shape anisotropy with an aspect ratio greater than 3:1. In the literature, 5CB has been characterized thoroughly and exhibits only the nematic phase at room temperature. It remains nematic between (22.4 to 34.5)°C and transitions to isotropic phase at transition temperature, $T_{NI} = 34.5$°C. All the rheology experiments were conducted at T = 25±1°C to maintain the sample in its liquid crystalline phase. The thermodynamic properties of 5CB nematic LCs are summarised in Table: 4.3. Table: 4.4 enlists the splay (K_{11}) , twist (K_{22}) and bend (K_{33}) elastic constants and different Miesowicz viscosity coefficients of 5CB at T = 25°C [83, 132, 160].

2. **Lyotropic liquid crystals.**

   The lyotropic mesophases chosen were composed of a ternary mixture of sodium dodecyl sulfate (SDS), an anionic surfactant, 1-decanol, and water.

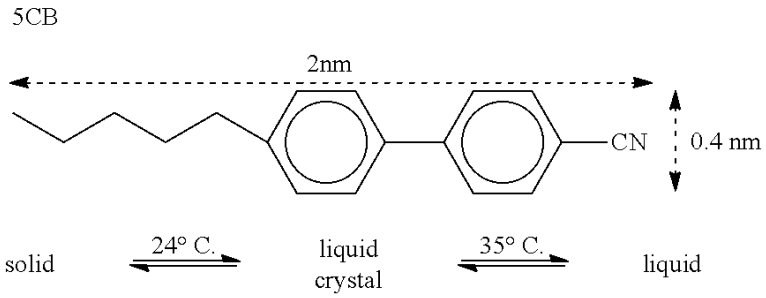

Figure 4.3 *5CB moleculal structure - two consecutive phenyl rings attached to a cyano group.*

Table 4.4 *Elastic constant and viscosity coefficient of 5CB in nematic phase at T= 25° C.*

K_{11} (pN)	K_{22} (pN)	K_{33} (pN)	η_1 mPa.s	η_2 mPa.s	η_3 mPa.s
6.4	3.2	9	22	123	43

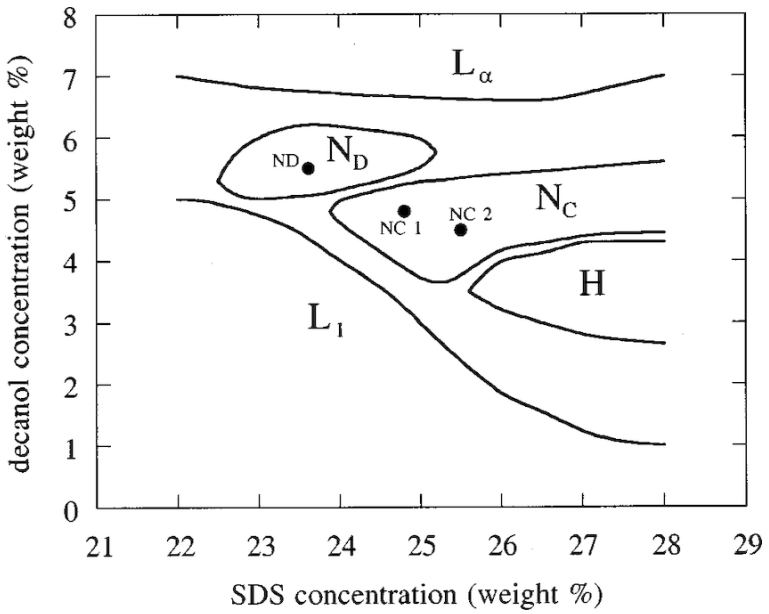

Figure 4.4 *Partial phase diagram of lyotropic liquid crystals showing different mesophases as a functon of relative SDS and Decanol concentration. The phases of interest are NC1 (nematic calamitic) and L_α (Lamellar) phases.*

Table 4.5 *Amount of SDS-Decanol and water in wt%.*

Phase	SDS	Decanol	Water
NC1	24.8	4.8	70.4
L_α	25	8	67
Iso	23	2	75

One of the reasons for choosing this lyotropic liquid crystalline system because its phase-diagram has been thoroughly studied and is very cost-effective to make in bulk. Several reviews by independent authors have established its phase diagram independently, and readers are directed to [5–7, 81, 150] for detailed calculation. This ternary mixture exhibits a succession of different lyotropic liquid-crystalline phases. The type of liquid-crystalline structure formed depends on the curvature adopted by the interface between the aggregates and the surrounding solvent. Lamellar, hexagonal, nematic calamitic (NC1), nematic discotic (ND), and cubic phases are usually seen in these systems. The anisotropic liquid crystalline phases appear when the concentration of amphiphilic molecules is increased to a value larger than the critical micellar concentration (CMC). For example, in the case of the SDS/pure water mixture, CMC = 0.008 M, and liquid crystalline phases are present for SDS at a concentration of > 0.2 M [7] which is two orders of magnitude higher. The theory of micelle formation has predicted the shape of the micelles. They could change from spherical to ellipsoidal at a specified concentration of the amphiphile. A partial phase diagram of this lyotropic system is depicted in the Figure: 4.4. Our focus is to characterize nematic lyomesophase of type NC1 (nematic calamitic 1), which forms cylindrical micelles with an aspect ratio of $>$ 3:1. The largest micelles size in the nematic phase is of order of nanometer [57]. The lamellar phase (L_α) form alternating layers of water and surfactant forming bilayers structure. And these phases are observed in the presence of a high concentration of amphiphilic molecules when the interface tends to be planar having large shape anisotropy [6]. Table: 4.5 shows the concentration of SDS, 1-Decanol, and water in weight% to form different lyotropic liquid crystalline phases.

A special precaution should be taken when preparing lyotropic liquid crystal because the lyomesophase is very sensitive to the relative concentration of amphiphilic molecules, a precision of at least 0.02 wt% is recommended. SDS $\geq$ 99% and 1-decanol 98% were purchased from Sigma Aldrich (U.K.)

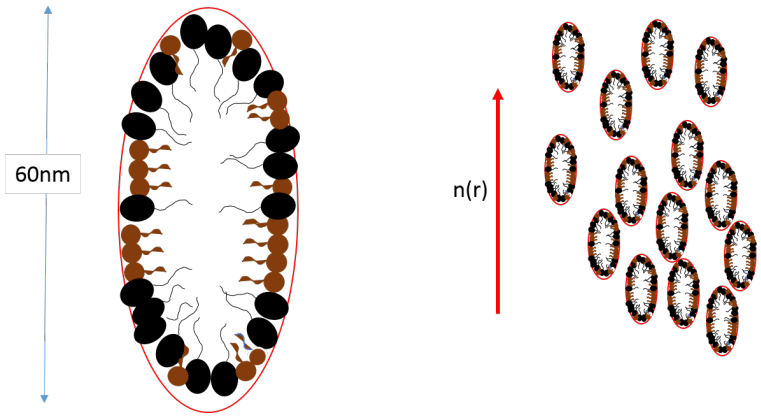

Figure 4.5 *(a) Proposed sketch of prolate ellipsoid or cylinder-shaped with two surfactant molecule - SDS (black) and Decanol (brown), (b) Sketch of the micellar order in NC1 phase.*

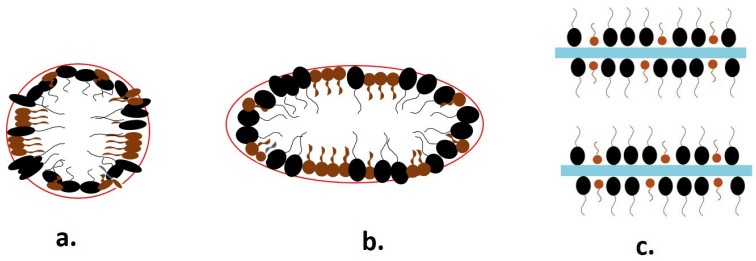

Figure 4.6 *Predicted micelles shape and structure (a) spherical micelles present in the isotropic phase, (b) as the concentration of decanol increases the micelles become cylindrical like in the nematic calamitic (NC1) phase, (c) continuous bilayers are observed in lamellar (L_α) phase.*

Table 4.6 *Thermodynamic property of NC1 LCs [21].*

LCs	ρ (g/ml)	$T_{XN}\deg C$	$T_{NI}\deg C$
NC1	1.0315	23	32
L_α		22.3	35

and were used without any further purification. To prepare NC1 LCs, 24.8 ± 0.2% of SDS and 70.40 ± 0.19% deionized water in weight% were thoroughly mixed using a vortex mixer for 120 seconds. Then, 4.80± 0.04 % in weight %of 1-Decanol was added to the mixture and was thoroughly mixed. The addition of fatty alcohol (1-decanol) gets rid of some amount of bubbles formed from mixing SDS and water. NC1 phase remains nematic from 23 to 32°C and the transition temperature of L_α is from 22.3 to 35°C. The mixture is then sonicated for 10 minutes to remove any remaining bubbles. When the mixture looks thoroughly homogeneous, it is left to sit on the shelf for 24 hours before using them for any experiment. Sample vials were sealed with paraffin to avoid any mass loss of constituents.

For preparing the lamellar phase, L_α, the same protocol was followed by changing the relative concentration of SDS to 25± 1 %, 1-decanol to 8 ± 0.8% and rest 67 ± 0.4 % to water. In the lamellar phase, amphiphilic molecules are organized as supermolecular aggregates, forming layers with a large shape anisotropy. The surfactant molecules form a bi-layer structure separated by solvent layer. The thermodynamic properties of micellar LCs are summarised in table: 4.6. Figure: 4.6 shows an illustration of the expected micelles shape and structure (a) spherical micelles present in the isotropic phase, (b) as the concentration of decanol increases the micelles become cylindrical as present in the nematic calamitic (NC1) phase, (c) continuous bi-layer structure is observed in the lamellar phase. Like all the anisotropic phases, lyotropic nematic and lamellar liquid crystal exhibit distinct optical texture when confined between two parallel glass slides and observed under cross-polarisers. Figures: 4.7 and 4.8 show the defect structures observed in both phases. Schlieren texture is observed for NC1, whereas streaky texture is observed in the lamellar phase.

Table 4.7 *Elastic constant [13, 96] and viscosity coefficient of NC1 in nematic phase at T= 25° C.*

K_{11}(pN)	K_{22} (pN)	K_{33} (pN)	η_1 mPa.s	η_2 mPa.s	η_3 mPa.s
2.1± 0.1	3.2	2 ± 1	N/A	N/A	N/A

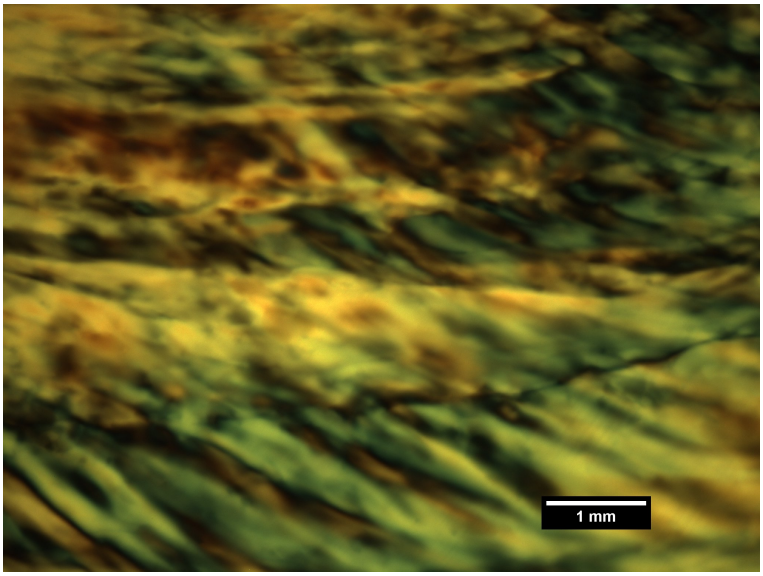

Figure 4.7 *Schlieren texture observed in NC1 phase of lyotropic liquid crystalline system composed of SDS-Decanol and water.*

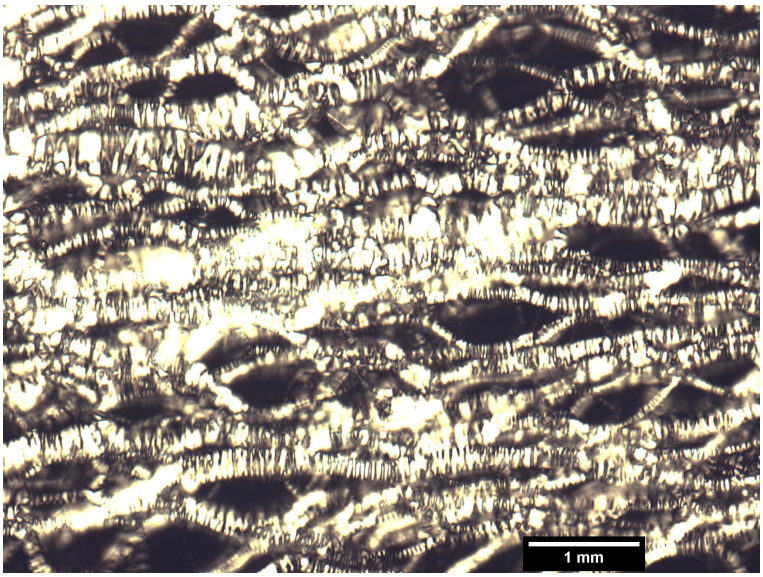

Figure 4.8 *Streak like defect lines observed in L_α phase of lyotropic liquid crystalline system made up of SDS-Decanol and water.*

4.2 Methods

4.2.1 Sample preparation

Solid-sphere nematic composites

A class of soft-solid is formed when spherical colloids of concentrations ($\phi > 0.18$) are dispersed in the nematic liquid crystal [200]. In this thesis, we study the soft solid composites formed by dispersing hard-sphere colloids in both thermotropic and lyotropic nematic liquid crystal. To make PMMA-PHSA composite in 5CB, thoroughly dried PMMA-PHSA particles with desired concentration were added to 5CB. The mixture was sonicated at room temperature for 10 minutes to get a homogenous mixture. Prior to performing any experiment, the samples were manually stirred with the spatula.

The relative concentration of colloidal particles in the liquid crystal was quantified using volume fraction. The volume fraction, ϕ, % was calculated using:

$$\phi\% = \frac{v_p * 100}{V_T} \tag{4.1}$$

where v_p is the volume of colloidal particles and $V_T = v_{LCs} + v_p$ is the total volme of the composites. The mass of the particles to be added were calculated by multiplying the $v_{particles}$ with their density, for 5CB density used was 1.0024 g/ml and for NC1 and L_α LCs the value of 1.0351g/ml [21]. $V_{LCs} = v_{total} - v_{particles}$ and the mass of LCs added is V_{LCs} multiplied by its density. Concentrations of fillers are preferably measured by volume than by weight due to the wide variations in the densities of available colloids. The weight percentage is preferable when volume fraction is difficult to measure.

Composites in lyotropic nematic phases were prepared using a slightly different method. At first, dried PMMA-PVP particles were dispersed in deionized water using a vortex mixer. Then the desired amount of SDS and Decanol were added to the mixture and manually mixed using a spatula. The composites formed were sonicated for 5-10 minutes to get rid of any bubbles present. Sample vials were sealed using paraffin to avoid any loss of constituents masses. The same protocol

was followed to prepare composites of Ani PS in NC1 and Cat PS in NC1. A wide range of volume fraction of the sample was made from $0.05 \leq \phi \leq 0.5$. Figure: 4.9, 4.10, 4.11 shows the images of the prepared PMMA-PHSA in 5CB composites, PMMA in NC1 composites and Ani PS in NC1 composites.

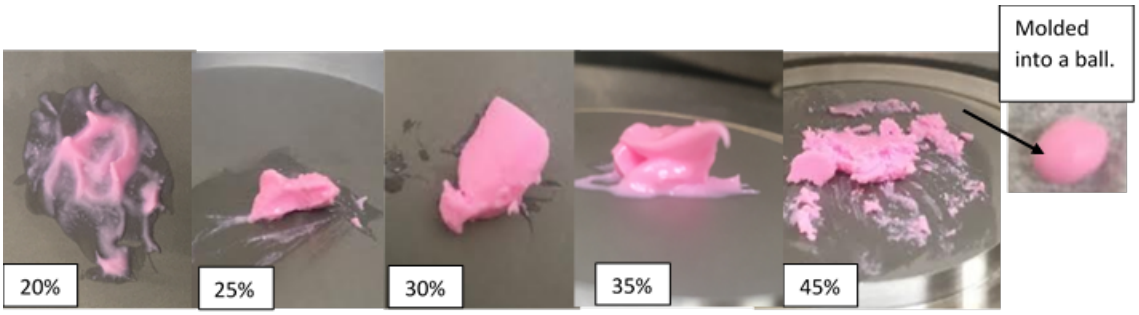

Figure 4.9 *Soft solid composites of different volume fraction ϕ formed by dispersing PMMA-PHSA particles in 5CB liquid crystal.Pink color is due to the dyed PMMA-PHSA particles.*

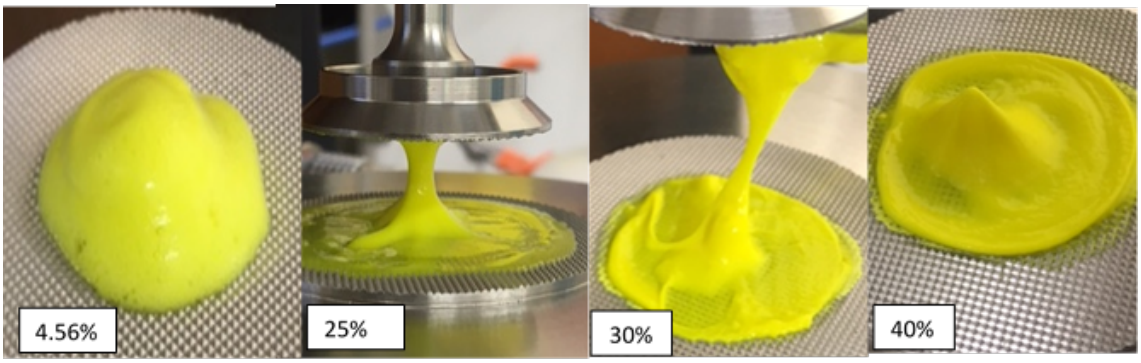

Figure 4.10 *Soft solid composites of different volume fraction ϕ formed by dispersing PMMA particles in NC1 liquid crystal. Pale yellow color is due to NBD dyed PMMA particles.*

- Stability test for the composites.
  A sedimentation experiment over a period of 30 days was conducted to check the stability of the composite against phase-separation.

  1. **Liquid crystal composites**

     A sedimentation profile was recorded for $\phi = 0.2$ of PMMA composites in both 5CB and NC1 nematic liquid crystal as well as lamellar composites. At the beginning of the experiment, all three composites were a homogenous mixture of colloids and LCs. Figure: 4.12 depicts the homogenous sample in the vials at the start of the experiment.

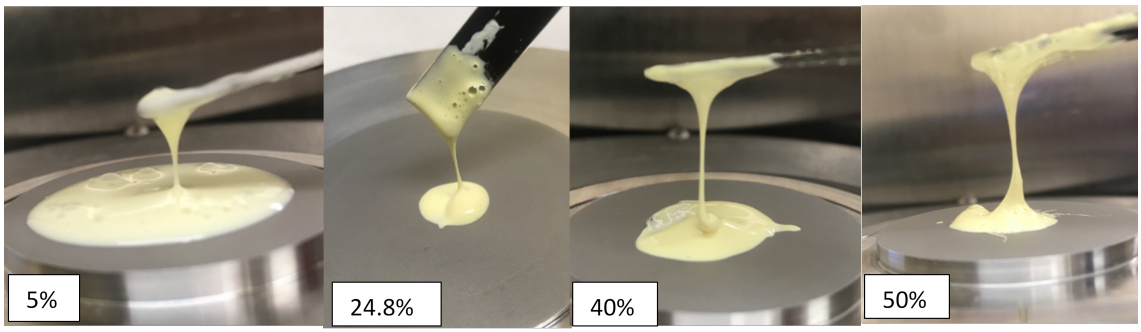

Figure 4.11 *Soft solid composites of different volume fraction ϕ formed by dispersing Ani PS particles in NC1 liquid crystal. Pale yellow color is due to NBD dyed Ani PS particles.*

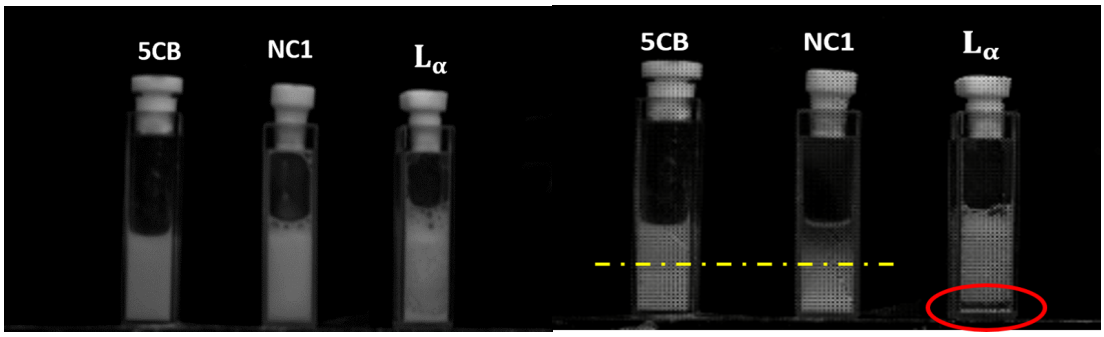

(a) **(b)**

Figure 4.12 *(a) Different LCs composite sample at the beginning of experiment, (b) Unstable composites after 15 days of experiment.*

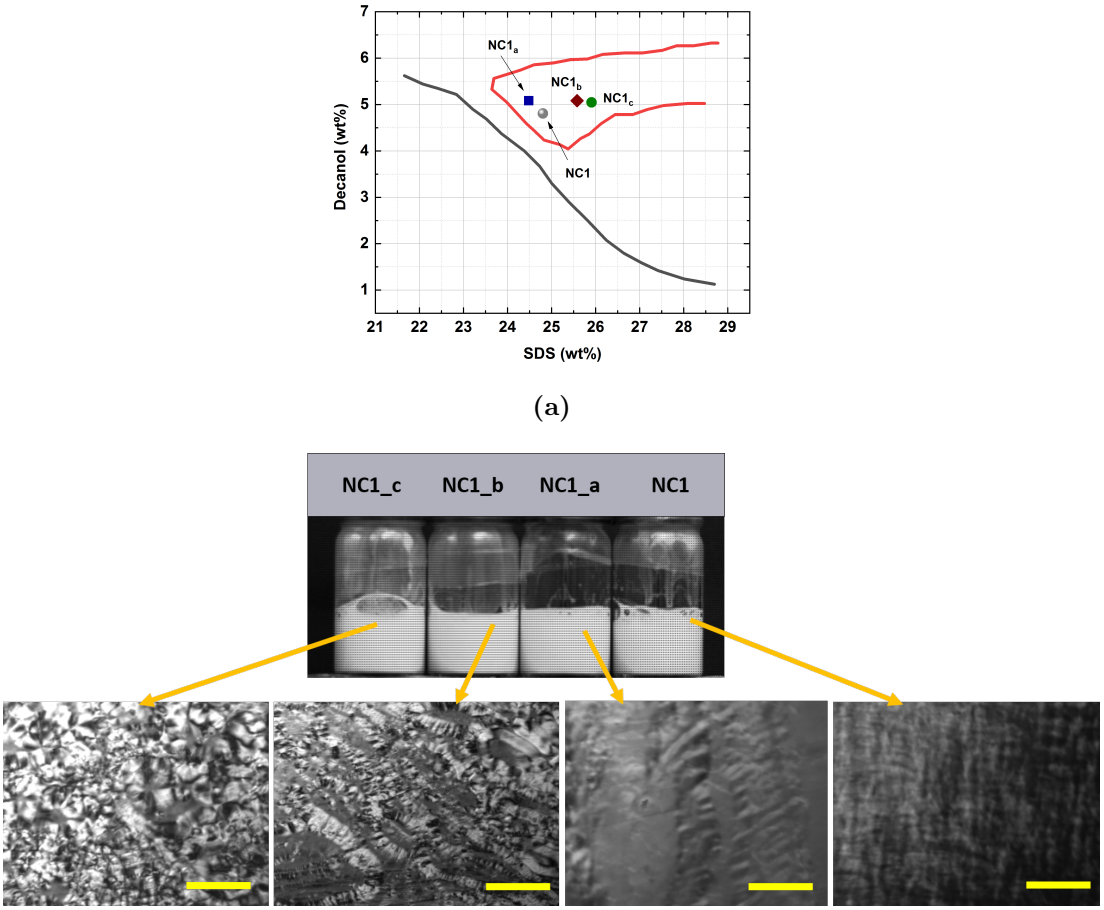

(a)

(b)

Figure 4.13 *(a) Partial phase diagram of lyotropic LCs with points denoting the different deep nematic concentrations studied, (b) Sample vials with the PMMA filled lyotropic nematic at the beginning of experiment, the cross-polariser images of the pure lyonematic phases corresponding to each sample, scale bar is 1 mm.*

The profile was recorded every 10 minutes interval for a total of 30 days. The onset of phase separation starts in lyotropic nematic (NC1) composites after 15 days, with colloids sedimenting at the bottom and pure nematic LCs at the top. However, the thermotropic composites remain stable with no phase separation recorded. However, for the lamellar phase, the composite did not show two clear phase separation, but the instability of the composites was prevalent with the colloid and LCs mixture separating.

2. **Exploring stability of nematic composites.**

   The lyotropic nematic composites were not stable as the thermotropic composites as discussed in the previous section. A selection of four

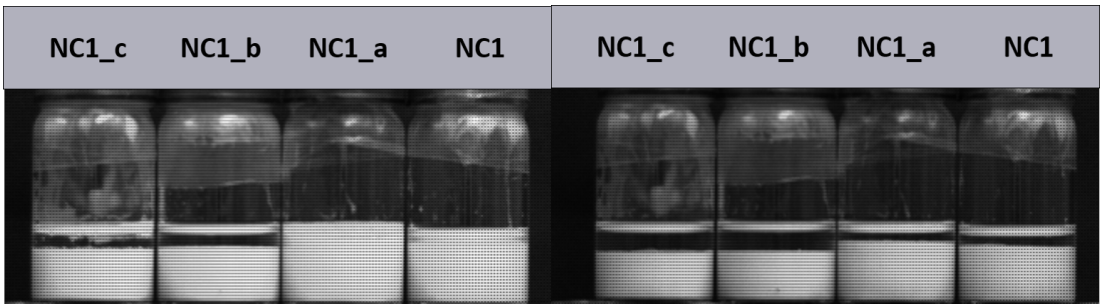

(a) **(b)**

Figure 4.14 *Sample vials with the PMMA filled nematic calamitic composite after (a) 15 days and (b) 30 days.*

different nematic calamitic LCs ($NC1$, $NC1_a$, $NC1_b$, and $NC1_c$) was chosen by varying the concentration of SDS and Decanol around NC1 within the nematic region to test their stability. A partial phase diagram with points denoting different nematic calamitic LCs phases is drawn in figure: 4.13a. The defect structure present in these LCs phases was imaged under cross-polariser, and the resultant texture is presented in figure: 4.13b. From the cross-polariser images, the evidence of multi-phase co-existence is prevalent for $NC1_b$ and $NC1_c$ phases. PMMA particles were dispersed in these nematic LCs at a volume fraction of 30%, and stable homogenous composites were made. These composites were tested for any sedimentation for 30 days. From the sedimentation profile, it was concluded that the $NC1_a$ composite is most stable, followed by a $NC1$ composite. But the onset of phase separation starts earliest in 10 days for $NC1_b$ and $NC1_c$ composites followed by $NC1$ and $NC1_a$ after 15 days. However, all the four samples phase separate in the 30 days. Keeping the instability of our sample in my mind, freshly prepared (within 48 hours) samples were used to perform rheometry and microscopy studies on them. And for the future study, we propose to use a density matching solvent to prolong the stability of these composites.

Nematic emulsion

The nematic emulsions are made by dispersing PDMS (polydimethylsiloxane) droplets in NC1 LCs. The surface anchoring of PDMS droplets stabilised by SDS is similar to that of PMMA microspheres, thus making it possible to investigate

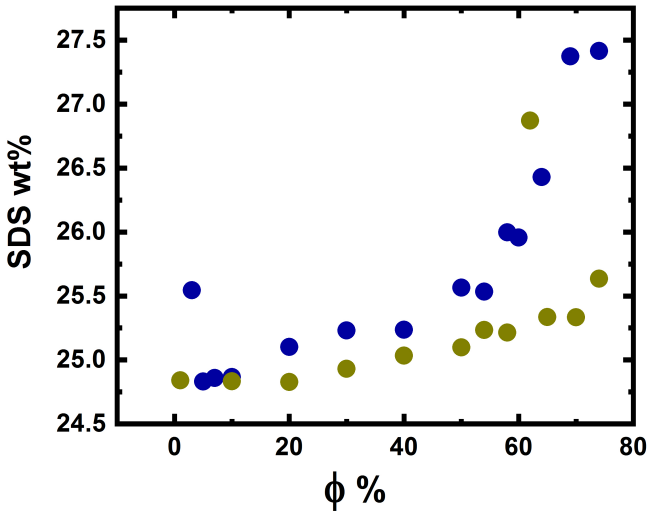

Figure 4.15 *The amount of SDS in wt % added to make nematic (NC1) emulsion and Lamellar (L_α) emulsion for $0.01 \leq \phi \leq 0.74$. Dark blue for nematic emulsion, light green for lamellar. Here we have considered droplet radius (r) 1 μm, surface adsorption of SDS is $3.5E-10 molcm^{-2}$.*

the effect of deformable droplets on the rheology of emulsion. Since emulsions are not at thermodynamic equilibrium, their preparation requires energy to create large interfacial areas. The large interfacial areas is provided by mixing the oil, water and surface mixture using Silverson high shear mixer. The time duration and rate of mixing determine the size and shape of emulsion droplets.

We have prepared four batches of emulsions using 0.05 Pa.s and 0.5 Pa.s of PDMS and at two different shear mixing rate, 3000 rpm and 6000 rpm for 120 s. For preparing different volume fraction of nematic emulsion, the desired amount of water and SDS were added to the vial, and PDMS was added in batches then the mixture was mixed using a shear mixture. Since the NC1 phase has SDS as one of the main constituents, the amount of SDS required to stabilize the interface of the emulsion was calculated separately. It is known that the minimum concentration of SDS required for stabilizing PDMS emulsion is 0.001 M in water [134]; thus, the amount of SDS added to make emulsion was 0.001 M in addition to the amount of SDS required in NC1 phase. When the mixture was completely homogeneously mixed, the required amount of 1-Decanol was added to make the NC1 phase. The figure: 4.15 shows the amount of SDS in weight % added to make nematic (NC1) emulsion and Lamellar (L_α) emulsion for different volume fraction, $0.01 \leq \phi \leq 0.74$. The nematic phase was confirmed by imaging the emulsion under

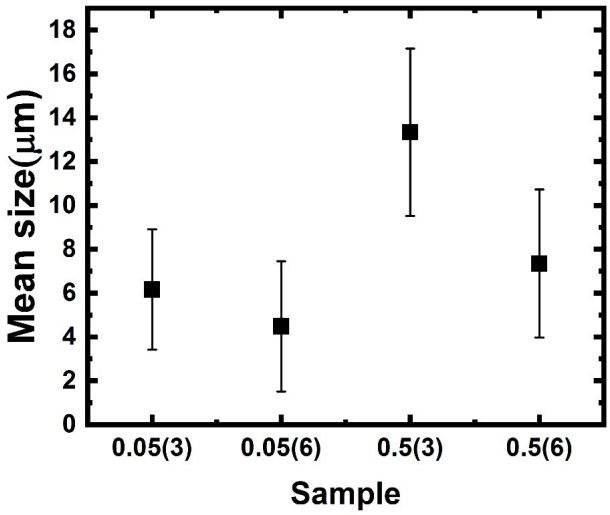

Figure 4.16 *Size comparison of droplet diameter for two different viscosities of PDMS (0.05, 0.5 Pa.s) in NC1 emulsion. 0.05(3) = 0.05 Pa.s PDMS in NC1 emulsion at a shear rate of 3000 rpm, 0.05(6)= 0.05 Pa.s PDMS in NC1 emulsion at a shear rate of 6000 rpm, 0.5(3)= 0.5 Pa.s PDMS in NC1 emulsion at a shear rate of 3000 rpm and 0.5(6) = 0.5 Pa.s PDMS in NC1 emulsion at a shear rate of 6000 rpm.*

crossed polariser. The rate and time of mixing were adjusted to make an emulsion with droplet diameter close to the size of our hard-sphere colloids. Figure: 4.16 shows the size distribution of emulsion droplets for 0.05 Pa.s and 0.5 Pa.s PDMS depending upon the rate of shear mixing. After comparing the droplet sizes from different mixing rates, it was identified that emulsions which were shear mixed at 6000 rpm had droplets diameter of 4.15 $\pm$ 1.89 μm. All the emulsions used in our experiments were thus prepared by following the 6000 rpm protocol. As mentioned in previous chapters, the droplet size influences the volume-to-surface area ratio: the increase of diameter leads to a more pronounced effect of the flow inside the drops.

4.2.2 Rheology protocol

Investigation of the rheology of our composites plays a crucial role in determining their properties and predicting their long-term stability. All the rheology experiments were performed on either a stress-controlled - TA-DHR rheometer and strain-controlled, ARES-G2 rheometer. Schematic diagrams of the working principle of both stresses controlled and strain-controlled rheometer are shown

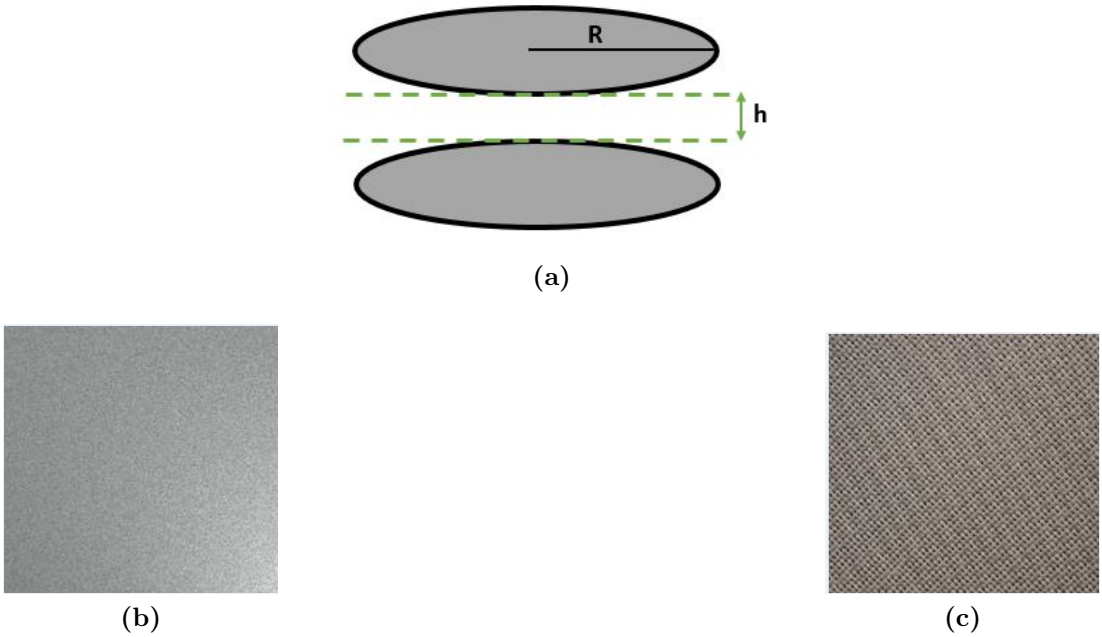

Figure 4.17 *(a) Schematic of the parallel plate geometry used in our experiments, (b) Sand-blasted and (c) Cross-hatched surface texture.*

in the figure: 4.4. The samples were placed on a plate and the other plate, of the parallel-plate geometry was lowered to (see figure: 4.17) a constant gap of 500 $\pm$ 10 μm. There were two different types of plate surface texture used, (a) sandblasted and (b) cross-hatched parallel plate see figure: 4.17 b and c. The rheology results were dependent on plate texture and gap. The temperature of the system was controlled using a constant temperature bath and was kept at T = 25 $\pm$ 1°C. This temperature is well within the range of the nematic region for both 5CB and NC1 liquid-crystalline media. A solvent-trap was used to prevent evaporation from the sample. A pre-shear of 0.1/s was applied for 10s before each experiment.

Oscillatry strain-sweep

In the oscillatory strain sweep, the evolution of storage modulus (G') and loss modulus (G'') was recorded for the applied strain, $\gamma = 0.1$ to 100 % at a constant frequency of 1 Hz. In the low strain regime, we study the rheological behavior of non-perturbed liquid-crystalline and composite structure, while higher values produce results due to structural modification. The low strain region where there are no changes in the magnitude of G' and G'' are referred to as a linear

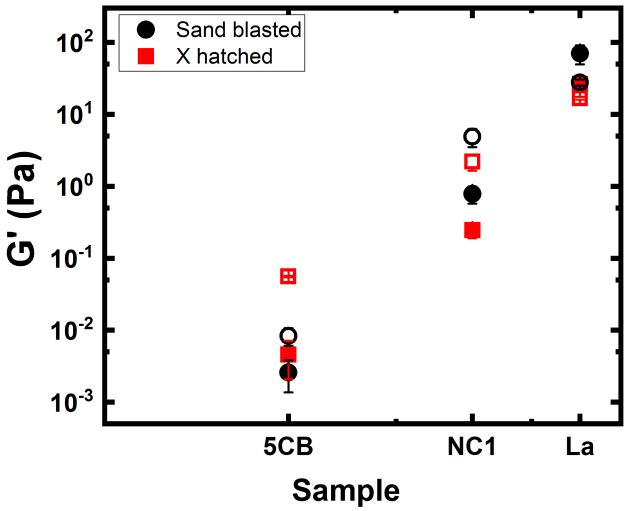

Figure 4.18 *Maximum dynamic moduli values for different LCs at two different surface texture, circle - sand-blasted and square - cross-hatched.*

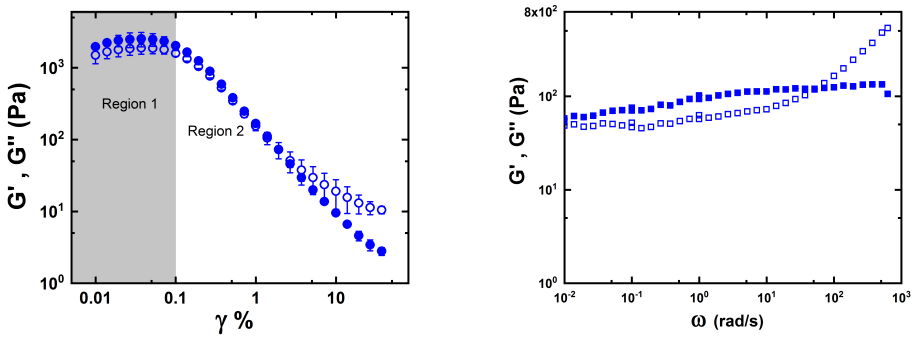

(a) (b)

Figure 4.19 *(a) The evolution of G' and G'' as a function of applied strain γ for PMMA-PHSA in 5CB composites at $\omega = 1$ Hz with G' and G'' showing a plateau up to 0.1% (Region 1) and then starts to yield (Region 2) with yield strain, $\gamma_c = 2.47 \pm 0.79$ %, (b) Frequency sweep curve of PMMA-PHSA 5CB composites at $\gamma = 0.6\%$ with transition from solid to liquid-like' for the range of applied frequency.*

viscoelastic regime (LVR). The value of critical strain (γ_c) was calculated where both G' and G'' divert from their linear behavior and cross over. Reverse strain sweep was carried on the sample to check whether the sample has fractured or are recoverable. Each sample was measured at least three times, and the data plots represent the average of all the runs.

Oscillatory strain sweep using both sand-blasted and cross-hatched surface texture parallel plate is shown in Figure: 4.18. The value of moduli from sand-blasted surface texture is higher as compared to cross-hatched texture. Thus, we have used sand-blasted plate for all our rheology experiments to avoid any discrepancies.

Frequency sweep

The dynamic response of the composites was probed by conducting a frequency sweep. The frequency sweep was recorded for low as well as high, strains to probe the LVR (Region 1) of the sample as well as the yielding region (Region 2). The angular frequency was applied from (0.0001 to 600) rad/s to the PMMA-PHSA in 5CB composites at different strain γ values from 0.01 to 10%. For colloids in NC1 composites, the applied frequency was changed from 0.1 to 600 rad/s. Low-frequency, the sweep was not possible for NC1 composites as they dried during the large experimental runs leading to the discrepancy in the measured value. Figure: 4.6 shows a standard curve of (a) oscillatory strain sweep and (b) frequency sweep for dense colloidal suspension in the nematic liquid crystal.

Steady state flow rheology

Shear viscosity (Pa.s) as a function of the applied shear rate was measured in the steady-state flow experiment. A shear - rate, $\dot{\gamma}$, of the range 0.1 up to 1000/s was applied, and the resultant change in the viscosity and stress values were measured. Figure: 4.20 shows the viscosity curve obtained from steady-state flow measurements for dense composites of PMMA-PHSA particles in 5CB nematic liquid crystalline media.

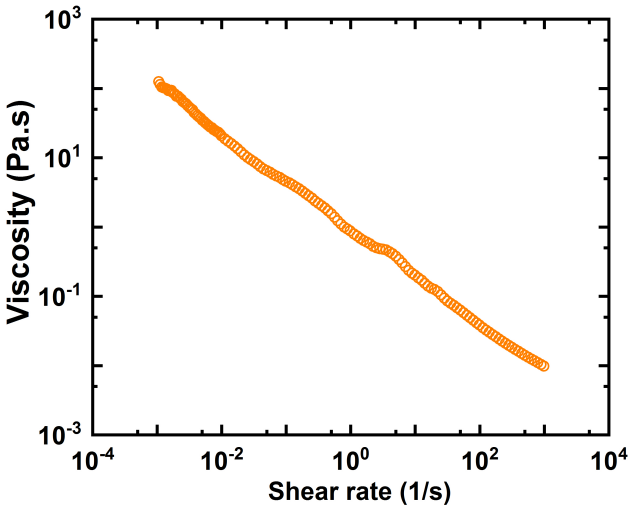

Figure 4.20 *Viscosity decreases as a function of applied shear rate (1/s) showing shear-thinning behavior. The measurements shown are for ϕ = 0.3 PMMA-PHSA in 5CB composites.*

4.2.3 Microscopy

The orientation of the director was resolved using a cross polariser optical microscope, and a three-dimensional microstructure of colloids in liquid crystalline media was studied using a confocal microscope.

Polarising optical microscopy

A Nikon optical microscope was used to image the defect lines in the liquid crystalline phases and to also image the defect around the colloids in dilute nematic composites. A high sensitivity CCD camera was used to record the image of cross polarised light passing through the sample. A polarizer and an analyzer are oriented in a perpendicular directions. When unpolarised visible light is passed through the first polariser; it only allows the light of that polarisation to pass through. When this linearly polarised light hits a birefringent sample such as LCs, it splits into two rays (a) ordinary and (b) extraordinary rays forming elliptically polarised light. The elliptically polarized light passes through the second polarizer, whose axis is perpendicular to the first one, before being recorded by CCD camera. Depending upon the region of interest and the optical resolution desired, a range of different air objectives were used: 5X, 10X, 20X, 40X. Figure: 4.21 shows the working principle of polarising optical microscopy.

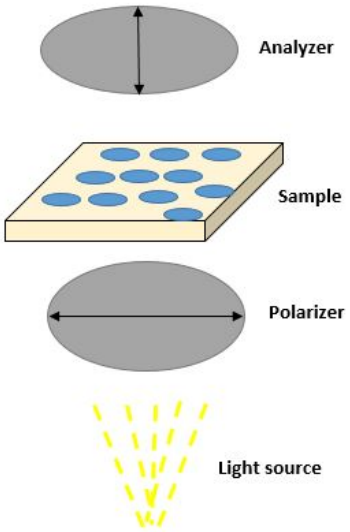

Figure 4.21 *Schematics showing working principle of polarising optical microscope.*

The Schlieren textures presented in Figure: 4.7 evolve due to different orientations of the nematic director possessing random anchoring conditions induced by the susbtrate.

Confocal microscope

Confocal microscope has become a well-established method for studying the microstrucure of soft matter systems. Compared to conventional optical microscopy, a confocal microscope has a better resolution and optical sectioning capability; only light coming from a given focal plane is collected at a any time, thus it is possible to scan deep into the sample and construct a three-dimensional images. In the time sweep mode, it is possible to lock the image on to a specific sample feature and record structural changes in time. Readers are referred to [126] for mathematical description of confocal imaging and to [197**?**] on their principles and applications.

The figure: 4.22 represents the working principle of confocal microscope. Laser light is shone on a dichroic mirror which reflects it along the optical path. The incident beam is then scanned across the sample by a pair of mirrors, passes through the microscope objective and excites the fluorescent specimen. The emitted fluorescent light (green line) returns along the same optical path but passes through the dichroic mirror and before reaching the photomultiplier tube

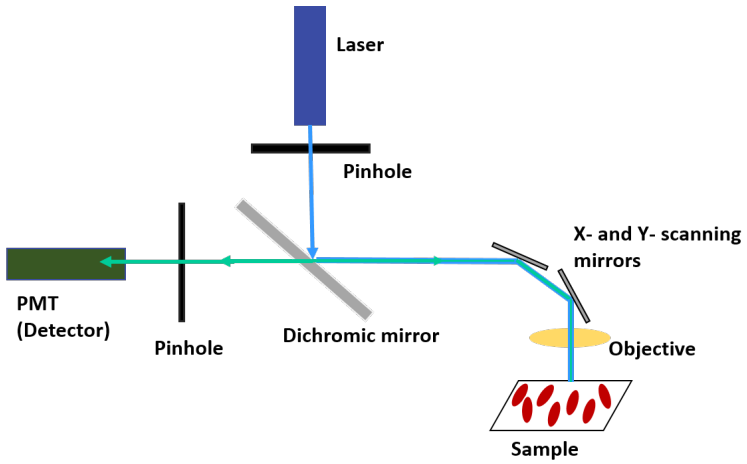

Figure 4.22 *Diagram showing main composnents an working principle of laser scanning confocal microscope.*

and is filtered by a pinhole. By construction, the aperture in front of the detector sits on the conjugate focal plane (hence the name confocal) of the illuminated spot in the sample. The right wavelength laser to illuminate the sample was chosen from the emission spectra of fluoroscence dye. For both NBD and Nile red dyed sample, 488 nm wavelength of laser was used.

Image analysis

The majority of image analysis was performed using standard macros available with an open-source image processing package, FIJI. The size of the colloid cluster was analyzed using the particle tracking method. The spacing between the colloidal particles was analyzed using a routine called radial profile distribution. The extent of director distortion around the particle in NLCs was calculated by taking a line profile across the diameter of the particle.

Chapter 5

Structure and dynamic response of filled thermotropic nematics.

What I cannot create, I do not understand.

- Richard Feynman

The viscoelastic behavior of colloidal filled thermotropic nematic liquid crystal composites was explored. The filler term used in this context refers to micron-sized PMMA hard-sphere, which was dispersed in the 5CB liquid crystalline matrix. Wood et al. conducted a study on concentrated filled thermotropic nematic composite [200]. They dispersed micron-sized PMMA-PHSA particles in 5Cb for a range of vol fraction, $0.005 \leq \phi \leq 0.5$, and performed oscillatory rheology. They have suggested an increase in the storage modulus with the increase of filler concentration, forming a stable gel-like structure beyond $\phi \geq 0.2$. They showed that it was due to the formation of a percolating network structure of disclination lines. These lines are entangled with the particles giving a self-quenched the defect glass state of line defects. Thus proving that topological defects induced by the particles play a crucial role in the bulk rheology of the composites. These defects, as discussed in chapter 3, were induced mostly due to the spontaneous anchoring of the molecules on the particle's surface. A class of soft solid was formed by the combination of dense colloidal suspension and liquid crystal. The exceptional dynamic properties of these uniquely structured composites are, for the first time, explored via rheological studies. First, the oscillatory strain and frequency response of pure 5CB NLCs will be discussed,

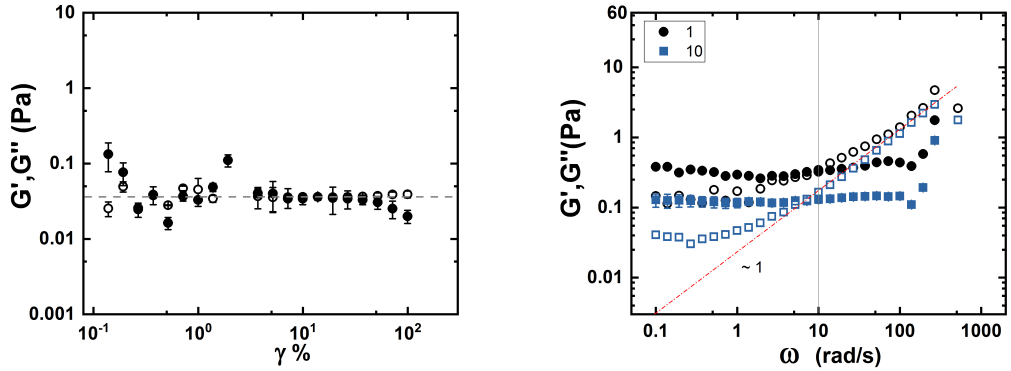

(a) (b)

Figure 5.1 *(a) Oscillatory strain sweep of thermotropic - 5CB NLCs at a frequency of 1 Hz at 500 μm gap size, (b) Frequency sweep thermotropic nematic - 5CB at 1 and 10 % strain at 200 μm gap size. Te gap was reduced to 200 μm for frequency sweep because the pure 5CB LCs behaved more fluid like. Closed symbol represents storage modulus (G') and open symbol represents loss modulus (G'').*

followed by the structure and dynamics of filled NLCs composites of varying concentrations.

5.1 Rheology of a thermotropic nematic liquid crystal - 5CB.

Before composite behaviour is studied, it is important to understand the rheology of the pure NLCs phase.

Figure: 5.1 shows the oscillatory strain sweep of 5CB NLCs. The value of G' and G'' are equal, showing a plateau with a value of $G' = 0.039 \pm 0.014$ Pa for strain, $\gamma\% \leq 10\%$ at 500 μm gap. But as the strain value increases $\gamma\% > 40\%$ the viscous property dominates with $G'' > G'$. The frequency sweep was carried out on the same geometry with the same experimental condition. Angular frequency, ω, was varied from 0.1 to 600 rad/s, and the evolution of G' and G'' was mapped.

At first, we plot the dynamic response of unfilled thermotropic liquid crystal - 5CB at two different strains, $\gamma\%$= 1 and 10 % at 200 μm gap, see Figure: 5.1b. At low frequency, $\omega < 10$ rad/s, the value of storage modulus (G') for 5CB is independent of ω and exhibits a constant value of 0.12 $\pm$ 0.04 Pa and 0.49 $\pm$ 0.18

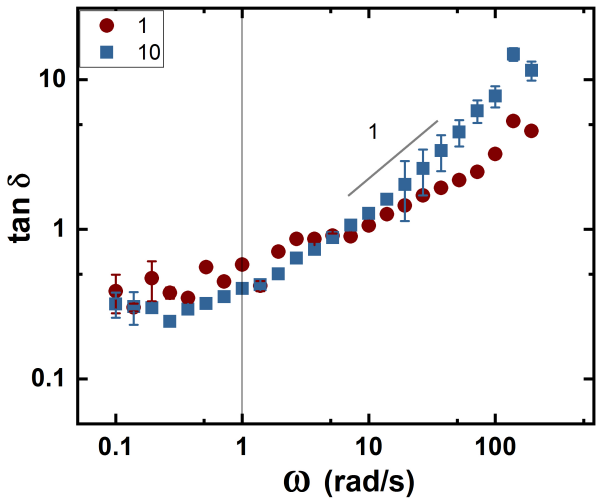

Figure 5.2 *Tanδ = G''/G' as a function of angular frequency, ω, in rad/s for different value of strains, $\gamma\%$ = 1 and 10 % for 5CB NLCs. Tanδ increases linearly with frequency.*

Pa for $\gamma = 10$ % and 1 % respectively with $G' > G''$. The prolonged viscoelastic relaxation at the low-frequency regime, indicative of the plastic behavior, can be attributed to the presence of defect structures in pure nematics. But it is clear from the graph that the value of loss modulus, (G'') increases linearly with frequency, $G'' \propto \omega$, as expected for a Maxwellian fluid [16]. The magnitude of G' is inversely proportional to the applied strain such that $G'(\gamma_{10}) = G'(\gamma_1)\frac{\gamma_1}{\gamma_{10}}$, where 1% and 10% are strain values. The value of G'' also decreases with strain, but the change in magnitude is less significant at a higher frequency, thus revealing an increasing dominance of the viscous regime. However, the crossover frequency ω_c where $G' = G''$ remains same for both the strain values.

Another important value to consider is the frequency dependence of loss tangent - tan δ, which is the ratio of loss to storage modulus. Figure: 5.2 represents the plot of tan δ for pure 5CB LCs at two different strain, γ. Tan δ grows linearly with ω for both strain values for 5CB NLCs, reflecting the liquid-like nature of the liquid crystal.

5.2 Influence of filler on the microstructure and rheology of thermotropic nematics.

Confocal micrographs of two PMMA-PHSA in 5CB composites at $\phi = 0.05$ and 0.25 are shown in Figure: 5.3. PMMA-PHSA particles form disconnected clusters at low volume fraction, $\phi = 0.05$, however they form a dense network like structure at high concentration, $\phi = 0.25$. As discussed in section 2.5, micron-sized PMMA-PHSA particles induce Saturn-ring defects when dispersed in 5CB NLCs. Weak homeotropic anchoring condition with $\frac{Wr}{K} \ll 1$ induces a defect line (or disclination), which encircles the colloid at an orientation normal to the local director orientation [66]. At low colloidal concentration, these Saturn-ring defects remain isolated without interacting with each other, but as the concentration of colloids increases in the composites, these Saturn-rings come in proximity and entangle with a range of possible topological configurations [10, 89, 135]. These entangled disclinations lead to a percolating defect network structure in three dimensions. A series of simulations were carried out on a similar model system with hard-sphere colloids of 1 μm in diameter in nematic liquid crystal by Davide Marenduzzo *et al.* [200] and the result showed up to $\phi_c < 0.18$ a large number of Saturn - ring defects remains isolated but begin to form a large stable entangled structure at $\phi > \phi_c$.

To confirm the entanglement theory, we have imaged defect structures in the composites at high volume fraction sandwiched between two glass slides. Figure: 5.3 shows the entanglement of defects around the PMMA particles in 5CB nematic solution [200]. The dark spherical region represents PMMA-PHSA particles, whereas the dark gray lines surrounding the particles are the defect lines.

The dynamic behavior of the composites can yield information on the interaction between filler and dispersing solvent. The kind of fillers which enhance the stability and mechanical strength of the composite are termed active fillers [48], whereas a filler which weakens the strength of the composites is termed as a passive filler. For the first time, we explore the dynamic rheological response of composites formed from 5CB NLCs with PMMA particles.

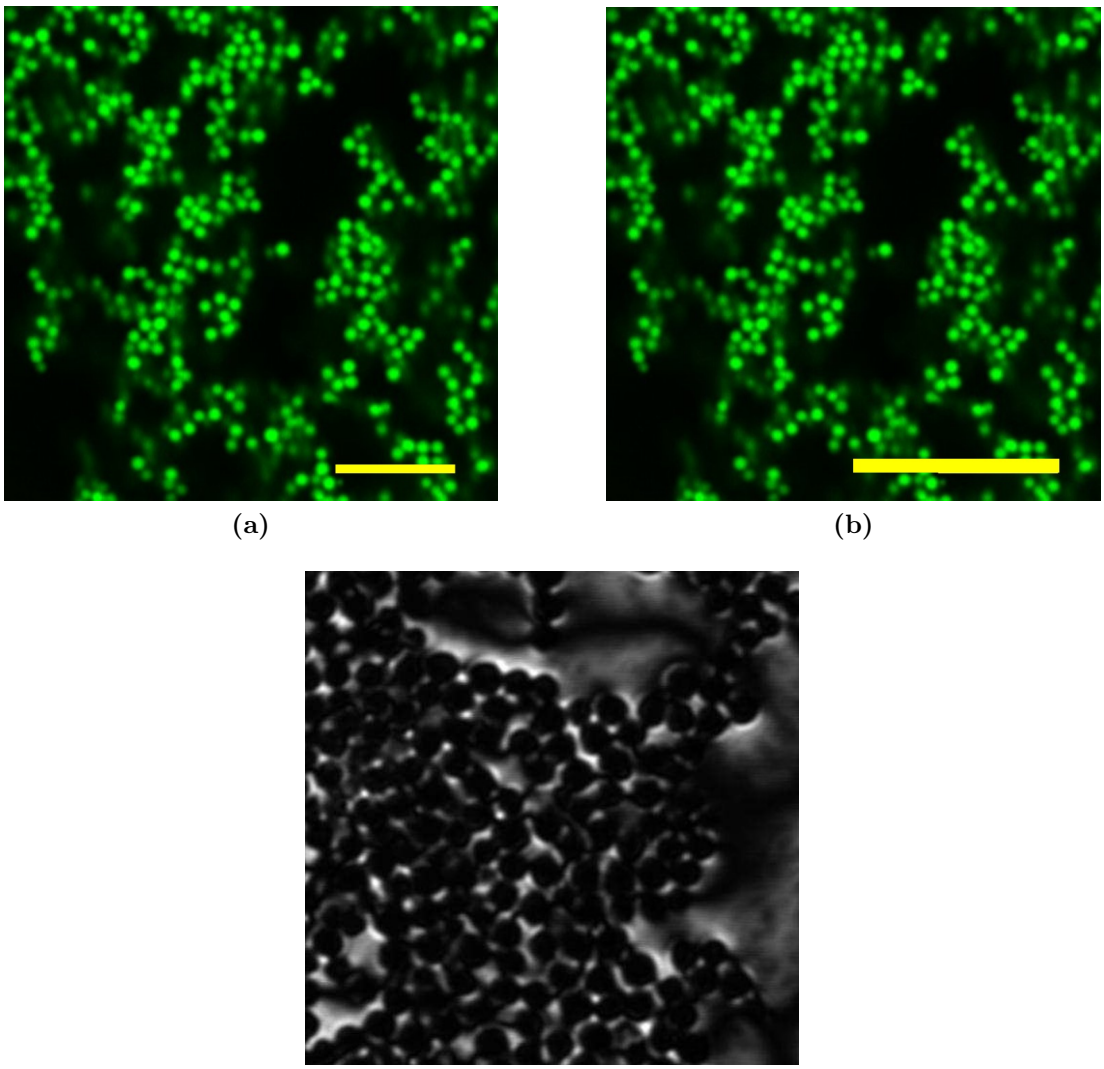

(a) **(b)**

(c)

Figure 5.3 *Confocal micrograph of (a) ϕ = 0.05 and (b) ϕ =0.3 PMMA-PHSA particles dispersed in 5CB. The scale bar is 10 μm, (c) Entangled defect network around PMMA particles dispersed in 5CB LCs. Courtesy Wood et al. (dark circles are particles and grey lines are disclinations).*

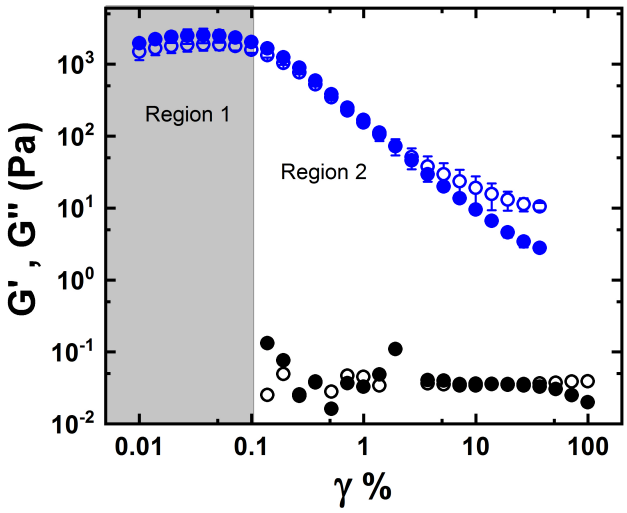

Figure 5.4 *Strain amplitude sweep of $\phi = 0.3$ 5CB (blue) composite depicting two regions, (1) LVR regime and (2) non LVR regime before yielding as compared to pure 5CB LCs (black).*

5.2.1 Oscillatory strain sweep

From manual inspection, it was observed that at $\phi > 0.2$, the composites became a stable gel, as reported in the Figure: 4.9. These gel were stable against sedimentation for more than three months. Figure: 5.4 represents the oscillatory strain sweep for $\phi = 0.3$ (blue) of PMMA-PHSA in 5CB NLCs composite as compared with pure 5CB LCs (black). The addition of filler particles enhances the value of G' and G'' of the composites by five orders of magnitude from 0.039 Pa to 3000 Pa. For $\phi = 0.3$ composite, both G' and G'' have a constant value with $G' > G''$ up to $\gamma \leq 0.1\%$, this region of low strain shows the presence of the linear viscoelastic regime (LVR) where the structure of the sample is not deformed on the application of strain. But on the continuous increase of strain, both G' and G'' begin to decrease, with the former dropping faster than the later eventually crossing and giving way to $G'' > G'$. The crossover of G' and G'' gives the value of the critical yield strain, γ_c. γ_c gives us the maximum strain value beyond which the microstructure of the composite gets deformed. The value of γ_c is 2.47 ± 0.07 % for $\phi = 0.3$ composite. Thus, it becomes important to specify the value of G' and G'' in linear viscoelastic regime (LVR), and they are denoted by $G'(LVR)$ and $G''(LVR)$ here.

We compare the strain sweep for two dense nematic composites at $\phi = 0.2$ (circle) and 0.3 (square) in Figure: 5.5 a. It is observed that the critical value of yield

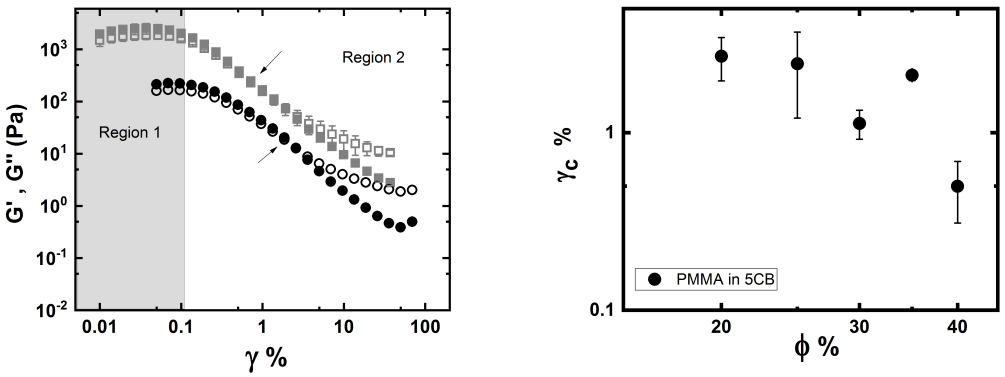

Figure 5.5 *(a) Oscillatory strain sweep for ϕ = 0.2 (black) and ϕ = 0.3 (gray) showing two different yield strain, (b) Yield strain (γ_c) as a function of ϕ for PMMA-PHSA in 5CB composites.*

strain decreases with the volume fraction of the composites, ϕ. However, the LVR ends at the same strain value (see Region 1). A plot of γ_c as a function of ϕ for the composites is plotted in Figure: 5.5 b. The plot reveals that as the concentration of particles in the nematic media increases, the yielding starts to occur at a lower strain. This is explained by the difference in the length of disclinations with ϕ. As the concentration of particles increases, the size of nematic domains decreases up to $\frac{x}{2r} = 1.1$, where x is the separation between the particles and 2r is the diameter of the particles [10]. With the increasing volume fraction, as the value of $\frac{\Delta x}{2r} < 1.1$, the particles are no longer entangled by Saturn-ring but began to jam and arrange themselves in a random packing making the overall composites weak and fragile; thus a lower value of γ is required to break the composite structure [95].

The value of G' and G'' as a function of volume fraction , ϕ, is plotted in Figure: 5.6. Inset graph shows that there two region, (a) at low volume fraction, $\phi \leq 0.1$, where $G'' > G'$ and the composite is fluid like and (b) beyond $\phi > 0.2$ where composites exhibit a solid-like response with $G' > G''$. In the graph, $\phi = 0.001$ denotes the G' and G'' value for just the liquid crystalline medium. A detailed plot of G' and G'' as a function of ϕ for $\phi \geq 0.2$ is shown in Figure: 5.6. At $\phi \geq 0.2$, $G'(LVR_{5CB})$ increases rapidly with ϕ, with a functional form consistent with:

$$G'(LVR_{5CB}) - G'_{5CB_0} = (\phi - \phi_c)^n \tag{5.1}$$

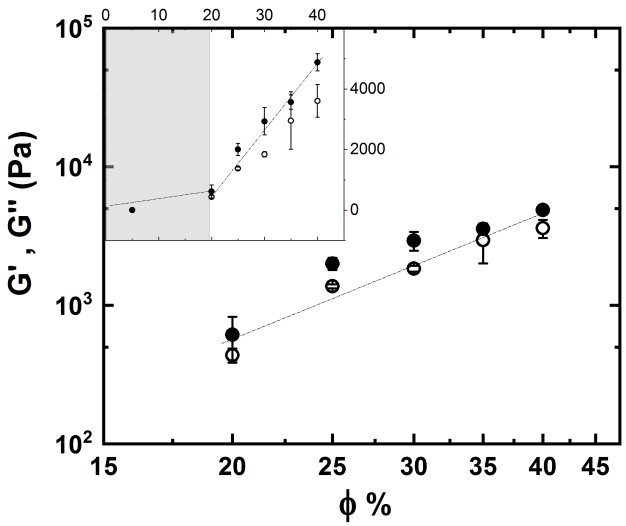

Figure 5.6 *G' and G'' as a function of volume fraction, (ϕ) of PMMA particles dispersed in 5CB nematic liquid crystal. The rapid increase in the value of G' for $\phi \geq 0.2$, for PMMA-PHSA in 5CB is consistent with the functional form of $G'_{LVR}(\phi) \propto (\phi)^n$, with n = 2.04±0.11. Inset shows two regimes for the evolution of G' and G'' for $\phi \geq 0.01$, beyond $\phi \geq 0.2$ the value of G' and G'' for filled nematics shows a rapid increase. The line is a guide to eye.*

where n = 2.04 ± 0.11 and ϕ_c = 0.18 ± 0.02. However, the generation of reliable and consistent data in the case of filled NLCs systems depends to a large extent on the preparation of the sample for the rheological test; thus, the same protocol was followed for sample preparation and data was collectively collected for six different runs. The error in the plot is random error estimated from the standard deviation of the accumulated data. Interestingly, a similar trend is observed for loss modulus (open symbols), indicating that the storage and loss moduli are intimately linked. Both G' and $G'' \propto \phi^2$, possibly due to each colloid supports a two-dimensional Saturn-ring. These ring defects can connect at different topological configuration with the defects, and therefore the number of percolating paths increases with the volume fraction. A similar dependence on the volume fraction was observed for colloidal suspension above glass transition ($\phi \geq 0.58$) [122], however in our nematic composites this behavior occurs at considerably low volume fraction, $\phi \geq 0.18$. Thus, due to the colloidal particles being arrested by disclination in nematic LCs, a stable gel-like structure is formed.

5.2.2 Dynamic response of filled thermotropic nematics.

Frequency sweep measurements were conducted for PMMA-PHSA filled thermotropic 5CB NLCs composites with the same experimental condition as used in the amplitude sweeps. The frequency sweep profile was recorded at different values of strain from 0.1 to 10 % over five decades of frequency, 0.001 to 600 rad/s. The data for frequencies between 0.001-0.01 rad/sec were found to have larger scatter and significant deviations from the higher frequency trends. Hence, the data range was restricted between 0.1 - 600 rad/sec, and the relative storage and loss moduli values were determined. From oscillatory strain sweep, two regions (a) LVR and (b) yielding were identified, see Figure: 5.4.

Region-1

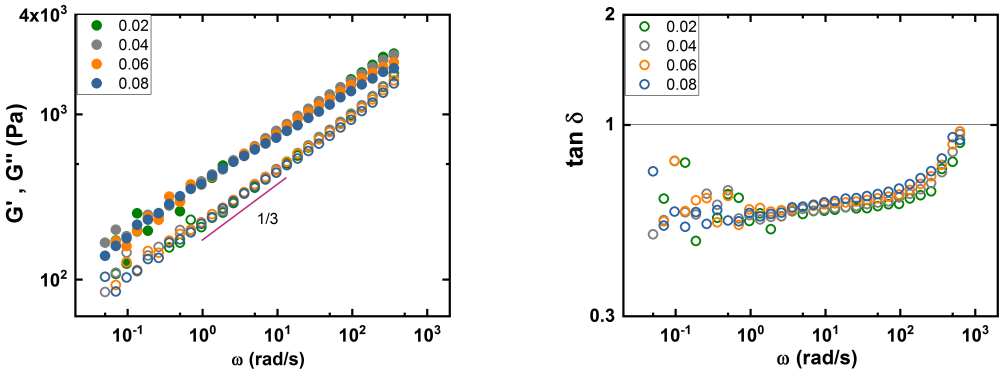

Figure 5.7 *(a) G' and G'' as a function of angular frequency ω in rad/s at low strain, $\gamma \leq 0.2\%$ in the LVR (region 1) where G' and G'' remains constant as compared with $\gamma\% = 0.6\%$ where the microstructure of the sample has deformed with decreasing value of G' and G'', (b) Tanδ as a function of ω in region 1.*

The LVR for $\phi = 0.3$ composites were restricted to $\gamma \leq 0.1$ %. The frequency sweep profile was recorded for the strain values below 0.1% is reported in the Figure: 5.7. Both G' and G'' increase with frequency with $\omega^{1/3}$. The plot of tan δ reveals that the composites behave as an elastic solid with tan $\delta < 1$ for the entire frequency spectrum.

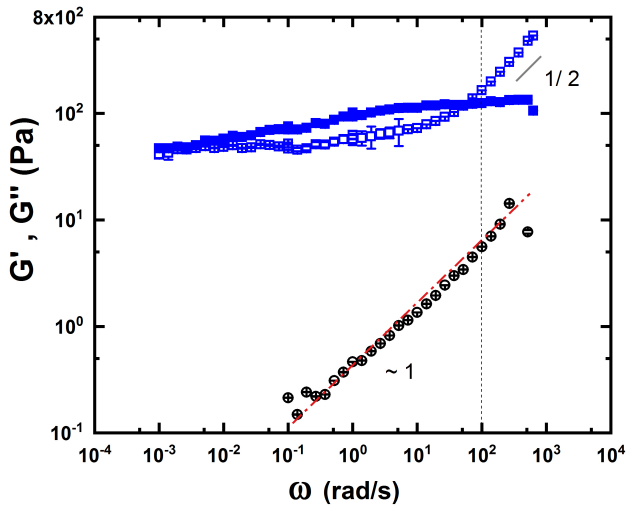

Figure 5.8 *Storage modulus (G') and loss modulus (G'') as a function of angular frequency ω at $\gamma\% = 0.6\%$ for $\phi = 0.3$ of PMMA in 5CB NLCs (blue) as compared to 0.05 of PMMA in 5CB NLCs (black). G' is in closed symbol and G'' in open symbol. For $\phi = 0.3$ composite, G'' grows as $\omega^{1/2}$ at higher frequency, $\omega > 70 \pm 12$ rad/s.*

Region-2

The yielding region for the nematic composites was defined for strain values, $\gamma > 0.1\%$. The frequency dependence of high ($\phi = 0.3$)(blue) and low ($\phi = 0.05$) (black) volume fraction for PMMA-PHSA in 5CB at $\gamma = 0.6\%$ is shown in Figure: 5.8. This strain of $\gamma = 0.6\%$ is beyond the LVR but lower than γ_c. The geometry with 500 μm was not suitable for measuring the frequency sweep of pure 5CB NLCs since it was too fluid-like. Thus for comparison, we have plotted the G' and G'' for $\phi = 0.05$ composite. The mechanical spectrum of G' shows a plateau region, which is related to the formation of the elastic structural network due to the interaction between colloids and nematic domains. However, G'' shows a weakly negative slope, but gentle yielding is observed above a critical frequency, ω_c with $G'' \propto \omega^{1/2}$. For $\phi = 0.05$, $G'' \propto \omega^1$ for all measured frequencies consistent with the high-frequency regime for a nematic liquid crystal without inclusions [108].

Another important expression to understand is the frequency response of loss tangent or $\tan\delta = \frac{G''_T}{G'_T}$. Figure: 5.9 a and b show the value of $\tan\delta$ for filled nematics at two different strain, γ, a) 0.6% which is less than γ_c and b) 4% which is greater than yield strain γ_c. Tan δ value for different concentration suspension

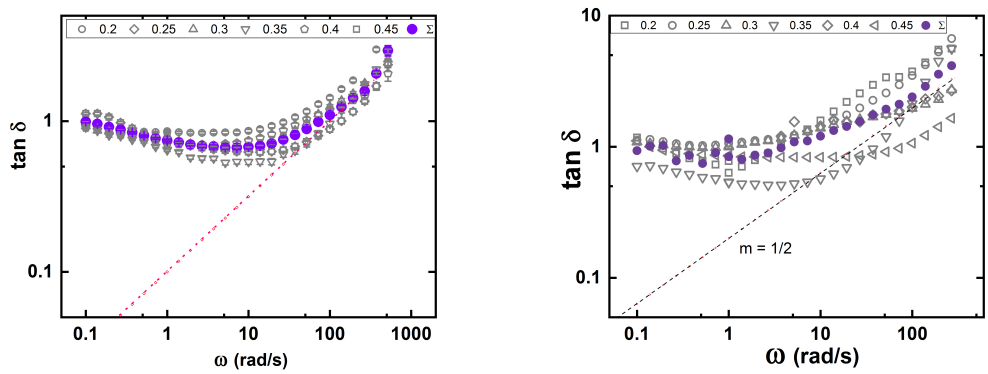

(a) (b)

Figure 5.9 *Tan δ = G"/G′ as a function of angular frequency ω in rad/s for different volume fraction ϕ of PMMA in 5CB at (a) $\gamma = 0.6\% < \gamma_c$ and (b) $\gamma = 4\% > \gamma_c$. The red line has a slope of 1/2. It is seen that samples of different volume fractions collapse onto one average curve (purple) and at $\omega > 70 \pm 12$ rad/s tan δ has a slope of 1/2 as a function of angular frequency. This behavior is observed for all strain values.*

can be collapsed into one master curve, as shown in dark-purple; this behavior could be replicated at all values of applied strain in the yielding region. Thus, it was concluded the value of tan δ is not dependent on the filler concentration beyond $\phi = \phi_c \geq 0.2$ for the thermotropic nematic composites, $\phi_c = 0.18$ is the onset of stable gel formation. A negative slope of -0.101 $\pm$ 0.003 for tan δ at low-frequency, $\omega \geq 10$ rad/s, suggests strong glassy elastic behavior. However, at a critical frequency, ω_c, the viscous behavior becomes dominant and, above this value, tanδ increases as $\sim \omega^{1/2}$. Initially, the observed independence of volume fraction is surprising since the form of G' increases with ϕ^2, but this increment with ϕ is also observed for G''; hence tan δ which is the ratio both the moduli becomes independent of the volume fraction of colloids.

In a colloidal composite in an isotropic solvent, we would expect tan δ to be dependent on the volume fraction as the concentration of particles affects the interparticle distance. In a nematic solvent, however, disclinations percolate because colloids are excluded from larger nematic regions and are located close to one another, bound by entangled disclinations. The dynamic independence suggests that the nematic phase determines the elastic and viscous properties of the composite, and its interaction with the colloids does not alter as the volume fraction is increased. Colloids, merely, give rise to disclinations, and the volume fraction increases the density of disclinations in the system, thus

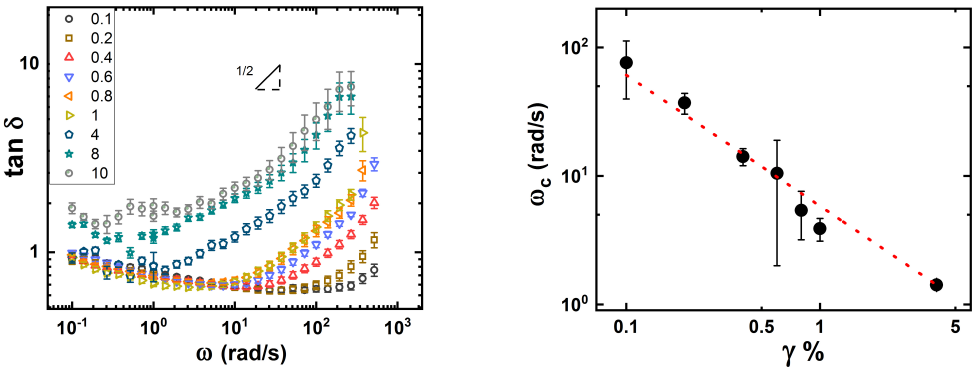

(a) (b)

Figure 5.10 *(a) Tan $\delta = G''/G'$ as a function of angular frequency ω in rad/s for all different vol fraction ϕ of PMMA in 5CB averaged for $\gamma = 0.1 - 10\%$. tanδ has a slope of 1/2 at ω 70 $\pm$ 12 rad/s, (b) critical frequency, $\omega_c = min(\tan\delta)$ as a function of $\gamma\%$, $\omega_c = A\gamma^{-1}$, with $A = 0.779 \pm 0.023$.*

increasing the strength of the composites. The dynamic behavior suggests there are no colloid-colloid interactions as the volume fraction is increased up to $\phi = 0.45$. Experiments were not performed above this limit since samples were difficult to handle as they started to crumble, indicating the composite character was changing. At $\phi = 0.45$, we expect the interparticle separation reduce to $r/d \sim (0.64/0.45)^{1/3} \sim 1.12$ (presuming colloids touch at random close packing $\phi = 0.64$). This value is approaching the ratio of particle radius to the interparticle distance, $r/d \sim 1.1$, between colloids entangled by disclinations, reported through computer simulations by Araki *et al.* [10]. Thus it appears that insufficient solvent is available to create a disclination-dominated composite at higher volume fractions.

The tan δ values of PMMA-PHSA in 5CB composites as a function of frequency, ω, for different strain, $\gamma = 0.1 - 10\%$ averaged over all volume fraction ($0.2 \geq \phi \geq 0.4$) are plotted in Figure: 5.10 a. The plot reveals that the value of tan δ is directly proportional to γ. The more liquid-like character of the PMMA-PHSA in 5CB composites are reflected at higher strain, e.g. $\gamma = 4\%$ where tan $\delta > 1$ beyond 1 rad/s, with tan$\delta \sim \omega^{1/2}$. This is because the suspension has yielded and nematogens have reoriented in the direction of flow at higher $\gamma > \gamma_c$. At lower strain, for example at $\gamma = 0.4$, the value of tan $\delta < 1$ at low frequencies because the suspension structure is still not broken with $G' > G''$. It is clear that the frequency dependence of PMMA-PHSA suspension is independent of

the concentration of the filler present in the 5CB NLC but depends on the strain and applied angular frequency.

Thus, we conclude, the curve of tan δ is non-linear, with tan δ showing slight negative slope at lower frequency and an increase with $\omega^{1/2}$ beyond a critical frequency, ω_c. We define ω_c, as the frequency where the value of tan δ = minimum. The plot (Figure: 5.10 b) of ω_c as a function of strain, γ shows their inverse dependence. Next, we propose a theory to explain the unique dynamic behavior of the thermotropic composites.

5.3 Theory for viscoelasticity of filled nematic composites

To describe the unusual behaviour, $G'' \sim \omega^{1/2}$, we have observed we present a new theory to describe the viscoelastic behaviour. We break down the description into elastic, G' and viscous, G'' parts.

5.3.1 Elastic contributions

The storage modulus describes the elasticity of the material and is the sum of two different contributions $G' = G'_{Rey} + G'_d$. G'_{Rey} describes the elasticity of a nematic liquid crystal flowing between parallel plates. It was described by Alexandro Rey [108] and at high frequencies was given by,

$$G'_R = \left((\frac{\alpha_2}{\gamma_r})^2 (2\omega\eta_{bend} K) \right)^{(1/2)} \tag{5.2}$$

where α_2 is Leslie viscosity co-efficient = - 0.085 Pa.s for 5CB, γ_r is the rotational viscosity is known to be to be 0.081 Pa.s for 5CB, η_{bend} is the bend viscosity = $\frac{\gamma_r - \alpha_2}{\eta_2}$ = 3.117 Pa.s for 5CB , K is the average elastic constant of LCs, taken to be 5.5E-12 N for 5CB and ω is the applied angular frequency. For 5CB $G'_{Rey} \sim 10^{-5}$Pa.

The elasticity of a liquid crystal, caused by the presence of disclinations, was

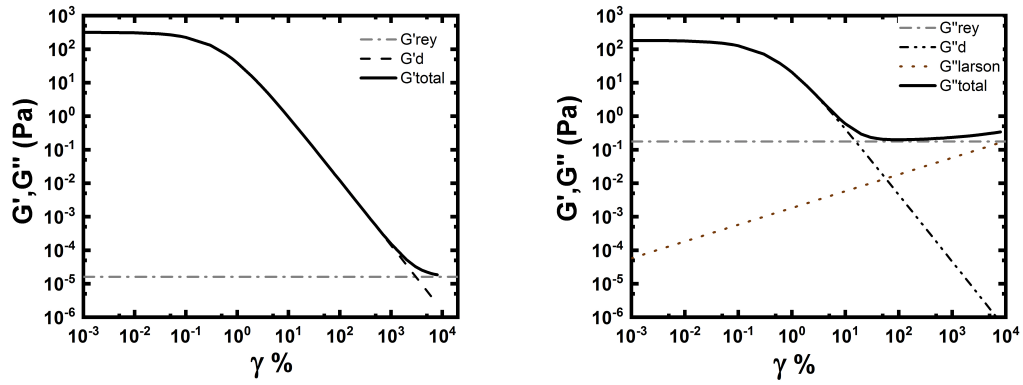

Figure 5.11 *Strain dependence of the theoretical contributions to G' and G".*

described by Weitz *et al.*

$$G'_d = (\frac{T}{d_{net}})^2 \tag{5.3}$$

G'_d describes the elasticity of a liquid crystal across which defects span at an average separation, d_{net}. We modify this expression for our composite to $G'_d = \left(\frac{T}{d_{net}}\right)^2 p(\phi)^2$ because we know from experiments that $G' \sim \phi^2$ (see Equation: 6.1). Saturn-ring defects can connect at multiple points around the ring, and therefore the number of percolating paths increases with the volume fraction.

In our case the colloids are separated by $\Delta x = 1.11r$ where $D = 2r$ is the diameter of the particles. We assert that disclinations yield at a critical strain of $\gamma_c = \frac{r_c}{1.1D}$ where r_c is the radius of a disclination. The radius of disclination for 5CB LCs is 5 nm [139]. Above this strain disclinations yield such that the density of the disclinations increase as $d_{net} = \Delta x \gamma_n$ where $\gamma_n = (\frac{\gamma_c + \gamma}{\gamma_c})$. The contribution form both the elastic terms are shown in Figure: 5.11 a.

5.3.2 Viscous contributions

The viscous behavior of the composite is determined by two contributions $G'' = G''_{Rey} + G''_d$. The viscous behavior of the composite is determined by the Ericksen number - the ratio between viscous and elastic forces on the sample. The Ericksen number is defined by $E_r = \frac{L^2 \gamma_r \dot{\gamma}}{K}$, where K is the elastic constant, γ_r is the rotational viscosity, $\dot{\gamma}$ is the shear rate and L is the relevant length scale. Disclinations and particle surfaces behave as walls that confine the nematic liquid crystal. Larson described the viscosity of a confined nematic as $\eta = \gamma_r E_r^{-0.5}$ [12].

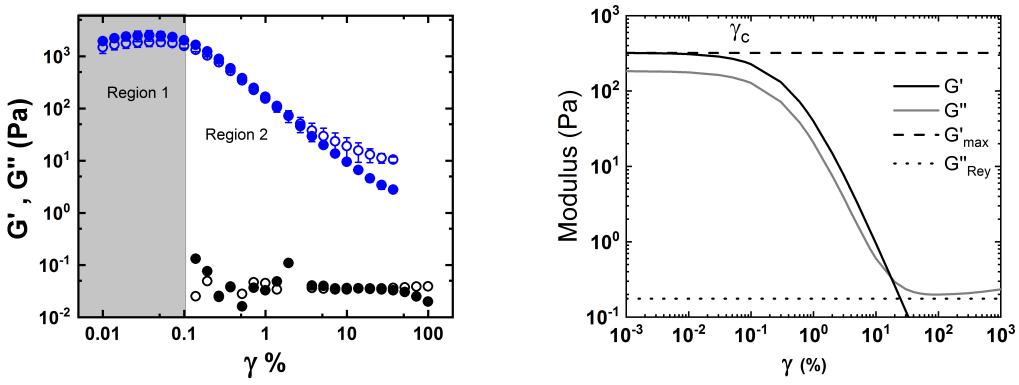

Figure 5.12 *(a) The comparison of evolution of G' and G'' as a function of the applied strain for 5CB NLCs (black) and ϕ= 0.3 PMMA-PHSA 5CB composite(blue) with G' and G'' showing a plateau up to $\gamma \leq 0.1\%$ and yielding at a γ_c= 2.47± 0.79 %, (b) The strain dependence plot from theory.*

We use this to assert that

$$G''_a = \omega_n \gamma_r E_r^{-0.5} p(\phi)^2 \tag{5.4}$$

for a nematic liquid crystal confined by dispersed colloids. For oscillatory flow, $E_r = \frac{a^2 \gamma_r \gamma_n \omega_n}{2\pi\omega}$ where a is the average dimension of nematic domains, the size of which will be determined by the ratio of the elasticity, K, to the anchoring energy, W of nematogens at the surface of colloids such that $a \sim K/W$. The growth of these domains forces colloids to approach one another and a ~ 10 μm. The frequency, $\omega_n = \omega_c + \omega$, where $\omega_c = \frac{2\pi K}{a^2 \gamma_r \gamma_n}$ is the critical frequency at which flow overcomes the elasticity of the composite. Inserting our definition of the Ericksen number into the Equation: 5.4 we find that

$$G''_a = \omega_n \gamma_r \left(\frac{2\pi K}{a^2 \gamma_r \gamma_n \omega_n} \right)^{0.5} p(\phi)^2 \tag{5.5}$$

so that,

$$G''_a = \left(\frac{2\pi K \gamma_r \omega_n}{a^2 \gamma_n} \right)^{0.5} p(\phi)^2 \tag{5.6}$$

when we expand $\omega_n = \omega_c + \omega$ we find that

$$G''_a = p(\phi)^2 \frac{2\pi K}{a^2 \gamma_n} + p(\phi)^2 \left(\frac{2\pi K \gamma_r \omega}{a^2 \gamma_n} \right)^{0.5} \tag{5.7}$$

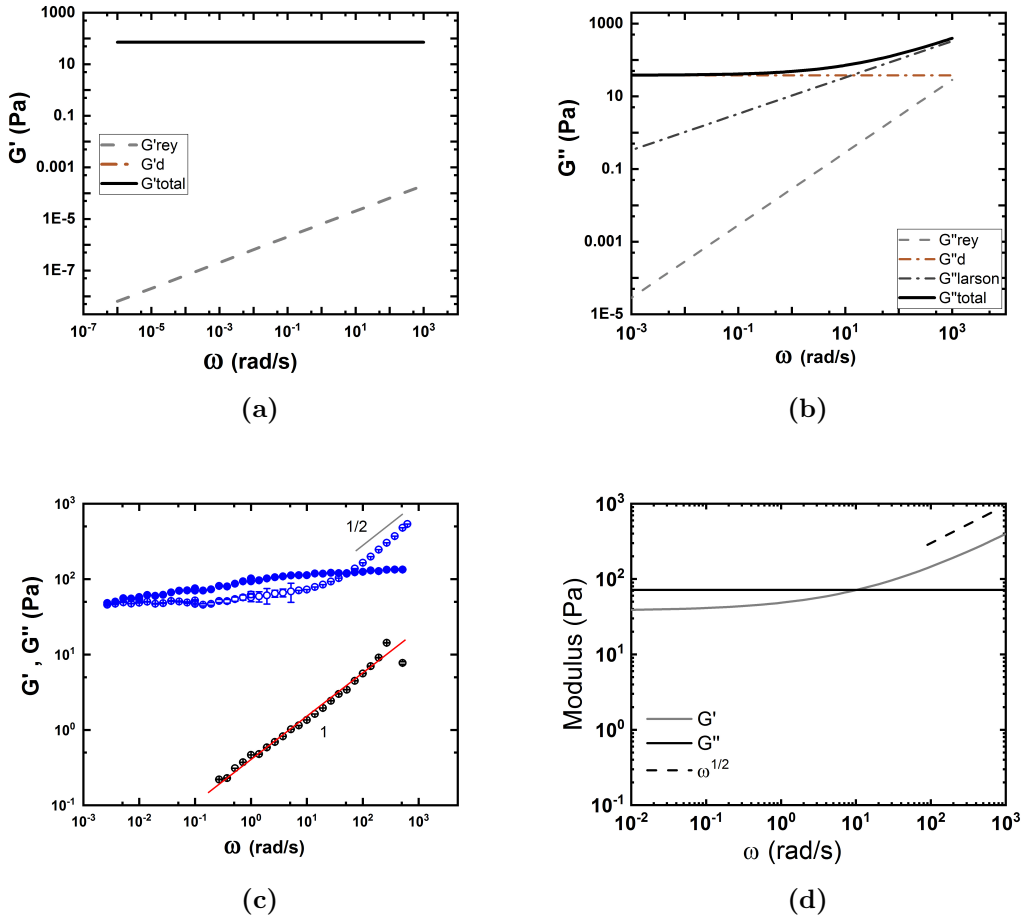

Figure 5.13 *Frequency dependence of the theoretical contributions to (a) G', (b) G'', (c) Experimentally measured value of G' and G'' as compared with the (d) theory prediction.*

The left hand side describes the plateau, G''_d, observed at low frequencies where the elasticity dominates. The right hand side, G''_c, described the yielding behaviour which occurs after the critical frequency, ω_c has been exceeded and $G''_a = G''_c + G''_d$.

We assume that the viscous term, $G_{Rey} = \eta_2\omega$, where η_2 is the Miesovicz viscosity for flow alignment. These contributions to the viscous loss term are shown in Figure: 5.13.

$tan\delta = G''/G'$. At low frequencies

$$tan\delta = \frac{2\pi K}{T}.\frac{1}{\gamma_n}.\frac{d_{net}^2}{a^2} \tag{5.8}$$

which indicates that $tan\delta$ is not dependent on the volume fraction but is

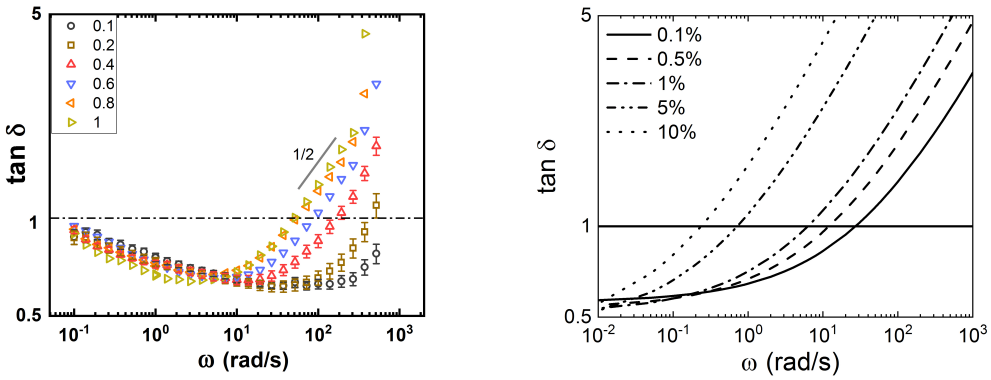

Figure 5.14 *Tan δ values from (a) experiment and (b) theory.*

dependent on the disclination density and size of the nematic domains. A comparison of experimental tan δ values with the theoretical prediction is shown in Figure: 5.14.

5.4 Summary

To summarize, the most important findings are:

1. G' and $G'' \propto \phi^2$, possibly due to each colloid supporting a two-dimensional Saturn-ring. This power-law dependence on volume fraction is similar to colloidal suspensions above the glass transition, $\phi_g = 0.58$. However, the glass transition for filled nematics is considerably lower at $\phi = 0.18$.

2. For the first time, we show that $G'' \propto \omega^{1/2}$ on yielding. We present a theory that indicates the yielding behavior is governed by the Ericksen number, E_r, and the viscous behavior is determined by the confined nematic regions.

3. We find that the frequency dependence of the composites is independent of the volume fraction, ϕ, indicating that it is neither active or passive filled system and the behavior of composite is determined by the intrinsic property of the nematic phase. The colloids merely serve to create and support Saturn-ring defects.

Chapter 6

Exploring shear rheology and microstructure of filled nematic lyomesophases.

For the first time, we have studied the bulk rheology of filled lyotropic nematics for a range of volume fraction and compare it with the thermotropic counterpart, which is now well understood. To study the rheology behavior of colloids in lyotropic LCs in bulk, we have dispersed hard-sphere and deformable colloids in lyotropic nematic LCs made from water, SDS, and 1-decanol [5–7, 81, 150].

Following a similar route as the filled thermotropic system, we have studied the oscillatory rheology of uncharged PMMA-PVP particles dispersed in lyotropic nematic, NC1, for a range of volume fractions, ϕ, followed by their dynamic behavior.

6.1 Rheology of lyotropic nematic NC1 LCs.

A strain amplitude sweep of NC1 NLCs as compared with 5CB NLCs is presented in Figure: 6.1a. NC1 NLCs show fluid-like behavior with $G'' > G'$, and the order of magnitude of G'' for NC1 LCs is two orders of magnitude greater than for 5CB. The dynamic response of pure lyotropic nematics is reported in the figure: 6.1)b. NC1 NLCs shows Maxwell fluid-like behavior with $G' \propto \omega^2$ and $G'' \propto \omega$ before reaching a plateau at higher frequency, $\omega > 200$ rad/s. The slope of $G''(NC1)$

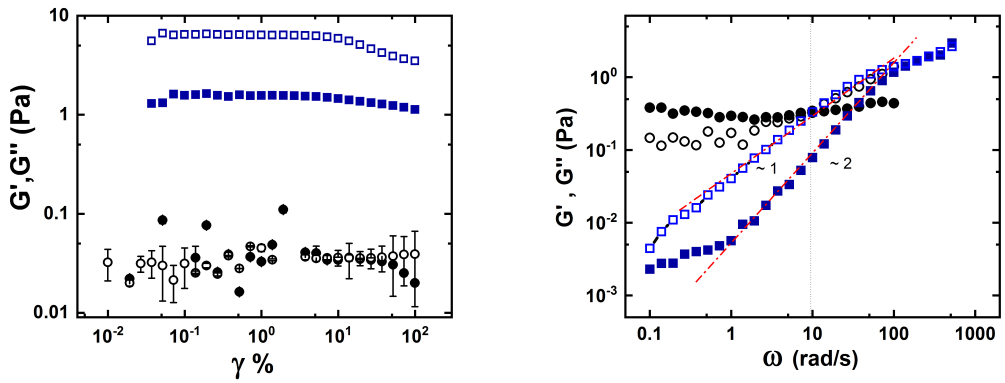

Figure 6.1 *(a) Oscillatory strain sweep of thermotropic nematic - 5CB NLCs (black circle) at a frequency of 1 Hz as compared with strain sweep of lyotropic nematic - NC1 NLC (blue square)s, (b) Frequency sweep of 5CB NLCs (circle) as compared with NC1 LCs (square) at 1% strain. Closed symbol represents storage modulus (G') and open symbol represents loss modulus (G'').*

is the same as that of $G''(5CB)$ above $\omega \leq 10$rad/s. In the entire frequency spectrum of NC1 LCs, $G'' > G'$ therefore NC1 LCs have fluid-like properties, unlike 5CB LCs, which is elastic at low frequency. The increase in the value of G'' at a higher frequency can be attributed to the alignment of the rod-shaped micelles present in NC1 towards the direction of flow, and these micelles were not able to align back to its original position in the short interval of time.

A plot of loss tangent, $\tan\delta = \frac{G''}{G'}$, at different strain values is plotted in Figure: 6.2. The absolute value of $\tan\delta$ is greater than 1 but the curve is non-linear. At low frequency, $\omega \leq 10$ rad/s, $\tan\delta$ plateaus before decreasing with increasing frequency.

6.2 Influence of uncharged filler

PMMA particles stabilized by PVP were dispersed in NC1 LCs for a range of different volume fractions, $0.05 \leq \phi \leq 0.5$, and the resulting composites were imaged and exposed to oscillatory rheology. The confocal micrograph of $\phi = 0.05$ and $\phi = 0.25$ of NC1 composites are shown in Figure: 6.3. At low concentration, $\phi = 0.05$, PMMA-PVP microspheres form a small disconnected cluster with large nematic domains between them, however at high concentration they form a spcae

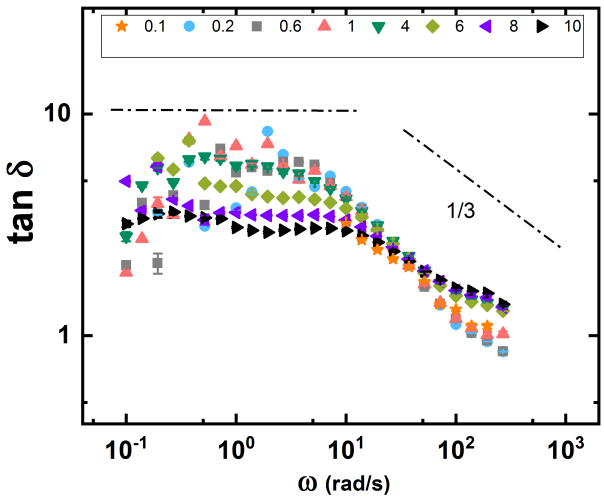

Figure 6.2 *Tanδ = G''/G' as a function of ω rad/s for different strain values for pure NC1 LCs. Tan δ shows a plateau up to ω = 10 rad/s and then decreases with $\omega^{-1/3}$ up to ω = 100 rad/s.*

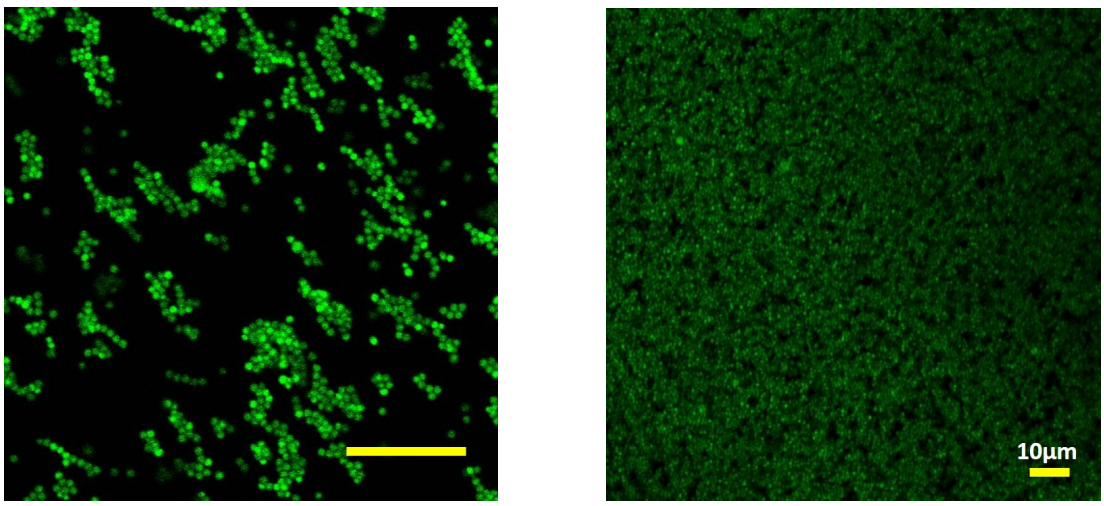

(a) **(b)**

Figure 6.3 *(a) Small disconnected cluster of PMMA-PVP microspheres in NC1 LCs at ϕ = 0.05, (b) Network clusters of PMMA-PVP particles spanning NC1 LCs. (dark region represents LCs media whereas green spheres represents particles) Scale bar is 10 μm.*

spanning network like cluster. From image analysis of five images at different x,y,z of the same sample, the average cluster area calculated = 25.14 ± 2.92 μm^2, however at higher concentration, $\phi = 0.25$, PMMA-PVP form entangled defect connected structure spanning over the space. The area of the nematic domain (black region) has decreased considerably from 400.90 ± 12.31 μm^2 at $\phi = 0.05$ to 5.12 ± 1.12 μm^2 at $\phi = 0.25$.

6.2.1 Oscillatory strain sweep

Oscillatory strain sweep curve for lyotropic nematic composites is shown in Figure: 6.4. It compares the strain amplitude curve of PMMA-PVP filled NC1 NLCs to PMMA-PHSA filled 5CB composites at a volume fraction, $\phi = 0.3$. Both the curves also draw a comparison with their respective NLCs. It can be seen that with the addition of the filler particles, the value of G' is elevated by four orders of magnitude for both lyotropic and thermotropic composites. The value of G'' also increases with the addition of filler particles.

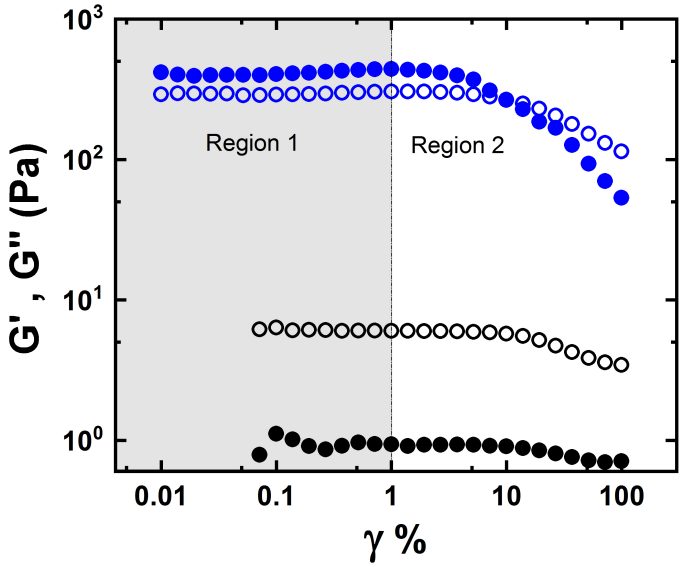

Figure 6.4 *The evolution of G' and G'' as a function of applied strain for NC1 LCs (black) with $G'' > G'$ and $\phi = 0.3$ PMMA in NC1 composite (blue) with G' and G'' shows a plateau up to $\gamma \leq 1\%$ and finally yielding at $\gamma = 7.18 \pm 0.39$ %. Closed symbol denotes G' and open symbol represents G''.*

A comparison of strain sweep for two concentrated lyotropic composites is shown in the Figure: 6.5 (a) Both ($\phi = 0.2$ (black) and 0.3 (grey)) the composites

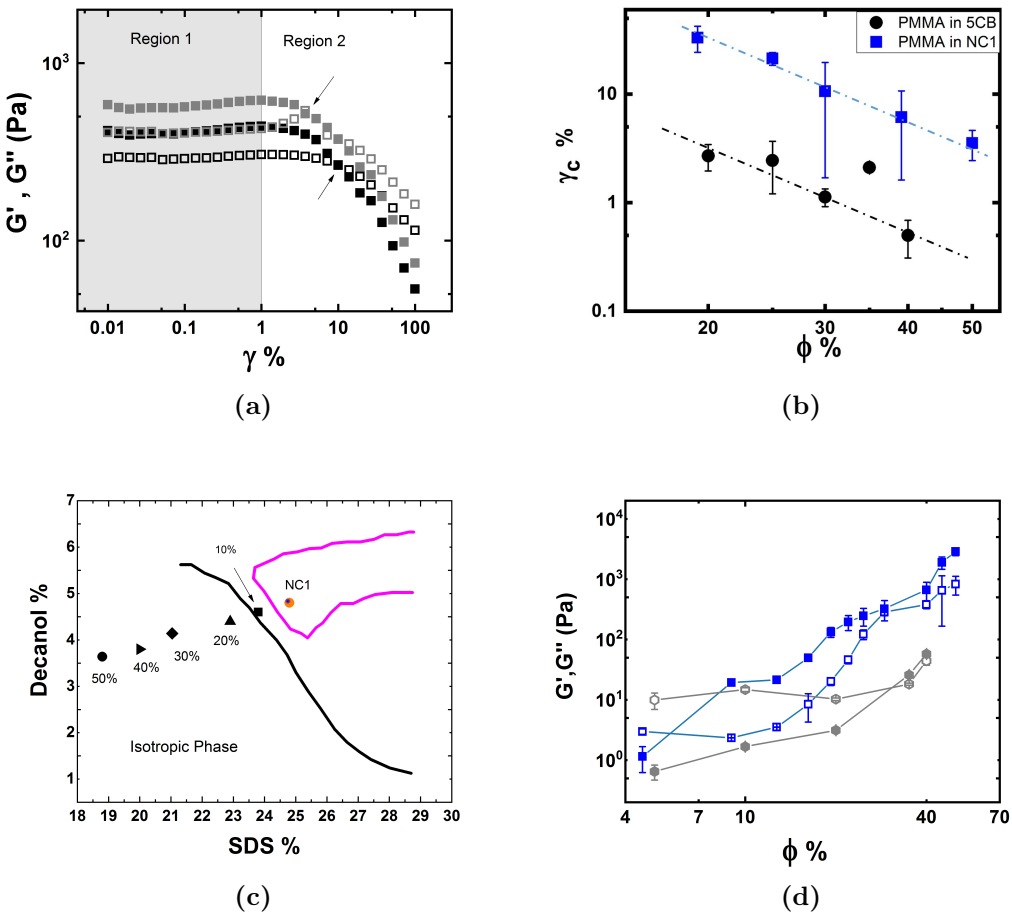

Figure 6.5 *(a) Strain sweep for $\phi = 0.2$ (black) and $\phi = 0.3$ (grey) composites. The LVR regime remains same for both the concentration denoted by region 1 and yielding is denoted by region 2, (b) Critical yield strain (γ_c) as a function of ϕ for PMMA in NC1 LCs (blue) as compared with PMMA in 5CB composite (black), (c) Partial phase diagram of SDS-Decanol-water LCs for isotropic and nematic phase, the points depict the wt% of SDS-Decanol added for different ϕ samples. (d) Plot comparing the value of G' (closed symbol) and G'' (open symbols) for different ϕ of filled nematic (blue) to isotropic (grey) composites.*

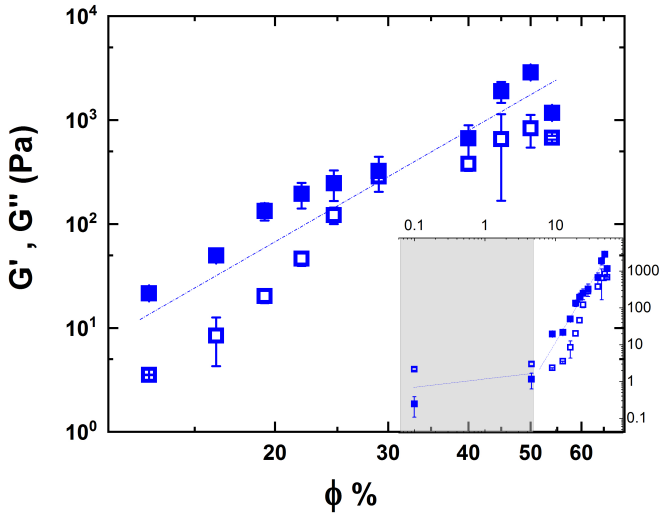

Figure 6.6 *G' and G'' as a function of volume fraction, ϕ for lyotropic composites. For $\phi \geq 0.2$ the value of G' and G'' for filled nematics shows a rapid increase. Line is $\propto \phi^2$. Closed symbol represents G' and open symbol represents G''.*

have the same LVR denoted by region 1 before yielding denoted by region 2. However, the yield strain, γ_c decreases with increasing concentration, a behavior also observed in filed thermotropic nematics. To confirm that the elevated moduli are due to the nematic structure of the lyotropic system, a comparison of NC1 composite to an isotropic composite is studied. PMMA-PVP particles were dispersed in the isotropic phase of the same lyotropic system, Figure: 6.5c shows the partial phase diagram of SDS-decanol-water lyotropic LCs with points representing the different volume fraction of isotropic composites. Figure: 6.5d represents the plot of G' and G'' as a function of ϕ for both filled nematic (blue) and isotropic (grey) phase. $G' > G''$ for all filled nematic composites beyond $\phi \geq 0.18$, whereas for the filled isotropic system, the viscous behavior dominates up to $\phi < 0.4$ with $G'' > G'$. The isotropic composites exhibit elastic behavior at a very high concentration, $\phi \geq 0.4$, compared to nematic composites, thus confirming the enhanced elasticity is due to the nematic structure.

The value of G' and G'' as a function of volume fraction, ϕ, is plotted in Figure: 6.6. The inset graph shows that there are two regions, (a) at low volume fraction, $\phi \leq 0.08$, where $G'' > G'$ and the composite behaves like a fluid and (b) beyond $\phi > 0.2$ where the composite exhibit solid-like response with $G' > G''$. In the graph, $\phi = 0.001$ denotes the G' and G'' value for just the liquid crystalline medium. At $\phi \geq 0.2$, $G'(LVR_{NC1})$ increases rapidly with ϕ, with a functional

form consistent with:

$$G'(LVR_{NC1}) - G'_{NC1_0} = (\phi - \phi_{c_0})^m \tag{6.1}$$

where m = 2.19 ± 0.17 and ϕ_c = 0.22 ± 0.04. The relation between G' and ϕ agrees well with the thermotropic counterpart as PMMA microspheres induce Saturn-ring defects in both lyotropic and thermotropic nematic LCs.

6.2.2 Dynamic response of filled lyotropic nematics.

The frequency response of PMMA-PVP in NC1 LCs were studied for a frequency range from 0.1 to 600 rad/s. From the strain sweep, two different regions were identified, (1) LVR for strain, $\gamma \leq 1\%$ and (2) yielding region for $\gamma > 1\%$. The dynamic response of lyotropic nematic in these two regions will be discussed.

Region-1

Figure: 6.7 (a) and (b) shows the dynamic moduli comparison for dilute ($\phi < 0.2$) and concentrated ($\phi > 0.2$) lyotropic composite in the linear viscoelastic regime (Region 1). It is observed the dilute composites follow liquid like behavior with G' $\propto \omega^2$ and $G'' \propto \omega$ same as pure liquid crystal (black), however the concentrated composites shows a weak dependence on frequency with G' and $G'' \sim \omega^{1/3}$.

The mechanical spectrum of G' and G'' for ϕ = 0.3 composites was further studied at different values of strain within the LVR region. The LVR for ϕ = 0.3 composites were restricted to $\gamma \leq 1$ %, thus the frequency profile recorded for strain, γ = 0.1, 0.4 and 0.6 % is reported in figure: 6.7 c. Both G' and G'' increases with frequency with $\omega^{1/3}$. A behavior which is observed for all concentrated lyotropic composites in the LVR region.

Region-2

The yielding region for the lyotropic nematic composites was defined for strain values, $\gamma > 1\%$. The frequency dependence of high (ϕ = 0.3) (blue) volume fraction for PMMA-PVP in NC1 composites at $\gamma = 6\%$ compared with pure NC1 LCs is shown in Figure: 6.8. One can see that the elastic modulus (G') is constant

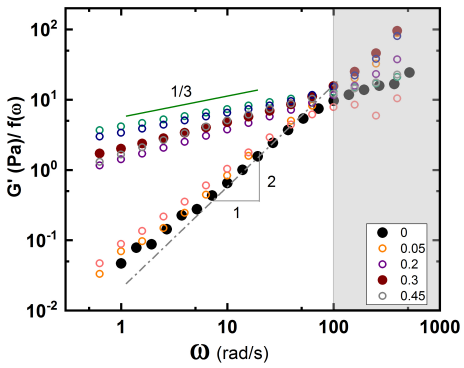

(a)

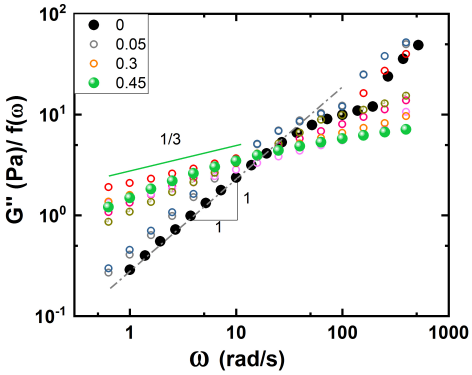

(b)

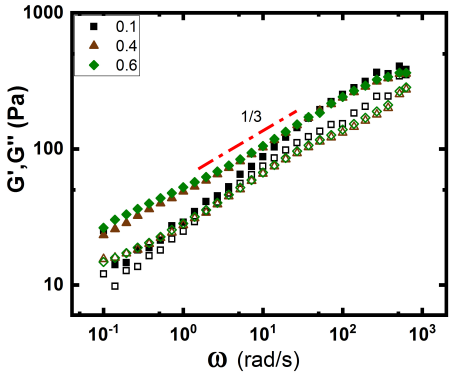

(c)

Figure 6.7 *Dynamic moduli (a) G' and (b) G'' comparison in the LVR (region 1) for different volume fraction of the lyotropic composites, (c) for $\phi = 0.3$ composites in the LVR region both G' and G'' increases as a function of angular frequency as $\omega^{1/3}$.*

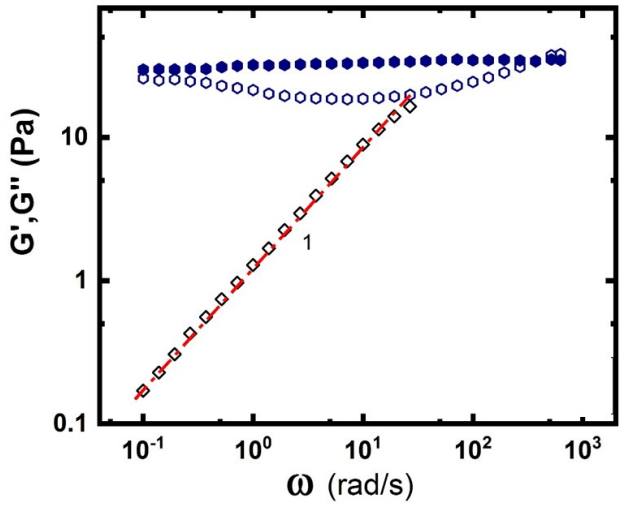

Figure 6.8 *G' and G'' as a function of angular frequency ω in rad/s at $\gamma\% = 6\%$ for $\phi = 0.3$ of PMMA in NC1 NLCs (blue) as compared to NC1 NLCs (black). G' is in closed symbol and G'' in open symbol.*

in a very wide frequency range covering several orders of magnitude. Such kind of behavior is standard for ideal elastic materials, the elastic modulus of which must be independent of frequency. Hence, the filled lyotropic composites can be classified as elastic materials. However, G'' exhibits a definite minimum at intermediate frequency [120], and the yielding behavior is not observed clearly. This can be due to the critical frequency beyond which yielding occurs being outside the experimentally measured frequency window.

Tan δ values for different volume fractions of lyotropic composites at strain value, $\gamma = 6\%$, is shown in Figure: 6.9. Tan δ values for different concentration composites can be collapsed into one master curve, as shown in dark-purple; this behavior could be replicated at all values of applied strain in the yielding region. Thus, it was concluded the value of tan δ is not dependent on the filler concentration beyond $\phi = \phi_c \geq 0.2$ for the lyotropic nematic composites, $\phi_c \sim 0.2$ is the onset of stable gel formation. However, the plot of tan δ is non-linear, with a negative slope of $\sim$ -0.11 at low frequency, $\omega \leq 10$ rad/s, suggesting a strong glassy behavior. But on increasing the frequency the value increases, finally becoming greater than 1 at $\omega > 100$ rad/s. The dynamic independence suggests that the nematic phase determines the elastic and viscous properties of the composite, and its interaction with the colloids does not alter as the volume fraction is increased. Like the case for filled thermotropic nematics, colloids give rise to disclinations, and the volume fraction increases the density of disclinations in the system, thus

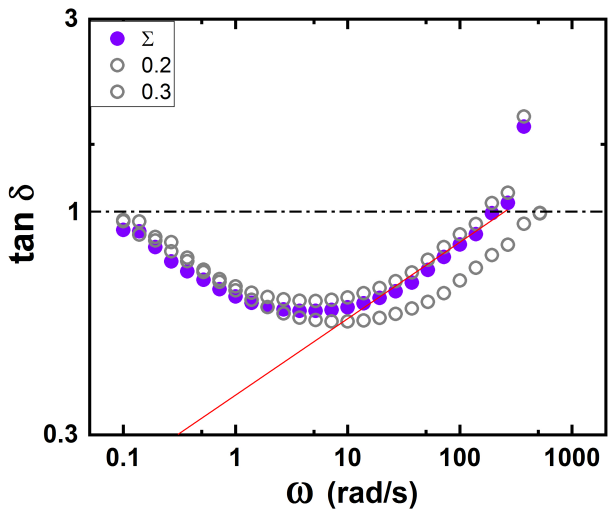

Figure 6.9 *Tan $\delta = G''/G'$ as a function of angular frequency ω in rad/s for different volume fractions, ϕ, of PMMA in NC1 at $\gamma = 6\%$, Dark purple shows a collapsed master curve calculated from average of both the volume fractions. Line has a slope of 1/2.*

increasing the strength of the composites.

Tan δ values at different strain values, $\gamma = 6$, 8 and 10 %, for $\phi = 0.3$ lyotropic composites are drawn in Figure: 6.10. The value of tan δ is directly proportional to strain, with the values being maximum at 10% strain. Tan δ becomes greater than 1 at higher frequencies, $\omega > 100$ rad/s, where the nematic micelles have oriented themselves in the direction of flow. However, the minima of tan δ for all three strains occurs at, $\omega = 10$ rad/s. The fluid-like behavior (tan $\delta > 1$) may be present at strain values greater than 10%. It can be clearly seen that the cross-over ($G' = G'' \rightarrow \tan \delta = 1$) decreases with increasing strain. We were not able to plot the critical frequency as a function of strain because of few data points available.

6.2.3 Comparison of filled lyotropic and thermotropic composites - experiment and theory

Oscillatory strain sweep comparison

The strain amplitude sweep (Figure: 6.11) showed similar behavior for filled both thermotropic and nematic composites. However, the yield strain for lyotropic

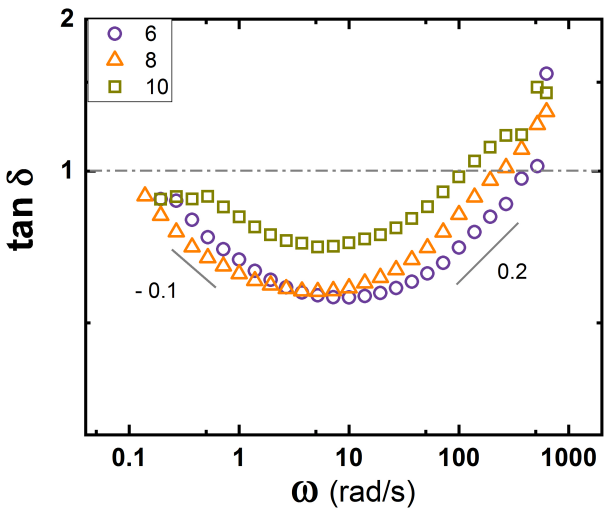

Figure 6.10 *Tan δ as a function of angular frequency ω in rad/s for γ% ≥ 6% for φ = 0.3 PMMA in NC1 NLCs.*

composites was one order of magnitude greater. From the theory discussed in the previous chapter, Equation: 5.2 and 5.3 were used to draw the theoretical prediction of G' and G'' for lyotropic nematics. The value of rotational viscosity and Leslie co-efficient is not known for NC1 LCs; thus, the values were kept the same as 5CB as γ_r = 0.081 Pa.s and α_2 = -0.939 Pa.s. However, the radius of disclination was increased by one order of magnitude to 60 nm, because of the size of nematic micelles is $\sim$ 60 nm [187]. The value of critical strain is higher for lyotropic nematic because of its direct dependence on disclination core radius, $\gamma_c = \frac{r_c}{1.1D}$ where r_c is the radius of a disclination.

The value of the maximum (in the LVR) dynamic moduli for both the composites were compared, see Figure: 6.12. At a higher concentration at $\phi \geq 0.2$ there was a sharp increment in the value of G' and G''. In spite of forming similar microstructures arrested by Saturn-ring defects, the value of G' of 5CB composite is one order of magnitude greater than G' of NC1 composite. Thus, the director distortion around a single particle in both the composites was calculated. The colloidal forces in nematic LCs are much stronger than the forces in ordinary colloids in isotropic solvents, exceeding thousands of k_BT per PMMA-PHSA particle, see Figure: 2.11 [89]. The extent of these defect lines or the deformation in the presence of colloids in LCs is determined by the anchoring strength. This is further estimated by taking the radial profile of these defect lines at 0° and 45° along the particle diameter. Figure: 6.13 (a) shows the radial profile of

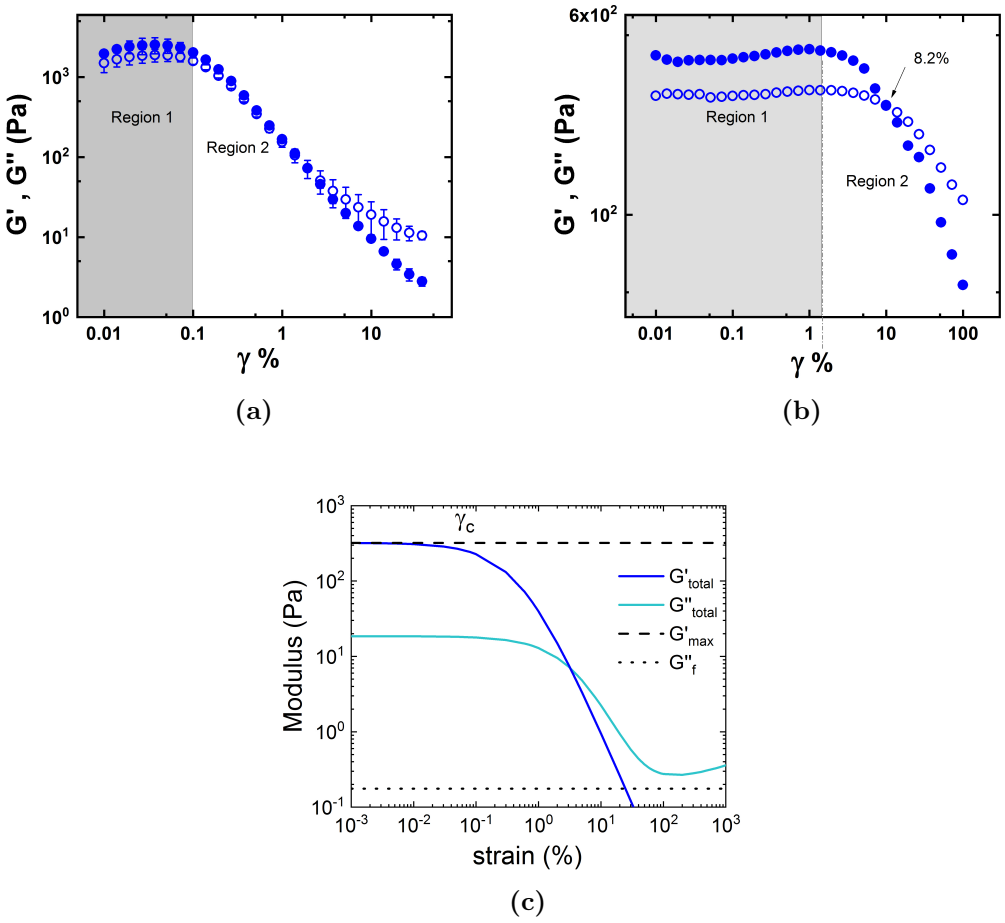

Figure 6.11 *The mechanical spectrum of G' and G'' as a function strain for (a) PMMA-PHSA in 5CB composites (thermotropic) and (b) PMMA-PVP in NC1 composites (lyotropic). Both the composites show LVR (region 1) and yielding (region 2), (c) The plot for G' and G'' predicted from theory.*

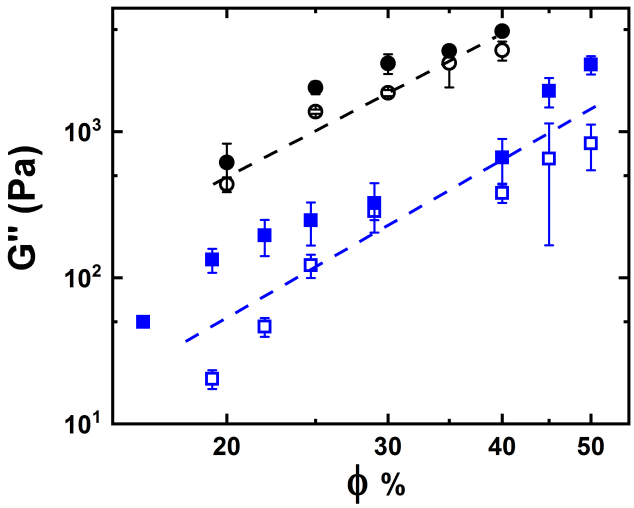

Figure 6.12 *Comparison of moduli of filled lyotropic composite (square) with thermotropic composites (circle). Line is a guide to eye. Closed symbol represents G' and open symbol represents G''.*

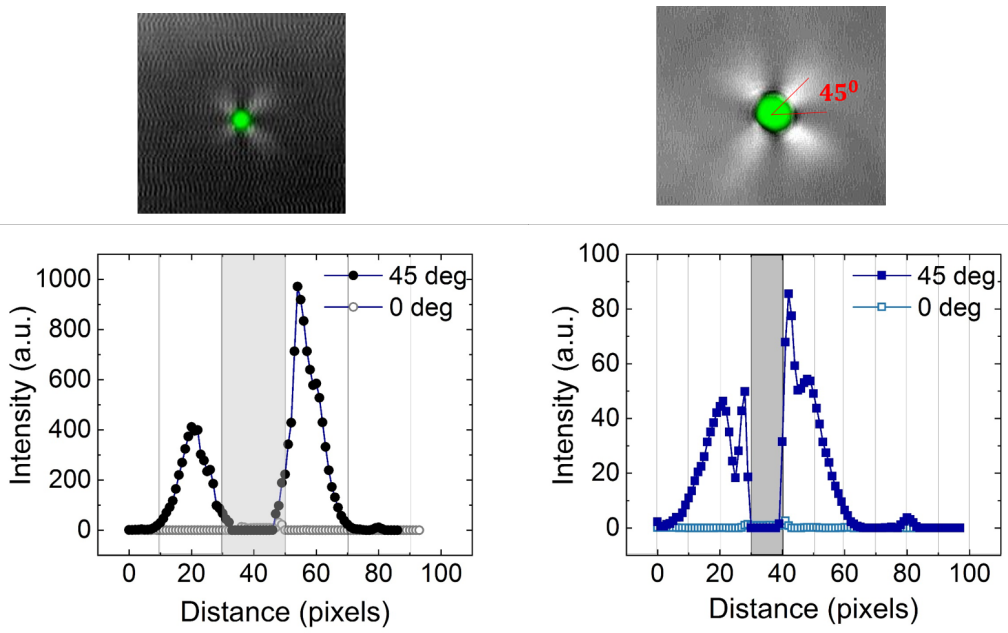

(a) **(b)**

Figure 6.13 *Confocal micrograph of (a) single PMMA-PHSA particles dispersed in 5CB and radial profile of the director distortion, (b) single PMMA-PVP particles dispersed in NC1 and radial profile of the director distortion.*

PMMA-PHSA in 5CB and (b) for PMMA in NC1. In both lyotropic (NC1) and thermotropic (5CB) nematics, PMMA particles induce Saturn-ring defect but the extent of director distortion is up to three times the colloidal diameter for 5CB LCs and up to two times the colloidal diameter in NC1 LCs. The extent of the director distortion is not so different between both the composites, but the result indeed suggests a weaker anchoring strength between colloids in lyotropic nematics as compared to thermotropics.

Frequency sweep comparison

The dynamic behavior of both the thermotropic and lyotropic composites have been compared in Figure 6.14. Both the nematic LCs show Maxwell fluid-like behavior with G'' linearly increasing with ω. The storage modulus of the filled thermotropic (left) and lyotropic (right) remain constant with no dependence on the frequency. This is a characteristic of an elastic material. However, a dramatic yielding is observed for thermotropic composites with $G'' > G'$ beyond a critical frequency; this behavior is not seen in the lyotropic composites. One of the plausible explanation is that the critical frequency for lyotropic composites is beyond the range of applied frequency. This is further explained by the dependence of critical frequency on the disclination radius, $\omega_c = \frac{2\pi K\gamma_c}{a^2\gamma_r(\gamma_c+\gamma)} = \frac{2\pi Kr_c}{Da^2\gamma_r((r_c/D)+\gamma)}$ thus indicating that ω_c increases when the disclination radius (or yield strain) increases. The disclination core radius for lyotropic NC1 LCs is one order of magnitude greater than the thermotropic 5CB counterpart. Therefore, we do not see the upturn in the viscous component for lyotropic nematic phases where the disclination radius (r_c) is expected to be tenfold of the disclination radius in thermotropic nematic materials. Using the Equation: 5.4 and 5.7 and putting the relevant value of r_c, the theoretical plot for frequency dependence of the moduli is created in Figure: 6.14 c.

6.2.4 Effect of droplet deformability on the rheology of nematic composites.

After studying the physics of solid-sphere colloids in NC1 LCs, we were encouraged to study the effect of droplet deformability on the rheology of nematic emulsions. The nematic emulsions were made using PDMS (0.05 Pa.s). Readers are directed to section 4.2.1 for the protocol followed to form the nematic

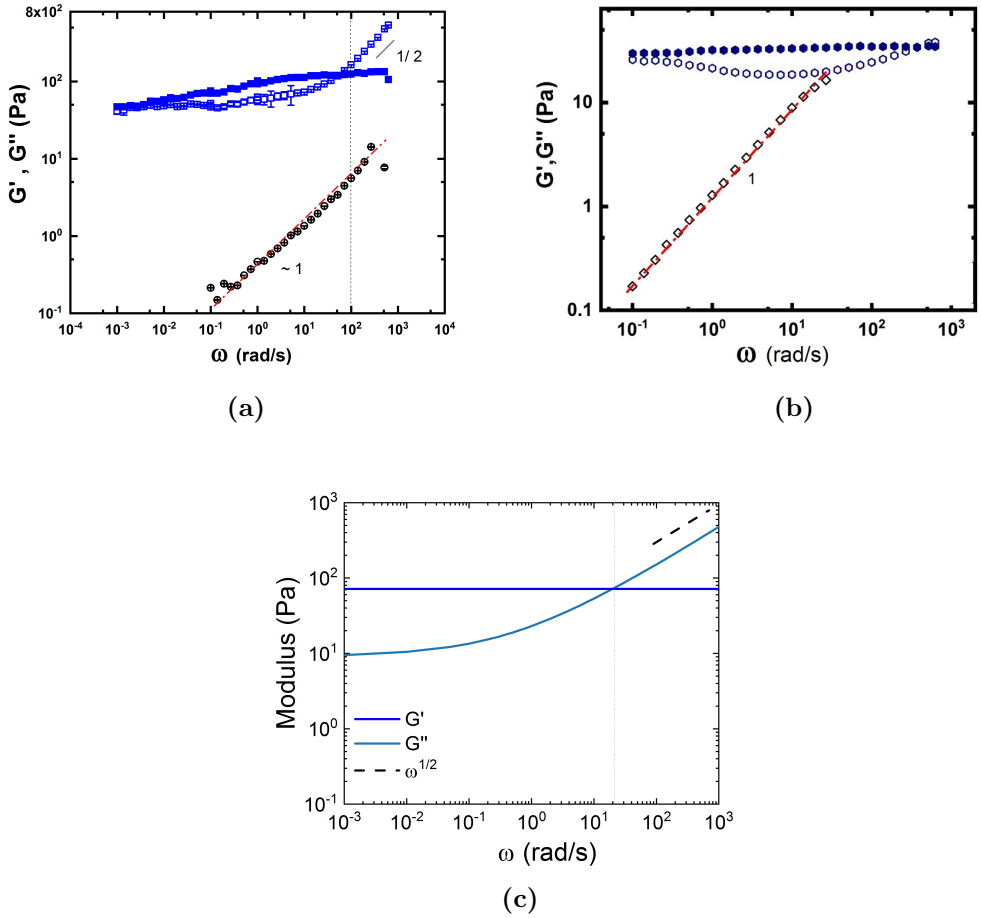

Figure 6.14 *The mechanical spectrum of G' and G'' as a function of angular frequency for (a) $\phi = 0.3$ of PMMA in 5CB NLCs (blue) as compared to $\phi = 0.05$ of PMMA in 5CB NLCs (black) at 6% strain and (b) $\phi = 0.3$ of PMMA in NC1 NLCs (blue) as compared to NC1 NLCs (black) at $\gamma = 6\%$. G' is in closed symbol and G'' in open symbol. For both the pure NLCs, $G'' \propto \omega$. However, for both the filled composites the value of storage moduli, G', remains constant for the entire frequency range, but there is a gentle yielding observed for the composites beyond a critical frequency where $G'' \propto \omega^{1/2}$, (c) frequency sweep for lyotropic composites predicted from theory.*

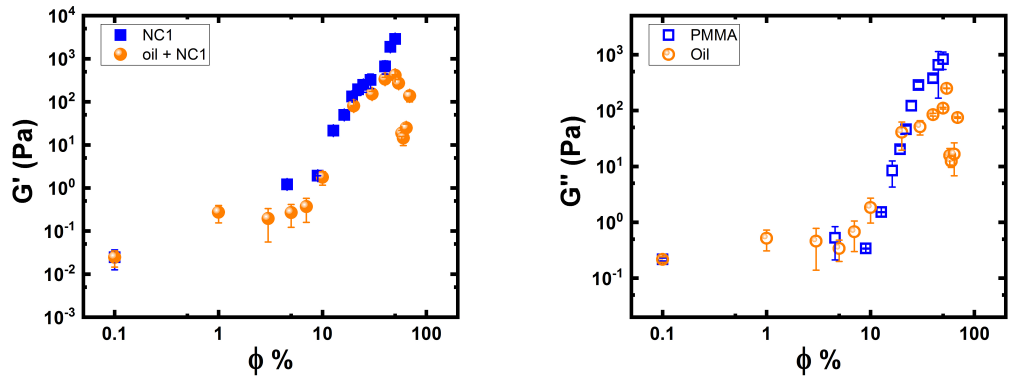

(a) (b)

Figure 6.15 *The evolution of (a) G' and (b) G'' as a function of volume fraction for 0.05Pa.s PDMS nematic emulsion. The nematic emulsions follow solid-sphere rheology up to $\phi < 0.54$ but shows a decrease in the value of moduli beyond $\phi = 0.54$.*

emulsion. The average droplet size of the PDMS droplets were, 2r = 4.54 ± 1.23 μm. Nematic emulsions up to volume fraction, $\phi = 0.72$ were made. The resultant moduli of the strain amplitude sweep of these emulsion as a function of ϕ is plotted in Figure: 6.15. The plot suggests that nematic emulsion has the same value of dynamic moduli as PMMA composite up to $\phi < 0.54$ beyond which the value of the moduli decreases. This behavior is replicated in the loss moduli curve as well. The flow rheology of PDMS emulsions in an isotropic solvent has been studied by Saiki and group [171]; they observed that both PDMS emulsion showed identical behavior as hard-sphere for low concentration, $\phi \leq 0.4$ but deviates from Krieger-Dougherty fit at $\phi_g = 0.58$. The deviation was due to the droplet deformability. However, for our nematic emulsions the deviation occurs at $\phi = 0.54$. At $\phi = 0.54$, we expect the interparticle separation $r/d \sim (0.64/0.58)^{1/3} \sim 1.03$ (presuming colloids touch at random close packing $\phi = 0.64$) which is less than the ratio of particle radius to the interparticle distance, $r/d \sim 1.1$, between colloids entangled by disclinations, as reported through computer simulations by Araki *et al.* [10], thus the droplets start touching and coalesce changing the size of droplets changing the rheological behavior.

6.3 Effect of surface charge on the structure and rheology of filled lyotropic nematics

We were inspired to explore the effect of surface charge on the rheology of filled lyotropic composites after studying the viscoelasticity of uncharged composites. Competition between charge repulsion and colloidal attraction is ubiquitous across colloidal dispersions. Charge effects can enhance phase separation in charged colloid-polymer systems [146] and are predicted for charged lyotropic lamellar systems [38]. It is known that the charged colloids aggregate in a lyotropic nematic phase. The first experimental evidence for the existence of elastic forces between spherical inclusions in a nematic liquid crystal was given for small-angle neutron scattering (SANS) experiments on a lyotropic nematic crystal by Raghunathan *et al.* They showed that the charged colloids aggregate in the presence of lyotropic nematics [98]. To know the effect of surface charge of colloids on the microstructure and viscoelastic property of a filled NC1 system, we have identified both positive and negatively charged polystyrene (PS) particles. Composites of negative and positively charged polystyrene particles were made by dispersing them in NC1 LCs for different volume fractions following the same preparation method as uncharged PMMA composites. Table 4.2 gives details about the zeta potential, (ξ), and the surface charge, (σ), of both Ani PS and Cat PS.

Confocal micrographs at $\phi = 0.25$ for both uncharged (PMMA-PVP in NC1) composite and negatively charged (Ani PS in NC1) composite are shown in Figure: 6.16. Uncharged PMMA particles form a space spanning network-like structure in NC1 LCs whereas the Ani PS form tenuous compact clusters not interlinked with each other. To observe the detailed difference in the microstructure, higher magnification images were studied. Figure: 6.17 shows the confocal micrographs of these two systems under high magnification (63X) for $\phi = 0.15$ composites, there are some striking differences between charged and uncharged system. PMMA-PVP particles formed irregularly shaped clusters connected over the space, whereas the negatively charged system of Ani PS showed a 2D lattice-like structure. Similar structures were first observed by placing quadrupolar colloids near to each other in thermotropic nematics with the help of laser tweezers [89]. In our system, for the first time, these honeycomb structures are observed in bulk, with dark defect lines connecting each other. This indicates that the Saturn-ring defects around the particles do become entangled

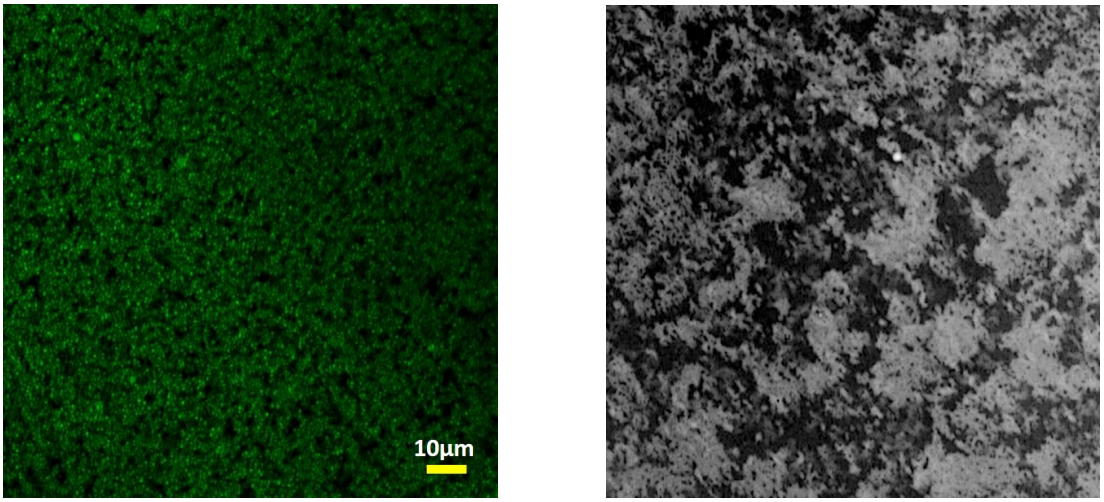

(a) (b)

Figure 6.16 *(a) Tenuous network of PMMA clusters in NC1 LCs as seen under confocal microscope, (b) Compact clusters of Ani PS particles in NC1. (dark region represents LCs media whereas white region represents particles).*

but form different topological structures compared to the uncharged system. It was difficult to image entangled defect in lyotropic system because of the alignment constraint.

6.3.1 Oscillatory strain sweep

Figure: 6.18 (a) shows a plot of $G'(\max)$ and $G''(\max)$ as a function of ϕ for Anionic PS particles in NC1. The inset graph shows that there are again two different regions at low and high volume fractions. At high ϕ, G' increases as ϕ^2. A detailed plot with the value of G' and G'' for charged and uncharged composites in both lyotropic and thermotropic composite is shown in the Figure: 6.19. The magnitude of G' for Cat PS and uncharged PMMA composites are of the same order of magnitude. However, G' of Ani PS composites are one order of magnitude lower at the same volume fraction, ϕ.

The lower magnitude of G' for Ani PS composites was further studied with the help of confocal images. On preliminary examination, both the colloids appear to promote quadrupolar defect patterns. However, there is a clear difference in the microstructure of both charged and uncharged composites, see Figure: 6.16. This could be due to different anchoring conditions between the colloids and LCs medium. The strength and type of anchoring depend upon the surface charge and

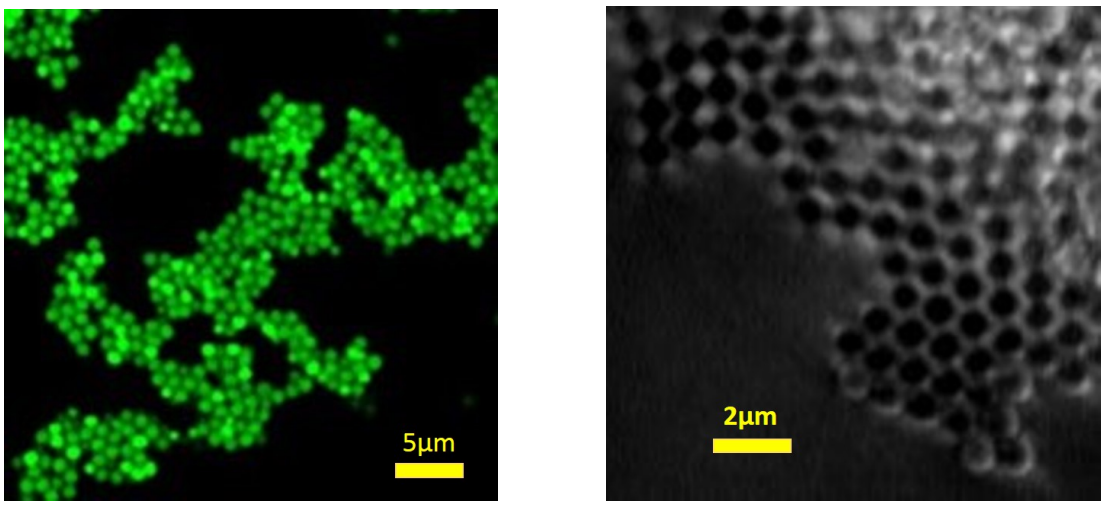

(a) (b)

Figure 6.17 *(a) Irregular shaped network like cluster of PMMA particles in NC1 LCs (dark regions represents LCs media whereas green circles represents PMMA particles), (b) Compact clusters forming 2D lattice like array of Ani PS particles in NC1. (dark region represents Ani PS particles whereas dark lines shows the disclinations around the particles.*

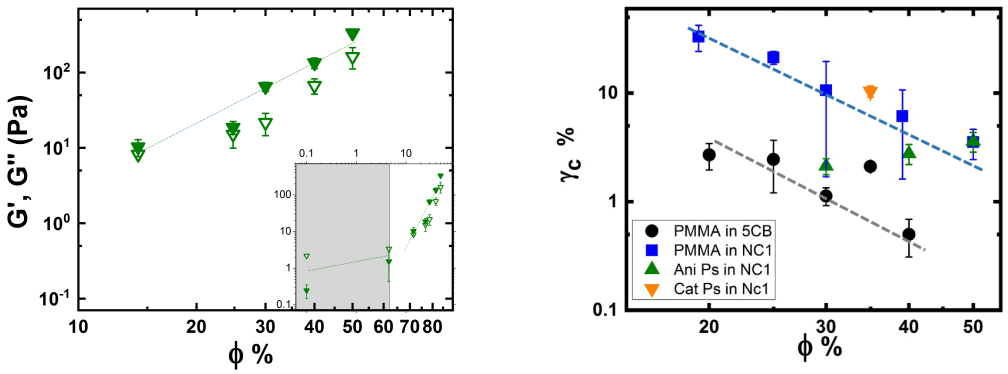

(a) (b)

Figure 6.18 *(a) Evolution of G' and G'' as a function of ϕ for negatively charged nematic composites, inset shows the two regime for dynamic moduli, (b) The value of critical strain, γ_c comparison as a function of volume fraction for uncharged thermotropic (black) and lyotropic (blue) composites, negatively charged (green) and positively charged (orange) composites. Line is a guide to the eye.*

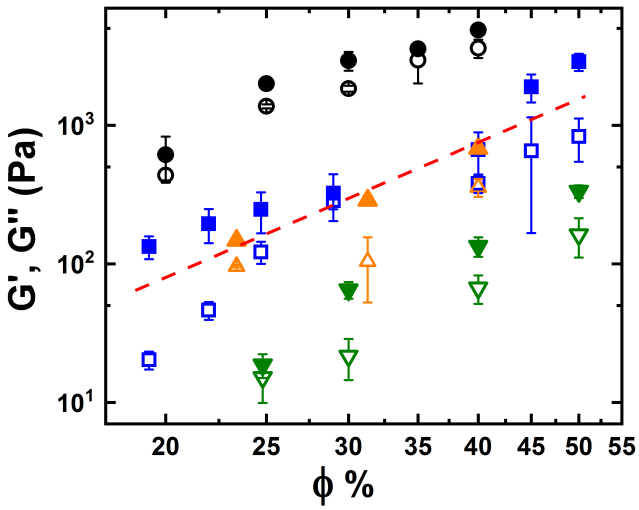

Figure 6.19 *Storage modulus (G') and loss modulus (G'') as a function of ($\phi \geq 0.2$) of uncharged and charged colloids in nematic liquid crystal composite, black = PMMA-PHSA in 5CB, blue = PMMA in NC1, green = anionic polystyrene in NC1 and orange = Cationic Polystyrene in NC1.*

the defect structure around particles in LCs. Thus, we tried to image individual PMMA and Ani PS and have tried to evaluate the extent of directory distortion caused by both the particles in NC1 medium. Each colloid is 1 micron in diameter, so visualization of nematic distortion was not easy.

Figure: 6.20 shows the director distortion profile for both PMMA-PVP and Ani PS in NC1. Profiles were taken across the particle centers to measure the extent of the spread of the quadrupolar defect pattern for each colloid. The spread is up to 2 colloid diameters beyond the colloid perimeter for the uncharged PMMA sample but is less than one diameter beyond the perimeter of the negatively charged anionic sample. It seems we have very weak anchoring conditions for the anionic sample, although it does appear to be homeotropic. So from the extent of distortion of the director, we conclude that the negatively charged Ani PS particles induce very weak homeotropic anchoring in nematic solution as compared to the uncharged system. Thus, they form a weak gel-like network leading to a lower value of G' as compared to the uncharged system. PMMA particles are sterically stabilized by PVP polymers that form hair-like structures around them (Figure: 4.1), whereas Ani PS particles have a smooth surface and are stabilized by the charge. These hair-like structures around PMMA particles promote strong homeotropic anchoring when in the nematic medium [66], whereas

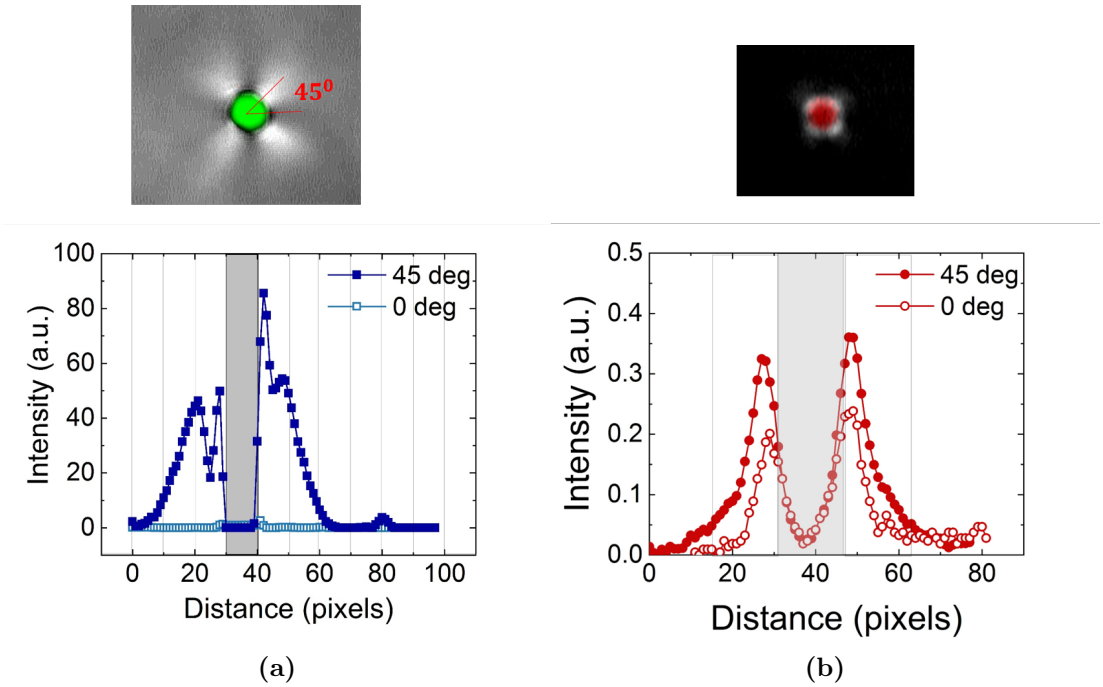

(a) (b)

Figure 6.20 *A comparison of extent of director distortion for (a) PMMA-PVP in NC1 as compared to (b) Ani PS in NC1. Profiles were taken across the particle centers to measure the extent of the spread of the quadrupolar defect pattern for each colloid. The spread is up to 2 colloid diameters beyond the colloid perimeter for the uncharged PMMA sample but is less than one diameter beyond the perimeter of the negatively charged anionic sample.*

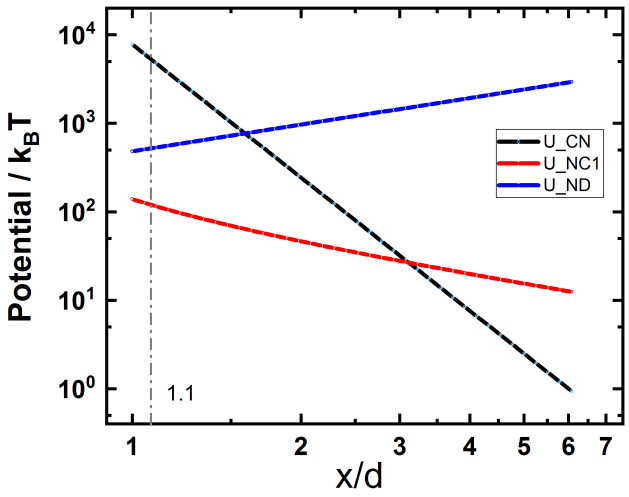

Figure 6.21 *Comparison of different potentials in ratio with thermal energy (k_BT) between colloids and LCs composites, x is the separation between particles and D is the colloidal diameter. U_{CN} (square) is the attraction potential between colloids and nematic LCs, U_{ND} (triangle) elastic attraction potential between nematic domains and U_{NC1} (circle) is the screened Coulomb potential between nematic micelles.*

a smoother surface may induce a weaker homeotropic anchoring compared to the hairy surface. The mechanical strength of these array-like structures is one order of magnitude less than the uncharged clusters.

It was also observed that the moduli value for uncharged lyotropic composites were one order of magnitude lower than their thermotropic part inspite of both particles and LCs phases being similar, see Figure: 6.19. Thus, to understand the discrepancy in the magnitude of G' for uncharged and charged lyotropic composites, we calculated and compared the different forces binding the colloid and liquid crystal composites together. The attraction potential between (a) colloids and nematic domains and (b) between nematic domains were present in both thermotropic and lyotropic LCs. The attractive potential between colloids and nematic LCs, U_{CN}, [94, 167] can be written in the form of anchoring strength, W, and elasticity of NLCs, K; where r_0 is the colloid radius and x is the separation between particles. The attraction potential between colloids and the nematic host is higher for strongly anchored particles because of $U_{CN} \propto \omega^2$. At T = 300 K and particle separation *(x) = 1.1D,* the value of $U_{CN} \sim 3000\ k_BT$.

$$U_{CN} = \left(\frac{4\pi W^2 r_0^8}{K x^5} (1 - \frac{W r_0}{56K}) \right) \tag{6.2}$$

The elastic attraction potential among nematic domains, U_{ND}, can be estimated from Hooke's law, see Equation: 6.3, where n is the number of nematic monodomains, K is the elastic constant and A is the nematic domain size.

$$U_{ND} = n * K * x \sim 5000 k_B T \tag{6.3}$$

$$U_{NC1} = \left(\frac{k(q_1 q_2)^2}{(x - r)} \exp^{-r/\lambda_D} \right) \sim 10000 k_B T \tag{6.4}$$

However, in addition to these forces, there is an additional force between the negatively charged micelles in lyotropic nematic LCs. The lyotropic NC1 LCs are composed of negatively charged micelles because of their composition (24.8% of anionic surfactant -SDS). The screened Coulomb potential between the negatively charged micelles, U_{NC1} is given by Equation: 6.4, where q_1 is the electronic charge = 1.6 10^{-19}C, q_2 is the surface charge on the rod-like micelles in NC1, x is the particle separation and r is the particle radius and D = 2r is particle diameter and λ_D is the Debye length. The range of all these three forces over the particle separation is plotted in the Figure: 6.21. From the plot, it is observed, the value of screened Coulomb potential dominates at low particle separation, compared to the long-range nematic attraction. The occurrence of Saturn-ring defect happens at $\frac{x}{D} \sim 1.1$ [10], which is according to the plot in the range where the screened Coulomb repulsion dominates, thus reducing the combined interaction potential between colloids and LCs — thus decreasing the anchoring strength between the colloids and lyotropic nematics and in turn, reducing the magnitude of G'.

In negatively charged lyotropic composites, the value of G' is one order of magnitude lower than the uncharged lyotropic composites. One of the mechanisms explaining this weak anchoring in the anionic composite is charged induced repulsion. The lyotropic nematic (NC1) phase have rod-like micelles that are negatively charged because of anionic SDS present in them. Coulomb repulsion between Anionic PS beads and could occur between Ani PS and charged micelles of NC1 LCs. However, if we go down to the nanoscale, the micellar solution is likely to be polydisperse with micelles of varying anisotropy from

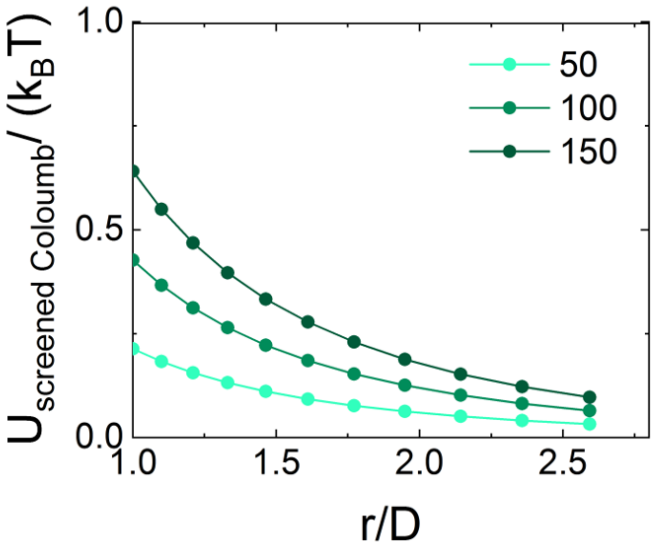

Figure 6.22 *Curve comparing the screened Coulomb potential between charged colloids and polydispersed charged SDS micelles with thermal energy ($k_B T$)*

spherical to cylindrical. In the nematic liquid crystal, the aspect ratio of the building blocks molecules in this case of the micelles are of 3:1. Micelles with higher anisotropy will have more SDS present in the rod-like structure (see Figure: 4.5, giving rise to higher surface charge on them.

Considering the micelles next to a charged surface and the local charge repulsion between an area on the colloid equivalent to the micelle radius, we can use the screened Coulomb potential (Equation: 6.4) to calculate the repulsion between the colloid surface and micelles of increasing charge. Spherical micelles of SDS are known to carry around 50 charges [94], and these charges increase with the micelles becoming more anisotropic on the addition of SDS. In the nematic phase, the uniaxial micelles tend to be three times as long as wide on average (aspect ratio 3:1 [149]). So we have calculated the potentials of these micelles as compared to the thermal energy (k_BT), see Figure: 6.22 for three different surface charges 50 q, 100q and 150q. The calculated potentials are close to thermal energy (k_BT), which suggests that larger (longer) micelles can be repelled from the colloid surface, thus reducing the anchoring of the nematic to the colloid surface. So, the weak anchoring is caused by electrostatic repulsion of larger micelles from the negatively charges polystyrene surface and as a result, lowering the value of G' for Ani PS composite. A schematic representation of the orientation of micelles before and after getting repelled from anionic PS is shown in the Figure: 6.23.

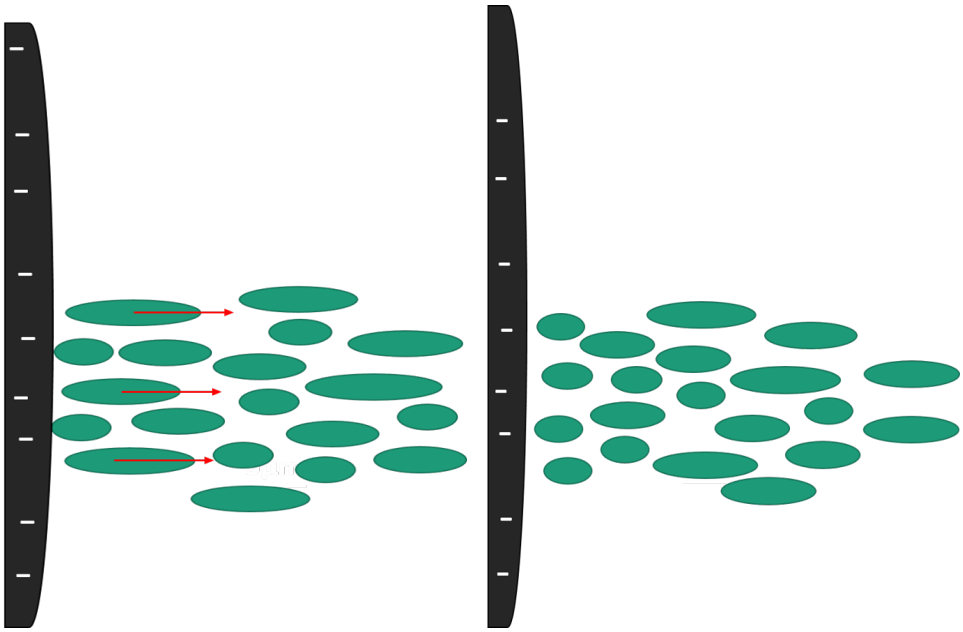

Figure 6.23 *(a) Schematic of polydispersed micelles (green) and negatively charged particle (black), (b) Oblate micelles having more SDS at its head rearranges themselves after getting repelled from negatively charged particle.*

6.3.2 Dynamic response in the yielding region

Frequency spectra in the yielding regime, region - 2, (Figure: 6.24 b) of Ani PS composite in NC1 suggest that at low frequency both G' and G'' increase with frequency. But after a critical frequency, the composites yields with G'' $> G'$, in this region G'' grows as $\omega^{1/2}$. The viscous response is similar to the uncharged composites. However, G' is not constant but shows a mild dependence on frequency. This is because the Ani PS particles form a fragile array of particles in NC1 LCs exhibiting low elasticity. And at a higher frequency, the microstructure breaks and aligns in the direction of flow, giving rise to a higher value of G''. The plot of tanδ for strain values, $\gamma \geq 0.6$ is shown in Figure: 6.25. Tan δ curve is non-linear with a constant value at a lower frequency, however at a critical frequency, the viscous behavior dominates and tan δ grows as $\omega^{1/2}$, see Figure: 6.25. It can be clearly seen that the value of critical frequency is inversely proportional to strain, but due to an insufficient number of data points, the inverse linear relation is not plotted. Thus the dynamic behavior of charged nematic composite is similar to uncharged composite at a higher frequency, with $G'' \propto \omega^{1/2}$.

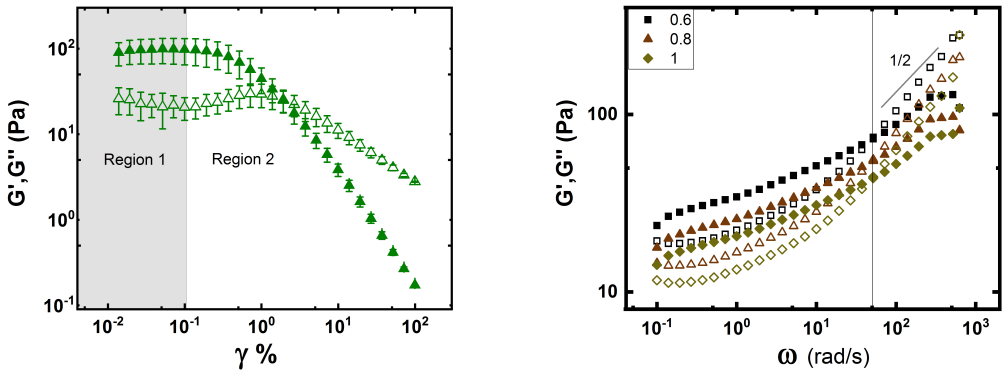

(a) (b)

Figure 6.24 *(a) Amplitude sweep of $\phi = 0.3$ of Ani PS in NC1, showing LVR rehion and yielding region as region 1 and 2, (b) Frequency spectra of Ani PS composite at strain values, $\gamma \geq 0.6\%$.*

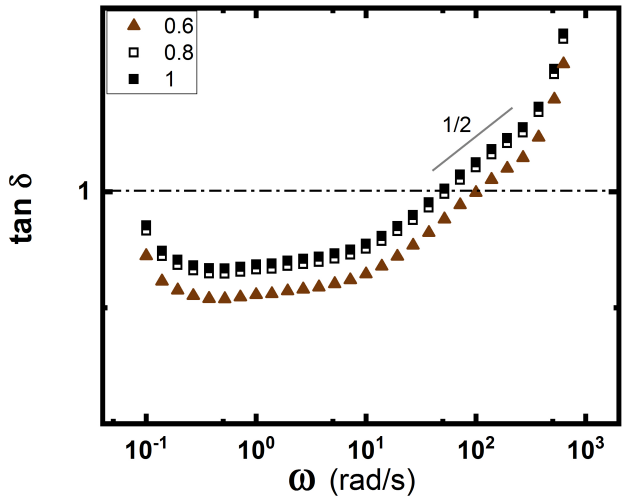

Figure 6.25 *Tan δ curve for Ani PS composite in the yielding region, $\gamma \geq 0.6\%$. Tan $\delta \propto \omega^{1/2}$ at frequency greater than the critical frequency, $\omega_c = G''/G'$.*

6.4 Summary

One of the most important findings of this thesis concerns the measurement of dynamic rheology and the microstructure of filled lyotropic nematic composite and comparing it with the filled thermotropic system. And here, some of the important experimental findings are presented:

- Filled lyotropic nematic composites behave the same as filled thermotropic, exhibiting the same dynamic behavior and forming similar microstructure.
- Surface charge of colloids disrupts the composite properties in the charged micellar nematic liquid crystal system.
- Nematic emulsions show similar rheological behavior like the solid-sphere dispersion in lyotropic nematic up to $\phi \leq 0.54$ but deviate near the glass transition volume fraction.

Chapter 7

Flow behavior of filled nematics.

The rheological properties of concentrated suspensions in liquid crystals are of interest in several applications. The making, mixing, and transfer of such materials generally require knowledge of the possible variation of viscosity with shearing rates as well as with concentration and particle size distribution. Here, in this work, we perform steady-state flow rheology on the samples prepared by mixing colloids in nematic LCs, both thermotropic and lyotropic. First, we discuss the viscosity and flow curve of a hard-sphere colloidal suspension followed by nematic emulsion. Nematic emulsions were made by dispersing PDMS in NC1 LCs. We have used two viscosities PDMS; (a) 0.05 Pa.s and (b) 0.5 Pa.s for these measurements. However, they are composed of very small droplets ($\sim 4\mu$m in diameter) and are very much like our solid-sphere system since the drops are hardly deformable. As a result, they follow essentially the same kind of rules given for solid dispersions.

The same experimental conditions were used to perform steady-state flow rheology on our composites. Apparent viscosity was measured when the material has reached steady-state flow determined by the correct sample period. The sample period is the time interval for which the average value of torque is recorded. The shear rate was increased (logarithmically) in steps from (a) 0.001 to 0.01 /s, (b) 0.01 to 0.1 /s, (c) 0.1 to 1/s, and (d) 1 to 1000/s and the process was repeated yielding a viscosity and flow curve. The steady-state stress as a function of applied shear rate is referred to as the flow curve, whereas the viscosity as a function of applied shear rate is referred to as the viscosity curve.

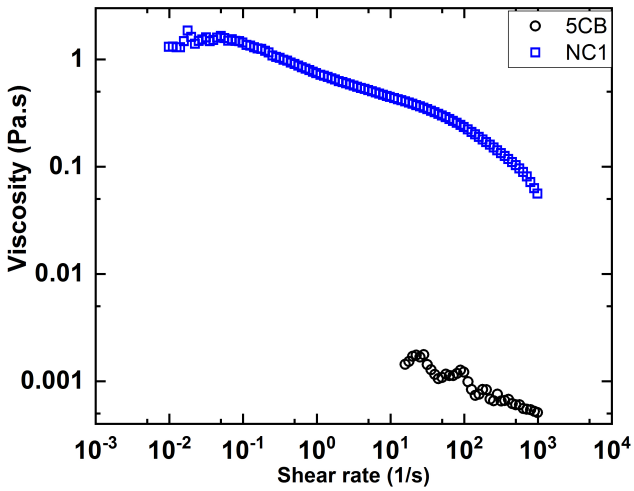

Figure 7.1 *Steady state shear viscosity curve as a function of shear rate, $\dot{\gamma}$, for 5CB (black) and pure NC1 LCs (blue).*

7.1 Nematic liquid crystals (LCs)

The viscosity curve for both thermotropic - 5CB and lyotropic nematic NC1 LCs is drawn in the Figure: 7.1. Both the nematic LCs exhibit mild shear-thinning behavior, with a rate - 0.16 ± 0.01 for 5CB and - 0.32 ± 0.01 for NC1 LCs. Nematic liquids generally show shear-thinning property [130, 185]. The perturbation of the equilibrium state by flow is then dependent not only on the direction of the flow field relative to the director field, $n(\vec{r})$, but also on the relative configuration of the flow gradient and the director field. The shear-thinning behavior in the NC1 phase can be due to the orientation of cylindrical micelles to facilitate flow. The curve was fitted to a power-law equation (Equation: 3.19). The value of power-law index, n_{PL}, is 0.74 ± 0.15 for 5CB and 0.68 ± 0.13 for NC1. The difference in the value suggests that the lyotropic nematic (NC1) LCs exhibit a high shear-thinning behavior compared to thermotropic nematic 5CB LCs.

7.2 Influence of filler

For the first time, we have studied the flow rheology of the filled thermotropic and lyotropic composites. The PMMA filled composites were subjected to shear

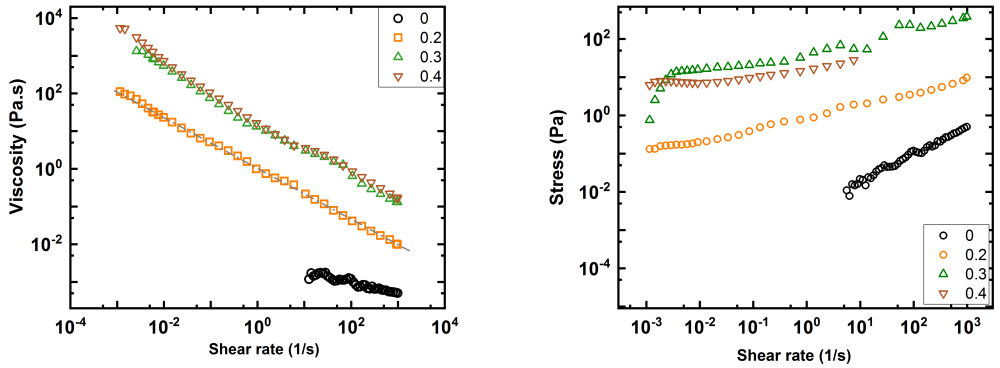

(a) (b)

Figure 7.2 *(a) Shear viscosity in (η) Pa.s and (b) Stress curve for PMMA-PHSA in 5CB and composite plotted against shear rate, for various volume fractions: $0.05 \leq \phi \leq 0.5$. Shear-thinning behavior and the absence of low shear-rate Newtonian plateau is clearly observed.*

stress, and the resultant change in viscosity is reported. Figure: 7.2 represents the viscosity curve and stress curve for PMMA in 5CB composites and Figure: 7.3 represents the flow curve of PMMA in NC1 composites.

The steady-state flow curve of solid-sphere colloids in nematic LCs show shear-thinning behavior without the existence of zero-shear viscosity plateau but it may appear at low enough shear-rate which is outside the range of experimentally measured shear-rate. The exceptional shear-thinning behavior occurs as a result of micro structural rearrangements occurring aligned to the plane of applied shear. Raghavan and Khan [16, 156] have proposed that highly concentrated suspension may form ordered layers and clusters of particles under a high shear rate in the direction of flow. Pure 5CB LCs and dilute composites, $\phi \leq 0.05$, show mild shear-thinning behavior with a slope of - 0.16 $\pm$ 0.01. However, the concentrated composites, $\phi \geq 0.2$, show strong shear-thinning behavior with a slope of -0.73 $\pm$ 0.11. This rate is higher when compared with dense colloidal suspensions [34, 171] and filled polymer solution [172], [154], [74], [153]. The low shear - viscosity $\dot{\gamma} \rightarrow 0.01$/s increases with increasing filler concentration. The interaction among Saturn-ring defects around the particles at equilibrium explains the increase in low - shear viscosity with the filler concentration for both the composites. Beyond a certain critical concentration, $\phi \geq 0.2$, these defects entangle to form a network-like structure that acts as a node restricting the motion of the particles in the composites hence resisting flow. However, upon shearing, the topological configuration frustrates, and the defect encircled particle

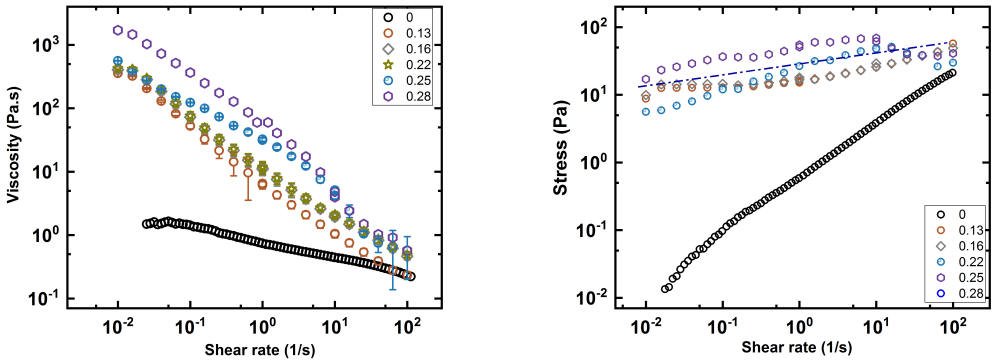

(a) (b)

Figure 7.3 *(a) Shear viscosity in (η) Pa.s and (b) Stress curve of PMMA-PVP in NC1 composite plotted against shear rate, for various volume fractions: $0.05 \leq \phi \leq 0.5$. Shear-thinning behavior and the absence of low shear-rate Newtonian plateau is clearly observed. Blue line depicts all the composites have similar increase.*

network breaks into smaller clusters and began to align along with the flow. In dense nematic composites, the defect does not detangle, but their structure breaks, unlike polymer melts. This behavior was studied using microfluidic channel flow. A channel slide with width: 20 μm, depth: 20 μm and length: 58.5 mm was used to image the lyotropic nematics. The elve-flow OB1 pressure controller was used to control the flow speed of the sample through the channel. And the flow profile was imaged under a confocal microscope. Figure: 7.4 show the images of dilute lyotropic composite in the microfluidic channel. The first image shows that the PMMA particles are trapped on the side walls restricting their motion. However, the maximum flow velocity is at the centre and the entangled network breaks into smaller clusters aligning along the flow direction. A simulation of velocity profile in the entangled network shows an enhanced flow velocity in a defect network.

At high shear-rate, the effect of adding particles becomes less significant, and eventually, each of the curves becomes parallel to each other, showing power-law behavior. For $\dot{\gamma} > 100$/s, the viscosity for different filler concentration converge to a common viscosity.

In lyotropic nematic composites, the micellar structure, when in equilibrium, has a high value of G', G'' and low shear viscosity, which is similar to a high molecular weight concentrated solution of polymers [153]. However, upon shearing, they can break into smaller micelles and align in the shear direction. The viscosity

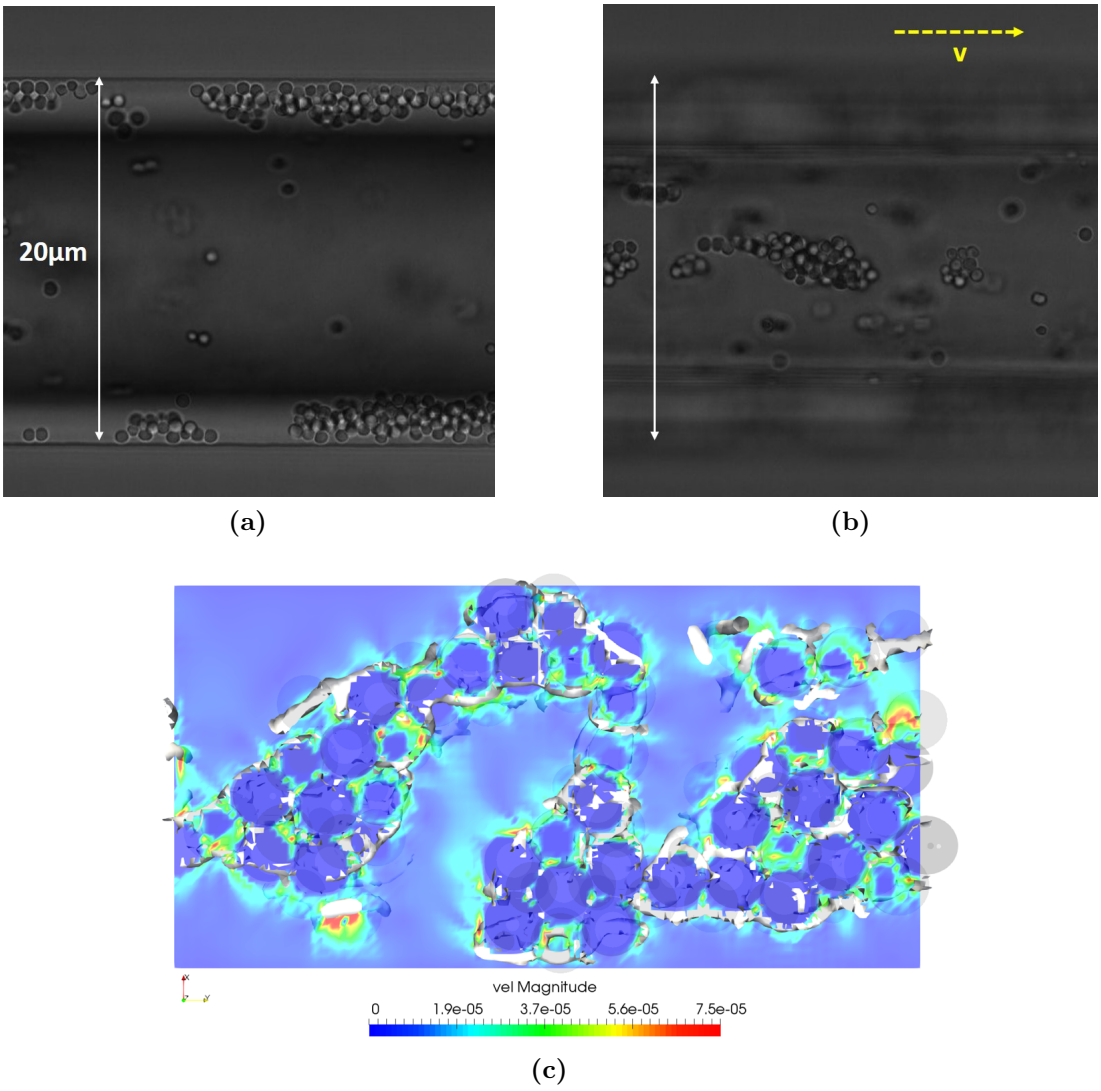

(a) (b)

(c)

Figure 7.4 *Channel flow images showing (a) particles accumulating and moving slowly on walls of the channel slides, (b) flow of small broken clusters of nematic colloids in the middle of channel slides and (c) flow profile of quadrupolar nematic colloids suggests an enhanced flow velocity in the defect network, courtesy Oliver Henrich.*

Table 7.1 *The values of n and yield stress σ_y from the Herschel-Bulkley relation for nematic composites.*

Composites	volume fraction, ϕ	n	σ_y (Pa)
PMMA in NC1	0.13	0.7 ± 0.08	11.2 ± 0.58
PMMA in NC1	0.16	0.5 ± 0.14	11.8 ± 0.61
PMMA in 5CB	0.2	0.75 ± 0.01	-
PMMA in NC1	0.25	0.41 ± 0.03	8.68 ± 0.91
PMMA in NC1	0.27	0.33 ± 0.15	37.17 ± 1.08
PMMA in 5CB	0.3	0.76 ± 0.01	7.91± 0.71
PMMA in 5CB	0.4	0.98 ± 0.01	16.58 ± 1.61

reduction upon shearing is, therefore, very significant and sharp, as depicted schematically in the Figure: 7.3.

Stress curves from flow rheology are plotted in Figures: 7.2 and 7.3 b. The curve was fitted using Herschel-Bulkley relation [71], $\sigma = \sigma_y + k\dot{\gamma}^{n_i}$, where the index $n_i < 1$ for shear - thinning samples. The value of n_i and yield stress, σ_y, for these composites are tabulated in Table: 7.1.

7.3 Effect of surface charge

After studying the flow rheology of uncharged composites in NC1, we were inspired to study the effect of the surface charge on their rheology. Both negatively charged Ani PS and positively charged Cat PS composites in NC1 were exposed to shear stress, and the resultant viscosity curves are drawn in the Figure: 7.5.

Both the charged composites exhibit shear-thinning behavior; however, the rate is greater for positively charged Cat PS in NC1 (-0.74± 0.19) as compared to negatively charged Ani PS (- 0.52±0.13). This is explained by the weaker anchoring strength found in Ani PS in NC1 composites (see Figure: 6.20), which allowed particles to entangle but the structure is different - more crystal like, rather than fractal like. Therefore, a higher relative concentration of colloids is required to achieve the same value of low shear viscosity. Because of the lower value of low shear viscosity, a shorter distance to the point of shear thinning is present - thus the gradient is lower for charged colloids. However, for both negatively and positively charged composites, the addition of more particles enhances the low shear viscosity.

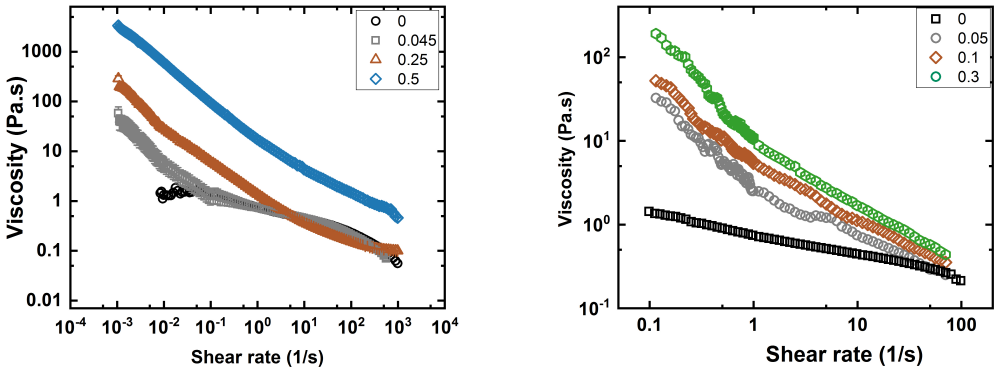

(a) (b)

Figure 7.5 *Shear viscosity (η) Pa.s of (a) Ani PS in NC1 liquid crystals and (b) Cat PS in NC1 plotted against shear- rate, for various volume fractions: $0.05 \leq \phi \leq 0.5$. Shear-thinning behavior and the absence of a low shear-rate Newtonian plateau are clearly observed.*

7.4 Power-law behavior

The power-law index (n_{PL}) values calculated from the viscosity curve of the composites, plotted against ϕ are shown in the Figure: 7.6. The value of n_{PL} for uncharged PMMA in both thermotropic (PMMA-PHSA in 5CB) and lyotropic (PMMA in NC1) decreases with increasing particle concentration. However, Ani PS has the same value of n_{PL} independent of particle concentration. For PMMA in NC1 suspension, it is seen that at $\phi\% = 12.73$, there is a sudden decrease in the value of n_{PL}. But the value of n_{PL} for uncharged composites in both thermotropic and lyotropic composites plateaus with a value of 0.07 ± 0.01 at $\phi\% \geq 40$. This value is one order of magnitude lower than the hard-sphere concentrated suspension which has n_{PL} - 0.4 ([34, 171]). On the other hand, n_{PL} for Ani PS in NC1 composites do not show any sharp decrease in their value with increasing volume fraction but a plateau with a value similar to solid-sphere dense suspension of 0.4 ± 0.05. This can be attributed to the weak anchoring between Ani PS and NC1 LCs, which does not form entangled network-like structure in nematic LCs but form a compact disconnected cluster.

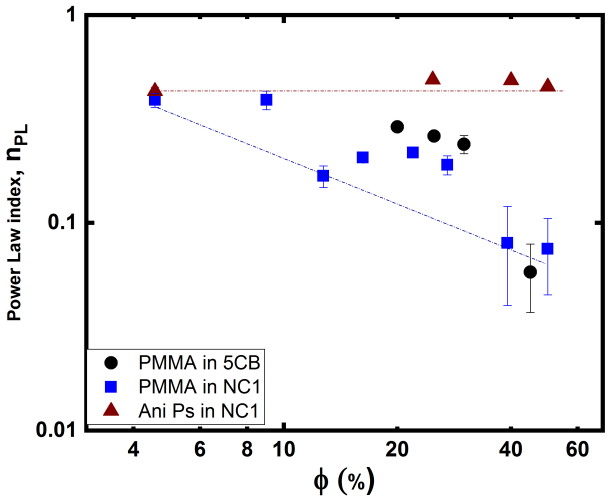

Figure 7.6 *Power-law indices plotted against volume fraction: PMMA-PHSA in 5CB (black), PMMA in NC1 (blue) and Ani PS in NC1 (brown). Line is a guide to eye.*

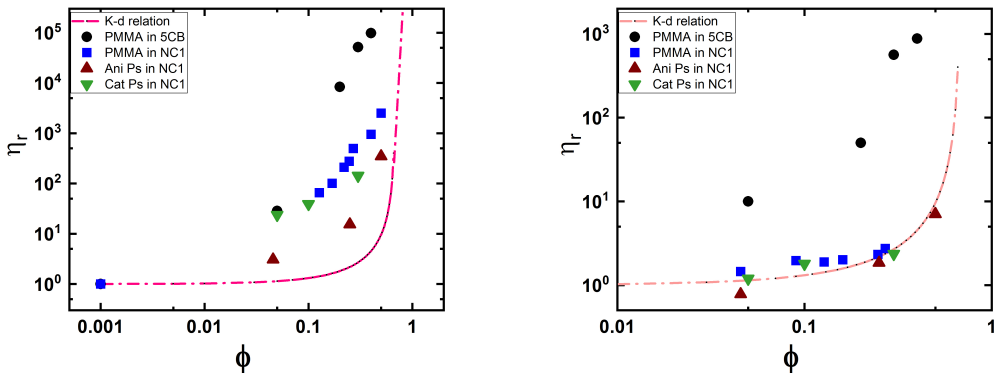

Figure 7.7 *Relative viscosities at (a) low $\eta_{0.01/s}$ and (b) high shear ($\eta_{95/s}$) for PMMA-PHSA in 5CB composites (circle), PMMA in NC1 (square), Ani PS in NC1 (triangle) and Cat PS in NC1 (down triangle) composites. The line is fitted to the Krieger-Dougherty relation, $\eta_r = \left(1 - \frac{\phi}{\phi_m}\right)^{-2.5\phi_m}$.*

7.5 Relative viscosity

Relative viscosities, ($\eta_r = \frac{\eta_\phi}{\eta_{LCs}}$), for the composites as a function of the colloidal concentration at low $\eta_{0.01/s}$ and high shear ($\eta_{95/s}$) are shown in Figure: 7.7. The thermotropic composites deviate from Krieger-Dougherty relation both at high and low shear rates, suggesting that the nematogens in the thermotropic composites are not affected by shear. However, the relative viscosity for lyotropic composites follows Krieger-Dougherty relation at high shear rate = 95/s, $\eta_r = [1 - \frac{\phi}{\phi_m}]^{-2.5\phi_m}$, the value of $\phi_m = 0.58$ was used to fit the data. This behavior suggests that the micellar nematogen is broken at high shear and reorganise to form spherical micelles which no longer exhibit nematic phase. Therefore the dispersion acts more like a normal colloid at high shear in the lyotropic nematic. However, the relative viscosities at low shear rate (0.05/s), Figure: 7.7, do not follow Krieger- Dougherty relation for filled lyotropic compsoites as the micelles nematogens are in equilibrium without being deformed or broken.

7.6 Nematic emulsion

We have studied the flow rheology of two sets of concentrated $\phi > 0.2$, nematic emulsion. Nematic emulsions were made from two different viscosities, (a) 0.05 Pa.s and (b) 0.5 Pa.s of PDMS dispersed in NC1 LCs. A plot of shear viscosity as a function of shear-rate for PDMS(0.05) emulsion exhibiting shear-thinning behavior, is shown in the Figure: 7.8. The data were fitted using the power-law equation. The value of the power-law index (Figure: 7.8b) decreases with increasing volume fraction, a behavior also observed in solid-sphere PMMA composites in NC1.

The solid-like behavior of drops can be explained by the formation of an elastic inter-facial layer at the drop surface, and this elastic cover changes radically the boundary conditions between the two fluids and prevents deformations of the liquid inside the drops up to $\phi \leq 0.58$. The increase of the concentration of drops in emulsions results not only in increased viscosity at low shear rates (i.e., Newtonian viscosity), but also in the appearance of strong non-Newtonian effects, a shear rate dependence decrease in viscosity.

The relative viscosities for nematic emulsions are plotted in Figure: 7.9. Nematic

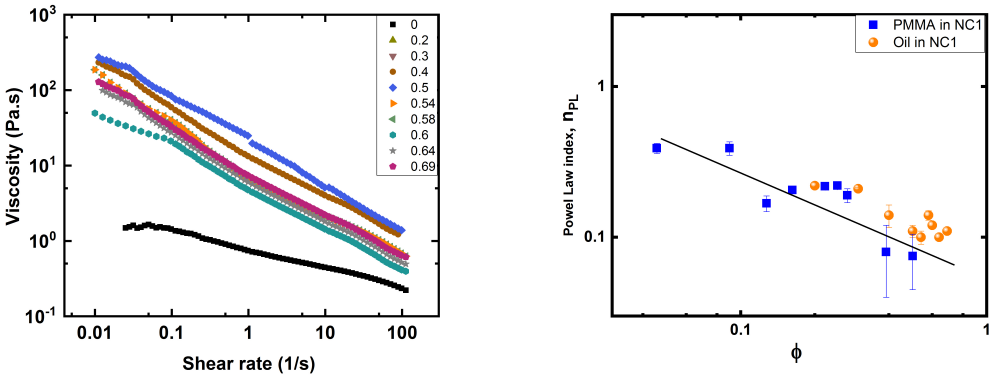

(a) (b)

Figure 7.8 *(a) Viscosity curve for PDMS (0.05) nematic emulsion and (b) Power-law index obtained from viscosity curve plotted against ϕ, hard-sphere composites (blue square) and emulsion (orange cirlce).*

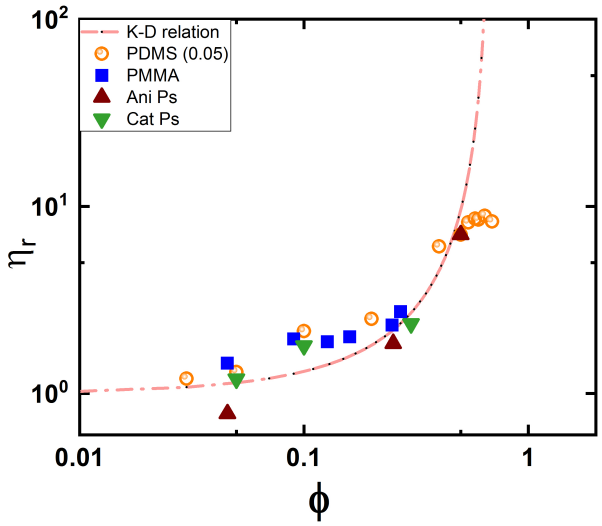

Figure 7.9 *Relative viscosities at high shear-rate $\eta_{95/s}$ for lyotropic composites, (a) PMMA in NC1 (square), (b) Ani PS in NC1 (triangle), (c) Cat PS in NC1 (down triangle) and (d) PDMS (0.05 Pa.s) emulsion (cirlce) composite. The line is fitted to the Krieger-Dougherty relation.*

emulsions follow solid-sphere composite behavior for volume fractions, $\phi \leq 0.58$, but deviate from the Krieger-Dougherty relation beyond. The deviation volume fraction is at the glass transition, $\phi_g = 0.58$, a behavior which was also observed in PDMS emulsion in isotropic solvent [171]. This is in accordance with the amplitude sweep data, section: 6.2.4. At $\phi = 0.58$, the inter droplet separation becomes less than 1.11 and they no longer remain entangled by the defects but start to touch each other and coalesce. This changes the flow behavior of the nematic emulsions similar to dense emulsions.

7.7 Summary

- The zero-shear viscosity of filled charged and uncharged nematic composites increases with the volume fraction. The concentrated composites, $\phi > 0.2$, exhibit exceptional shear-thinning behavior, with the value of power-law index ~ 0.11, which is lower than for dense colloidal suspension ~ 0.4 and to those of polymer melts ~ 0.3.

- The relative viscosities of the hard-sphere lyotropic nematic composites at high shear-rate ($\dot{\gamma} = 95/\text{s}$) follow the Krieger-Dougherty relation suggesting that the micellar nematogens are broken at high shear and form isotropic spherical micelles.

- Nematic emulsions show identical flow behavior to solid-sphere composites for low volume fractions composites, $\phi = \phi_g < 0.58$, but deviate from the Krieger-Dougherty relation beyond ϕ_g.

Chapter 8

Structure and dynamics in filled lamellar phase.

The rheology of filled lamellar lyotropic phases has been considered in depth before [23, 51, 72, 99]. We present measurements on colloids in a lamellar system made using the same ingredients as for the lyotropic nematic system so that we can compare directly the rheology of filled nematic and lamellar systems. In this chapter, we have attempted to study the rheology of the lamellar phase formed from a ternary mixture of anionic surfactant-SDS, 1-decanol, and water. Filled lamellar composites were formed by dispersing PMMA-PVP particles in the lamellar liquid crystal. Lamellar liquid crystalline textures may show homeotropic or focal-conic (threadlike, mosaic or oily streaks patterns), [166], [85] texture under cross-polariser, see Figure: 4.8. The proposed orientation of SDS and 1-decanol in the bi-layer structure is represented in the Figure: 4.6.

8.1 Rheology of lyotropic lamellar LCs.

The strain-dependent storage (G') and the loss (G'') moduli of L_α as compared with thermotropic nematic - 5CB and lyotropic nematic (NC1) LCs are shown in Figure: 8.1. The value of G' for L_α is two orders of magnitude greater than that of NC1 LCs with $G' > G''$ up to $\gamma \leq 4.2$ %. The lamellar phase behaves as an elastic system with high yield stress. One of the most significant differences between both lyotropic lamellar (rhombus) and nematic (square) liquid crystals are the

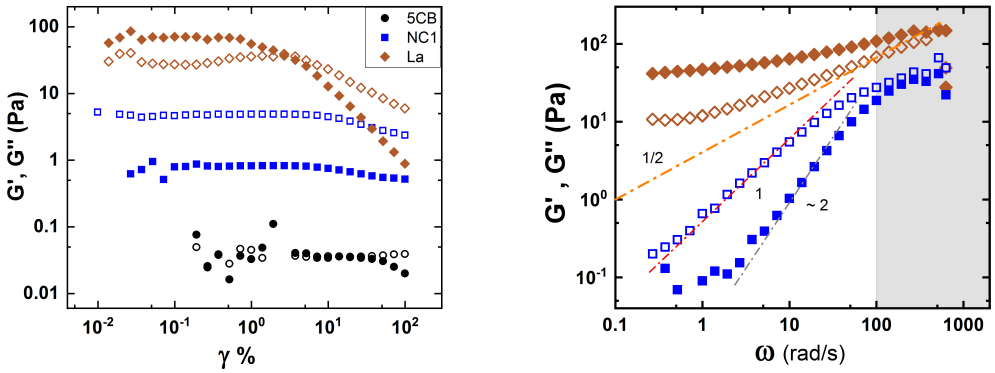

Figure 8.1 *The mechanical spectrum of G' and G'' as (a) a function of applied strain and (b) a function of frequency for 5CB (black), NC1 (blue) and L_α (brown) phases of LCs.*

appearance of yield stress. The solid-like behavior of the L_α phase is explained by their intrinsic ordered bi-layer structure, which gives rise to multiple defect lines because a bi-layer structure cannot continue indefinitely and therefore defects arise as opposed to nematic phases where the director can relax to form a defect-free structure if it has a sufficient length scale to do so (i.e. it is not confined). A cross-polariser image of both lyotropic LCs (see Figure: 4.7 and 4.8) shows the different defect structures observed in these lyotropic LCs. The linear viscoelastic properties of lamellar phases were determined by means of frequency sweeps inside the linear viscoelastic region. As can be observed in the Figure: 8.1b, the frequency dependence of G' and G'' is always similar. Thus, almost constant values of G' and a clear minimum in G'' can be detected, a behavior prominent in glassy rheology [148]. This mechanical spectrum corresponds to the 'plateau' region, which has been related to the formation of an elastic structural network due to the interactions between liquid-crystalline domains [93]. This behavior is typical of a viscoelastic solid such as a combination of springs (elastic) and dashpots (viscous). At high frequency, the springs are able to elongate while the dashpots are moving slowly with time under the forced shear. At low frequency, the springs can also extend, however the dashpots have sufficient time to move and their extension exceeds that of the springs.

Tan $\delta = G''/G'$ curve for pure L_α is non-linear but increases with frequency beyond 1 rad/s as for all strain values. But the absolute value of tan $\delta < 1$ for the entire frequency spectrum confirming that the defects in lamellar LCs exhibit strong elastic characteristics.

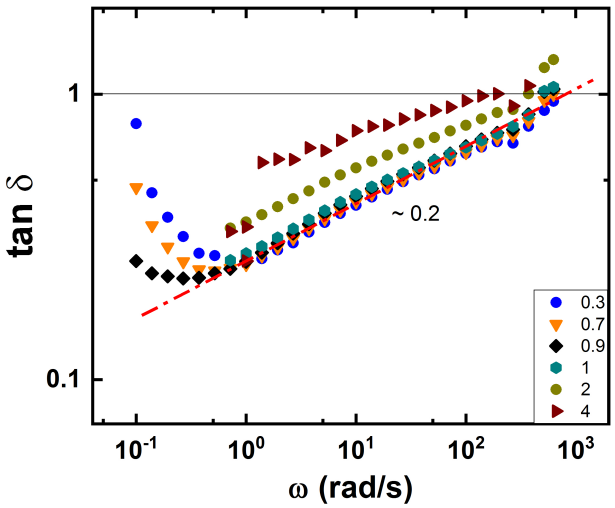

Figure 8.2 *Tanδ* $= G''/G'$ *as a function of angular frequency* ω *in rad/s for* L_α *LCs for* $\gamma = (0.1 - 10)\%$.

8.2 Influence of filler on the rheology and microstructure of filled lamellar.

Microspheres of PMMA-PVP were dispersed in lamellar lyomesophases to create composites of varying volume fraction, ϕ = 0.05 - 0.5. Confocal micrographs of dilute, $\phi = 0.05$, and concentrated , $\phi = 0.3$, lamellar composites are shown in Figure: 8.3. In the dilute composites, the colloids form small disconnected clusters. The average cluster size calculated from 7 different sets of images is $\sim$ 50 $\pm$ 10 μm, and the clear nematic domain size was found to be $\sim$ 700 $\pm$ 21 μm. However, at high concentrations, the shape of the cluster transforms into a well-connected space spanning network structure, and the size of the nematic domain is reduced to $\sim$ 500 $\pm$ 4 μm. Thus the change in the microstructure of the composites and affecting the rheology results.

8.2.1 Oscillatory response

Following a similar route as NC1 LCs, the influence of filler concentration on the L_α composites was studied. It was observed from amplitude sweeps, that as the concentration of PMMA-PVP particles increases, the value of G' and G'' also increases. An amplitude sweep curve for $\phi = 0.30$ composite compared with pure

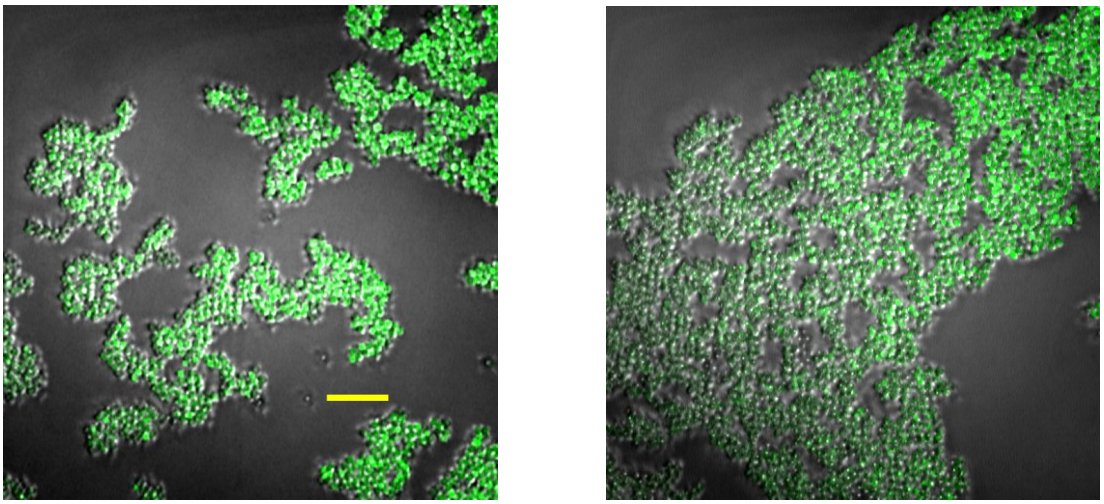

(a) (b)

Figure 8.3 *Microstructure of PMMA particles dispersed in L_α for (a) $\phi = 0.05$ and (b) $\phi = 0.3$ as seen under confocal microscope (fluorescence channel) Green spheres are PMMA beads and dark regions represent L_α medium. PMMA beads form irregular shaped space spanning cluster at high concentration. Scale-bar is 20 μm.*

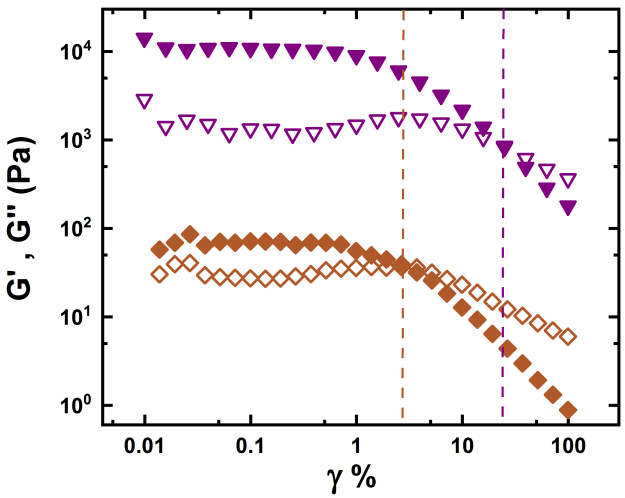

Figure 8.4 *Amplitude sweep for $\phi = 0.3$ composite (purple) as compared to pure L_α phase. Closed symbol is G' and open symbol is G''.*

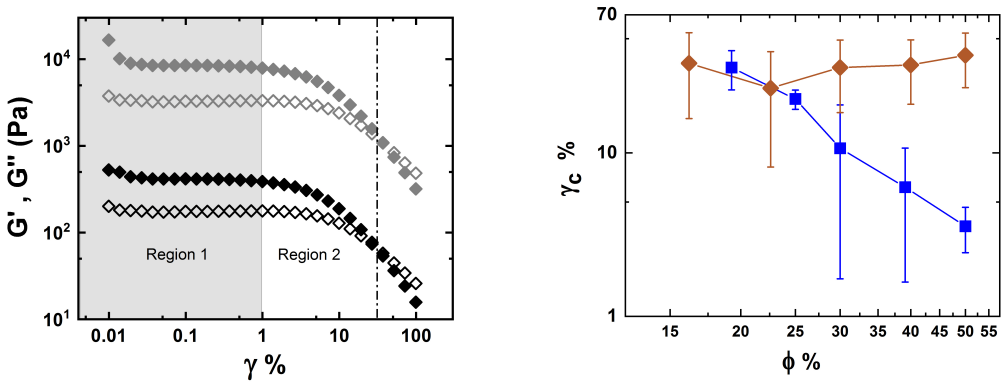

Figure 8.5 *(a) Amplitude sweep for ϕ = 0.2 (black) and 0.3 (grey) composite. (b) Yield strain, γ_C, for the lamellar composites (rhombus) as compared with the NC1 composites (square).*

unfilled L_α phase is shown in Figure: 8.4. G' (LVR) for $\phi = 0.3$ composite is $\sim$ 10000 Pa which is two orders of magnitude greater than the pure lamellar LCs with $G' \sim 100$ Pa. The critical yield strain, γ_c, where $G' = G''$, also has increased with volume fraction from 3 % to 16 % for pure and filled LCs respectively.

The Figure: 8.5 a compares the amplitude sweep of two concentrated ($\phi = 0.2$ and 0.3) composites. The plateau region (LVR) remains the same for both the composites with the crossover happening at the same strain. The plot of yield strain Figure: 8.5 b suggests that the yield value does not change with the concentration, unlike for nematic composites. A detailed plot representing the value of G'(LVR) and G''(LVR) for lamellar composites is drawn in Figure: 8.6. The inset shows the two regimes of dynamic moduli, for $\phi \leq 0.1$ the value of G' and G'' are of the same order of magnitude as that of unfilled liquid crystals, but there is a rapid increase in the values of G' and G'' beyond $\phi \geq 0.2$. The comparison with NC1 composite is evident, the value of G'(LVR) for L_α composites greater than for NC1 composites. G' shows an increase with ϕ with $G' - G_0 = \phi^p$, where p = 1.57 $\pm$ 0.24. The value of both G' and G'' for the lamellar composites are greater than for the NC1 and 5CB composites.

The elevated value of G' at high volume fraction can be attributed to the space spanning cluster matrix (see Figure: 8.3), which holds the particles together, forming a stable gel-like system. But as the applied strain increases, the structure deforms finally yielding with G'' becoming greater than G'. The critical yield strain, γ_c, remains $\sim 30 \pm 4$ % for different concentration of composite as shown

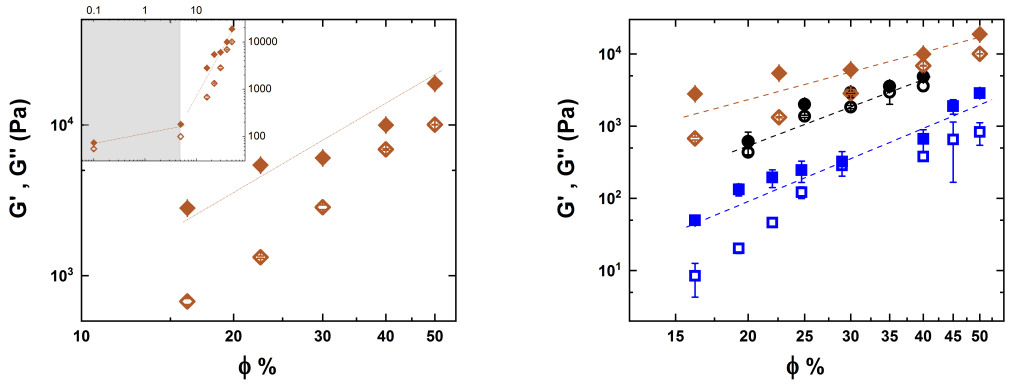

Figure 8.6 *(a) Storage modulus (G') and loss modulus (G″) as a function of volume fraction (ϕ)) of PMMA particles dispersed in L_α. Inset shows the two regimes of dynamic moduli, for (b) $\phi \leq 10\%$ the value of G' and G'' are of the same order of magnitude as that of unfilled liquid crystals but there is a rapid increase in the values of G' and G'' beyond $\phi \geq 0.2$.*

in figure: 8.5 unlike the NC1 composites whose value decreases with increasing ϕ.

8.2.2 Dynamic response

A frequency sweep was conducted for PMMA-PHSA filled lamellar LCs composites with the same experimental condition as used in the amplitude sweep. The frequency sweep profile was recorded at different values of strain from 0.1 to 10 % over four decades of frequency, 0.1 to 600 rad/s. From oscillatory strain sweep, two regions (a) LVR and (b) yielding were identified; see Figure: 8.5 a.

Region 1

The LVR for $\phi = 0.3$ composites were restricted to $\gamma \leq 1\%$. The frequency sweep profile was recorded for the strain values below 1% is reported in Figure: 8.7. Both G' and G'' shows a weak dependence on frequency with $\omega^{1/5}$. G' remains approximately the same in the whole frequency range studied. This behavior is characteristic of a gel-like sample. The plot of tan δ (Figure: 8.7 b) reveals that the composites behave as an elastic solid with tan$\delta < 1$ for the entire frequency spectrum.

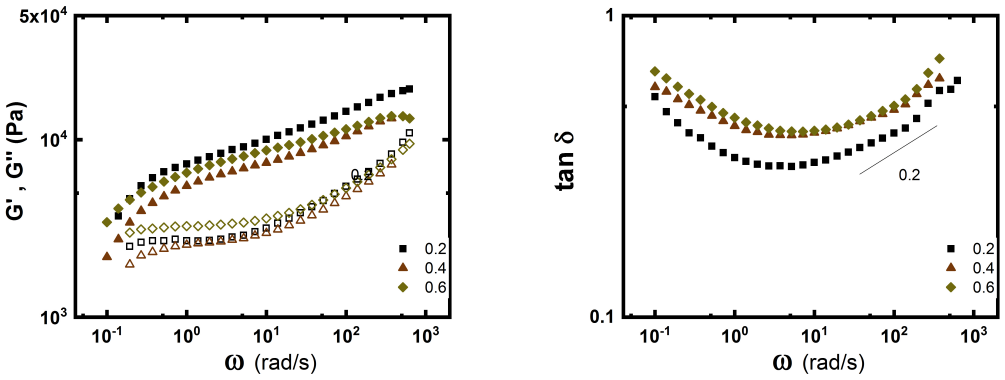

Figure 8.7 *(a) G' and G'' as a function of angular frequency ω in rad/s at low strain, $\gamma \leq 1\%$ in the LVR region (region 1) where G' and G'' remains constant as compared with $\gamma\%>2\%$ where the microstructure of the sample has deformed with decreasing value of G' and G'' (b) Tan δ as a function of ω in region 1. Tan δ shows a weak dependence on ω.*

Region 2

Frequency spectra of filled, $\phi = 0.3$, lamellar composites and pure L_α LCs are compared in Figure: 8.8. It is interesting to note that for the angular frequency range from 0.01 to 100 rad/s, the elastic moduli shows a plateau with the viscous component increasing as $\omega^{1/2}$ at higher frequencies. The system does not show a linear response, and under these nonlinear conditions, the storage modulus G' is higher than the loss modulus over the whole angular frequency range, unlike pure lamellar LCs, which show a clear minimum. This solid-like viscoelastic behavior is strongly correlated with the defect density. In fact, Larson *et al.* [100] showed that both G' and G'' decrease when the defects are removed by applying a large amplitude oscillatory shear. Hence the plateau modulus reflects the defect density. This result coincides with the idea that systems with yield stress behave as a solid until a certain threshold value, and they do not have any finite structural relaxation time [63].

Nemeth *et al.* [133] reported this behavior only in the lamellar liquid crystalline phase, but from our studies, these characteristics are present in concentrated lamellar composites. The increase of G'' may be attributed to slow reorganizations of the system (motion of lamellar or other liquid crystalline phases depending on the system). These reorganizations correspond to the rupture of weak bonds in

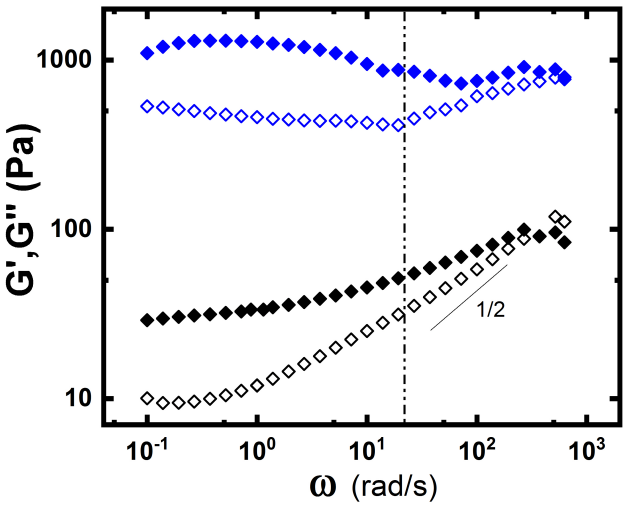

Figure 8.8 *G' and G''as a function of angular frequency, ω, in rad/s for ϕ = 0.3 and pure L_α LCs for $\gamma = 0.1 - 10\%$.*

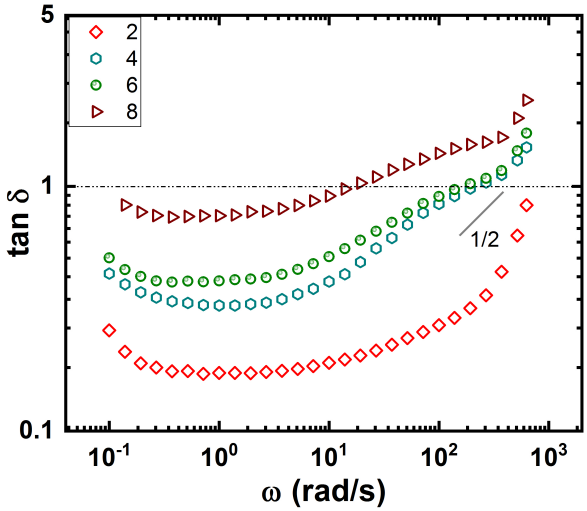

Figure 8.9 *Tanδ = G''/G' as a function of angular frequency ω in rad/s for PMMA in L_α LCs in the yielding region for $\gamma > 1\%$.*

the system and donot affect the elasticity of the system, i.e., G' changes a little. These relaxations result in energy loss and lead to an increase of G''.

The tan δ values of filled lamellar composites as a function of frequency, ω, for different strain, $\gamma > 1 - 10\%$ is plotted in Figure: 8.9. The plot reveals that the value of tan δ is directly proportional to ω. The more liquid-like character of the composites is reflected at higher frequency, for example $\omega > 10$ rad/s where tan $\delta > 1$, with tan$\delta \sim \omega^{1/2}$. This is because the suspension has yielded and bi-layers have reoriented in the direction of flow at higher $\gamma > \gamma_c$.

Thus we conclude, the curve of tan δ is non-linear, with tan δ showing a slight negative slope at lower frequency and increase with $\omega^{1/2}$ beyond a critical frequency, ω_c. We define ω_c, as the frequency where the value of tan $\delta = 1$. The value of critical frequency is inversely proportional to the strain values.

8.3 Steady state flow rheology

8.3.1 LCs comparison

The evolution of apparent viscosity as a function of shear rate for the lamellar phase shows the characteristics of a shear-thinning fluid, showing, in general, a power-law decrease in viscosity see Figure: 8.10. Flow properties of lamellar liquid-crystalline systems are strongly dependent on shear rate and composition. It can be observed that the viscosity curve is nonlinear in the LCs system. This is explained from the experimental error as the data was collected in steps, and each bump represents the start of a new step. The zero shear viscosity ($\eta at 0.001/s$) of L_α is two orders of magnitude greater than for NC1 LCs, which is consistent with G" values from strain amplitude sweep. Viscosity decreases on increasing shear rate and follow power-law behavior, $\dot{\gamma} = \eta^{n_{PL}-1}$, with n_{PL} = 0.44 and 0.87 for lamellar and nematic LCs respectively, a complete absence of a shear-independent viscosity plateau region. Similar shear-thinning behavior was obtained for a CTAB/1-hexanol/water system lamellar phase [130]. This shear-thinning behavior has been related to the formation of ordered bi-layer structures being aligned in the flow direction for the lamellar phase. For the nematic phase, this decrease in viscosity was attributed to the partial alignment of rod-like micelles in the direction of flow.

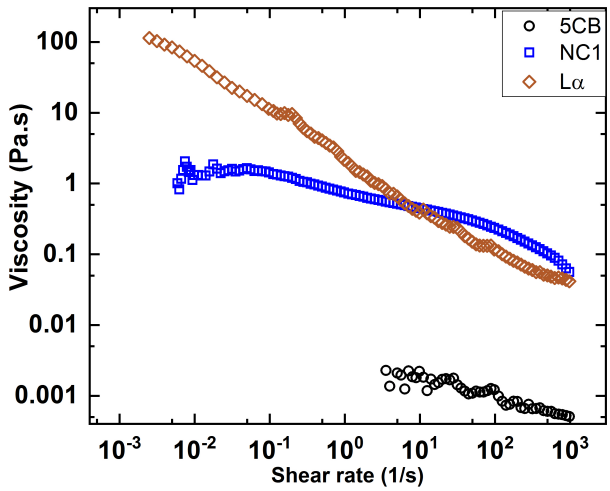

Figure 8.10 *Shear viscosity (η) in Pa.s for different liquid crystal, thermotropic nematic - 5CB (black), lyotropic nematic - NC1 (blue) and lyotropic lamellar (L_α) (brown).*

8.3.2 Influence of filler

The filled lamellar composite exhibits exceptional shear-thinning behavior, as depicted in the Figure: 8.11. The low-shear viscosity (η at 0.05/s) of the composites increases with the concentration of particles. The data was fitted using a power-law equation, $\dot{\gamma} = \eta^{n_{PL}-1}$, where n_{PL} is the power-law index. The value of n_{PL} for different volume fractions of lamellar composites is plotted on Figure: 8.11b for both NC1 and L_α composites. The value of n_{PL} is close to 0.1 for the different volume fractions of lamellar composites proving that all lamellar composites ($\phi > 0.15$) exhibit the same flow behavior, unlike NC1 composites. The dilute ($\phi < 0.15$) NC1 composites have a low power-law index stating a low shear-thinning rate; however, concentrated composites ($\phi \geq 0.2$) exhibit similar flow behavior as lamellar composites.

Relative viscosities ($\eta_r = \frac{\eta_\phi}{\eta_{L_\alpha}}$) at two different shear-rates, (a) $\dot{\gamma} = 0.05$/s and (b) $\dot{\gamma}$= 95/s as a function of composite volume fractions are shown Figure: 8.12. At low shear rate, $\dot{\gamma}$, the relative viscosities follow the Krieger-Dougherty relation. But this behavior is not evident at high shear - rate when the composites have changed their structure.

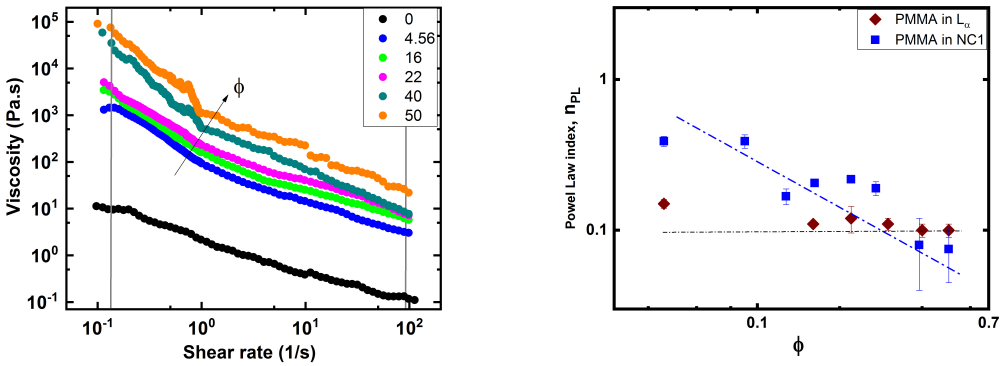

(a) (b)

Figure 8.11 *(a) Viscosity curve for different volume fraction of Lα composites (different colors are for different volume fractions), (b) Power-law index as a function of ϕ for L_α and NC1 composites.*

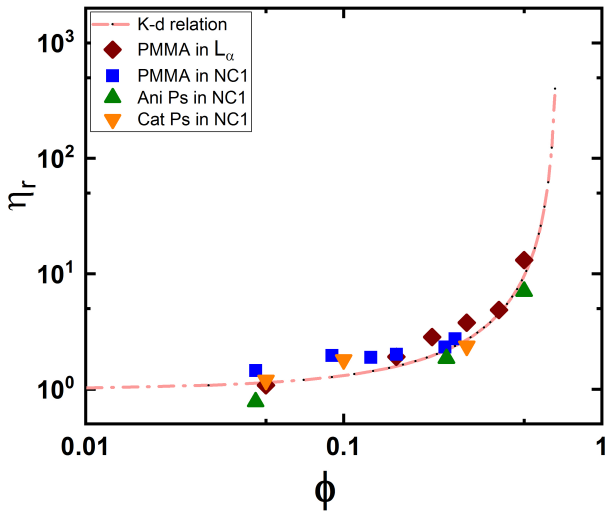

Figure 8.12 *Relative viscosities (at $\dot{\gamma}$= 0.05/s and at 95/s) plotted against ϕ for lamellar composites.*

8.4 Summary

Our rheology results for L_α LCs repeats the findings reported in the literature and allows us to set the rheology of filled nematics in context.

1. $G' \propto \phi^2$ for filled nematics, but there is a lower power dependence ($G' \propto \phi^{1.5}$) for lamellar composites.

2. The critical yield strain, γ_c, for filled nematics decreases with increasing volume fraction, but for filled lamellar, the value of yield strain remains constant.

3. The shear rheology suggests an exceptional shear-thinning behavior for concentrated ($\phi > 0.2$) nematic composite which is also a characteristic behavior of filled lamellar composites with n_{PL} for nematic and $L_\alpha \sim 0.1$.

Chapter 9

Conclusion and outlook

The research presented in this doctoral thesis spans several original findings about filled nematic liquid crystals composites. Thus, in this concluding chapter we summaries the results presented in this thesis.

9.1 Structure and dynamics of filled nematic composites.

We have studied the dynamic response of filled thermotropic nematic composites. Unfilled pure nematic liquid crystals without defects flow like a viscous liquid exhibiting Maxwell fluid like behavior, $G'' \propto \omega$. However, on addition of particles beyond a critical volume fraction, $\phi_c > 0.18$, a class of highly elastic soft-solid is formed. From the amplitude sweep, two different regions were identified, (a) Region 1 - LVR and (b) Region 2 - yielding region. The value of G' in the LVR shows a sharp increase with volume fraction at $\phi > 0.18$ with functional form of $G' \propto \phi^2$. This power dependence on volume fraction is similar to colloidal suspensions over the glass transition, $\phi_g = 0.58$. However, the glass transition for filled nematics is considerably lower at $\phi = 0.18$.

From the frequency sweep, $G' > G''$ for infinite time, $\omega \to 0$ we find that the composite is highly stable. Above a critical frequency, we show that the soft-solid yields with $G'' \propto \omega^{1/2}$. We present a theory that indicates the yielding behavior is governed by the Ericksen number, E_r, and the viscous behavior is determined

by the confined nematic regions. We find that the frequency dependence of the composites is independent of the volume fraction, ϕ, indicating that it is neither an active nor a passive filled system. The behavior of composite is determined by the orientation of defect lines in the nematic LCs and the colloids merely serve to create and support Saturn-ring defects.

For the first time, we explore filled lyotropic nematic composites and find their rheology and microstructure to be very similar to their thermotropic counterparts. We show that charge interactions weaken the composite strength when colloids are dispersed in a charged nematic liquid crystalline medium. The microstructure of the charged composites exhibit crystal array-like structures as opposed to loose randomly-packed networks formed in uncharged composites, see Figure: 6.17. We also show that the deformable colloids in nematic emulsions show similar rheological behavior like the solid-sphere dispersion in lyotropic system up to $\phi \leq 0.54$ but deviate near the glass transition volume fraction. We attribute this deviation to the change of interparticle separation at higher volume fractions. At $\phi = 0.54$, the inter particle separation between droplets decreases from 1.11 to 1.05, thus they are no longer separated by Saturn-ring defects but start to touch each other and coalesce, therefore changing the microstructure of the composites and their rheological behavior.

The low shear viscosity of filled nematic composites increases considerably with colloidal volume fraction. However, on the application of stress, the concentrated composites, $\phi > 0.2$, exhibit exceptional shear-thinning behavior, with power-law index ~ 0.11, which is lower than for dense colloidal suspension ~ 0.4 and to those of polymer melts ~ 0.3. The relative viscosities at both low (0.01/s) and high (95/s) shear rate were plotted against the Krieger-Dougherty relation. At low shear-rate both filled thermotropic and lyotropic composites does not follow Krieger-Dougherty relation because the nematogens are in equilibrium without being affected by shear. However, at high shear lyotropic nematic composite follow K-D relation suggesting that the micellar nematogens are disrupted at high shear and the composites behave like dense colloidal suspensions. The flow rheology of lyotropic nematic emulsions show identical flow behavior to solid-sphere composites for volume fraction less than glass transition, $\phi = \phi_g < 0.58$, but deviates beyond ϕ_g.

9.2 Dynamics of lamellar composites in context of filled nematics.

Rheology measurements on lamellar composites are consistent with findings reported in the literature and allows us to set the rheology of filled nematics in context. The value of G' shows a lower power dependence on volume fraction, $G' \propto \phi^{1.5}$, as compared to filled nematic composites, $G' \propto \phi^2$. However, the value of critical yield strain, γ_c, remains constant for filled lamellar composites whereas the value decreases for filled nematics with increasing volume fraction. The flow profile of lamellar composites suggests a high shear-thinning behavior for concentrated lamellar composites as compared to the filled nematic counterpart.

Collectively, these results support the suggestion that a filled lyotropic liquid crystal could offer an alternative route to creating stable formulations, that are highly tunable, and shear-thinning, without the use of polymers. However, in order for uni axial micelles to be the route of choice, further research and development will be required to identify nematic phases made of bio-compatible surfactants and co-surfactants. Charge should be avoided since it can lead to phase separation when charged colloids are dispersed within. Our experiments indicate that anchoring at the surface of colloids can affect the microstructure and future work could involve new characterization methodologies to characterize the anchoring strength more quantitatively. Furthermore, computer simulation could enlighten experimentalist to help us understand the conditions under which the crystal structure is formed and, for the defect-mediated gel, help us understand the increase in the number of percolating disclinations across a composite with the filled volume fraction.

Appendix A

Topological defects in nematics.

Topological defects are the defects which arise from breaking continuous symmetry of the system and cannot be fixed by any local rearrangement of molecules. In three-dimensional space, these defects are where the order parameter of the system under consideration is classified by the homotopy groups $\Pi_n(V)$, n = D-d-1 [125] , where D is space dimension, in a 3D nematic, d is the defect dimension, V = P^2, n=1 for line defects enclosed by loops and n = 2 for point defects enclosed by sphere. Homotopy classification of defects can be done by; first defining the order parameter (OP) of the system, if the system is non-uniform then S is considered as a function of coordinates. Then all the values of OP are determined that do not alter the thermodynamic potential of the system. From the topological point of view, the order parameter space of the nematic phase is the projective plane $P^2 = \frac{S^2}{Z_2}$, where S^2 is the unit sphere in three dimensions. Every point on $\frac{S^2}{Z_2}$ denotes a particular orientation of $\vec{n}$. Since $\vec{n}$ and $-\vec{n}$ are equivalent, so any two diametrically opposite points on the sphere represents the same state. The director $\vec{n}$ maps all the point in the sphere.

A.1 Line Defects or Disclinations.

Nematic line defects are also known as disclinations to indicate the discontinuity in the inclination of molecules. Consider a disclination as shown in Figure: A.1 and surround the line by a loop Γ such that the director, $n(\vec{r})$ is defined at every point along Γ. Thus the function $n(\vec{r})$ maps Γ into some closed contour Ω

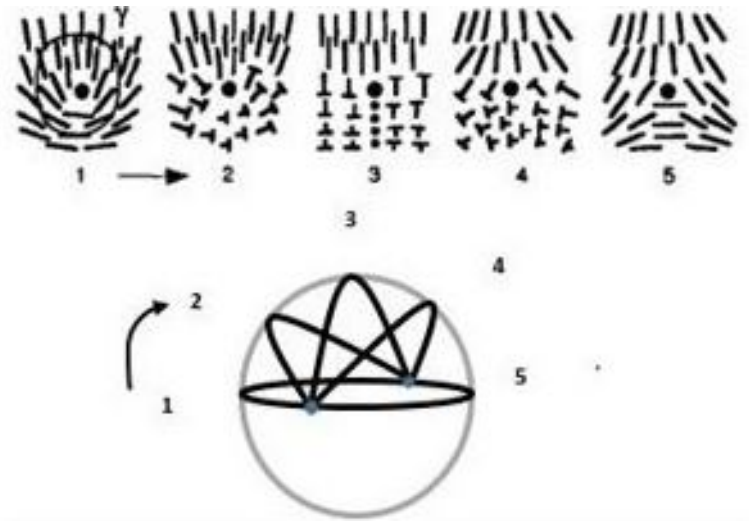

Figure A.1 *Stable disclinations in a nematic phase with their corresponding contours in* Γ *space.*

on the projective plane. Ω can be of two types; (a) like a circle which starts and terminates at the same point or (b) like a contour which connects two diametrically opposite points of the sphere. A circle in the first case can be contracted into a single point and for this scenario, $\vec{n}$ = constant, but contours cannot be contracted and their ends will remain diametrically opposite points of Ω. The corresponding defect line of contours is topologically stable. The homotopy group $\pi_1(\frac{S^2}{Z_2}) = Z_2 = 0, \frac{1}{2}$ is composed of two elements from the addition rules $\frac{1}{2} + \frac{1}{2} = 0$ and $\frac{1}{2} + 0 = \frac{1}{2}$. The elements of the homotopy group are called topological charge, s. The transformation between $\frac{1}{2}$ and 0 is energetically impossible as it will require the breaking of nematic phase symmetry; the only stable disclinations are those that correspond to the element of $\frac{1}{2}$. All the stable lines (1 and 5) can be transformed into each other by a rotation of π along the horizontal axis. The disclination shown on left (1) has a strength (k) of $\frac{1}{2}$ whereas the disclination of right (5) has a strength of -$\frac{1}{2}$. The strength is defined by how many times the director rotates by 2π while covering the circumference of the defect core once and the sign of k denotes the direction of rotation. The director field around a disclination follows from the minimization of the Frank free energy, Equation: 2.4. In one-constant approximation, the line tension energy F_d of the disclination can be calculated using R, the radius of enclosing sphere Γ and the radius of the disclination core r_c given by;

$$F_d = \frac{\pi}{4} K(1/2 + \log \frac{R}{r_c}) \tag{A.1}$$

The surface term is neglected in the above equation. The right-hand side of Equation: A.1, represents the elastic free energy per unit length around the line defect. The line energy calculated using the same equation, with $r_c \propto 10$ nm, average elastic constant K$\approx$ 12 pN and L around 10-100 μm is F_d =65-85 pN [139]. It can be seen that as R increases the energy also increases logarithmically, so if R tends to ∞, the energy also diverges logarithmically.

Since the energy diverges logarithmically, one has to introduce a lower cut-off radius of r_c, i.e., the radius of the disclination core. Its line energy, given by the first term, is derived in the following way, one assumes that the core of the disclination contains the liquid in the isotropic state with a free energy density ϵ_c necessary to melt the nematic order locally. The expression for ϵ_c is given by Equation: A.2. Now a rough approximation for the core energy, F_c, per unit length can be assumed:

$$\epsilon_c = \frac{K}{8}(1/r_c) \tag{A.2}$$

$$F_c = \frac{pi}{8}\frac{K_1 + K_2 + K_3}{3} \tag{A.3}$$

A.2 Point Defects

The two types of point defects found in nematic LCs are radial and hyperbolic hedgehogs. These defects are classified by second homotopy group; $\pi_2(\frac{S^2}{Z_2})$ = Z = (0, $\pm$ 1, $\pm$ 2, ...). The simplest point defect is radial hedgehog shown in Figure: A.2.

The director fields are rotationally symmetric about the vertical axis in both radial and hyperbolic hedgehogs. Consider a sphere of radius R, enclosing the point defect. Thus, the function $\vec{n}$ maps every point in that sphere. But these mapping cannot be contracted into a single point because the point defect will be unstable at that point. But if the mapped surface is wrapped N times around the sphere, the point defect is stable with topological charge s =1. In nematic LCs, it is not possible to distinguish between s and -s because $\vec{n}$ and $-\vec{n}$ are equivalent.

The energies of the hedgehog configurations are calculated from the Frank free

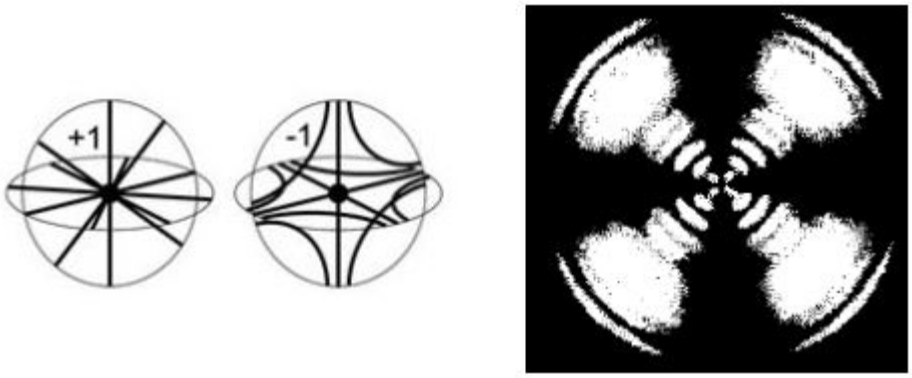

Figure A.2 *a) Schematics of radial and hyperbolic hedgehog. b) Spherical nematic droplets suspended in glycerin doped with lecithin. The director configuration is normal to the spherical surface. The image shows the point defect-hedgehog in the center of the droplet as observed as observed under cross polarizer.*

energy $F_{el} + F_{24}$ (see Equation: 2.28 and 2.6).

$$F_{radial} = 4\pi(2K_1 - K_{24})R \tag{A.4}$$

$$F_{hyper} = \frac{4\pi}{15}(6K_1 + 4K_3 + 5K_{24})R \tag{A.5}$$

Note that the Frank free energy of point defects does not diverge in contrast to the line energy. The hyperbolic-hedgehog has lower energy compared to the radial hedge-hog when $6K_1 - 5K_{24} > K_3$, and when $K_{24} = 0$, then hyperbolic hedge-hog is preferred as $K_1 \sim K_3$.

Bibliography

[1] Ravnik M., I., Tkalec U., & Osterman, N. (2007). Two-dimensional dipolar nematic colloidal crystals. *Phys. Rev. E*, *76*, 051406.

[2] A. Patil, & M. S. Ferritto (2013). Polymers for personal care and cosmetics: overview. *ACS symposium*.

[3] Abitbol, T., & Cranston, E. D. (2014). *Chiral Nematic Self-Assembly of Cellulose Nanocrystals in Suspensions and Solid Films*, chap. Chapter 4, (pp. 37–56).

[4] Agarwal, A., Huang, E., Palecek, S., & Abbott, N. L. (2008). Optically responsive and mechanically tunable colloid-in-liquid crystal gels that support growth of fibroblasts. *Advanced materials*, *20*(24), 4804–4809.

[5] Amaral, L., Santos, O., Braga, W., Kimura, N., & Palangana, A. (2015). Biaxial phase and coexistence of the two uniaxial nematic phases in the system sodium dodecyl sulphate–decanol–d2o. *Liquid Crystals*, *42*(2), 240–247.

[6] Amaral, L. Q., & Helene, M. E. M. (1988). Nematic domain in the sodium lauryl sulfate/water/decanol system. *The Journal of Physical Chemistry*, *92*(21), 6094–6098.

[7] Amaral L. Q., Helene M. E. M., Bittencourt D. R., & Itri R. (1987). New nematic lyomesophase of sodium dodecyl sulfate. *The Journal of Physical Chemistry*, *91*(23), 5949–5953.

[8] Anderson, V., & E.M., T. (2001). Cellular solid behaviour of liquid crystal colloids 2. mechanical properties. *The European Physical Journal E*, *4*(1), 21–28.

[9] Andreotti Bruno, P., Forterre Yoël (2013). *Granular Media: Between Fluid and Solid*. Cambridge University Press.

[10] Araki Takeaki, T. (2006). Colloidal aggregation in a nematic liquid crystal: Topological arrest of particles by a single-stroke disclination line. *Physical Review Letters*, *97*, 1–4.

[11] Awad, T. S., Johnson, E. S., Bureiko, A., & Olsson, U. (2011). Colloidal structure and physical properties of gel networks containing anionic surfactant and fatty alcohol mixture. *Journal of Dispersion Science and Technology*, *32*(6), 807–815.

[12] Axelrad Penina, L. (2006). *The Structure and Rheology of complex fluid*, vol. 87. OUP USA; Digital Reprint edition.

[13] Bajc J., Hillig G., & Saupe A. (1997). Determination of elastic constants and rotational viscosity of micellar liquid crystals by conductivity measurements. *The Journal of Chemical Physics*, *106*(17), 7372–7377.

[14] Barnes, H. (2000). *Elementary book of rheology*. University of Wales, Institute of Non-Newtonian Fluid Mechanics.

[15] Barnes, H. (2003). Review of the Rheology of Filled Viscoelastic Systems. *The British Society of Rheology*, *38*, 1–36.

[16] Barnes, H. (2003). Rheology characterisation of filled viscoleastic material. *Rheology reviews*.

[17] Barnes, H. A. (1994). Rheology of emulsions — a review. *Colloids and Surfaces A: Physicochemical and Engineering Aspects*, *91*, 89 – 95.

[18] Batchelor, G. (1977). The effect of brownian motion on the bulk stress in a suspension of spherical particles. *Journal of Fluid Mechanics*, *83*(1), 97–117.

[19] Batchelor G. K., G. (1972). The determination of the bulk stress in a suspension of spherical particles to order c2. *Journal of Fluid Mechanics*, *56*(3), 401–427.

[20] Beggs, H. D., & Robinson, J. R. (1975). Estimating the viscosity of crude oil systems. *Society of Petroleum Engineers*.

[21] Beica, T., Moldovan, R., Puica, M., & Frunza, S. (1274). Temperature dependence of the density of calamitic and discotic nematic lyotropic liquid crystals containing sodium lauryl sulphate/decanol/water. *Liquid Crystals*, (pp. 1275–1278).

[22] Birinci Elvan, K. (2006). Development of extrudate distortions in poly (dimethyl siloxane) and its suspensions with rigid particles Development of extrudate distortions in poly (dimethyl siloxane) and its suspensions. *Journal of rheology*, *50*.

[23] Bohlin .L, M. (1985). Oscillatory shear flow measurements on liquid crystalline phases with hexagonal and cubic structures. *Journal of colloid and interface science*.

[24] Bower, C., Gallegos, C., Mackley, M. R., & Madiedo, J. M. (1999). The rheological and microstructural characterisation of the non-linear flow behaviour of concentrated oil-in-water emulsions. *Rheologica Acta*, *38*(2), 145–159.

[25] Brochard, F., & de Gennes, P.G. (1970). Theory of magnetic suspensions in liquid crystals. *J. Phys. France*, *31*(7), 691–708.

[26] Bukusoglu, E., Pal, S. K., de Pablo, J. J., & Abbott, N. L. (2014). Colloid-in-liquid crystal gels formed via spinodal decomposition. *Soft Matter*, *10*, 1602–1610.

[27] Burghardt, W. R. (1991). Oscillatory shear flow of nematic liquid crystals. *Journal of Rheology*, *35*(1), 49–62.

[28] Busse, W. F. (1932). The physical structure of elastic colloids. *Journal of Physical Chemistry*, *36*.

[29] Candau S. J., C. (1990). Statics and dynamics of worm-like surfactant micelles. *Journal of Physics: Condensed Matter*, *2*, 6869–6892.

[30] Cappelaere E., Berret J. F., Decruppe J. P., Cressely R., & Lindner P. (1997). Rheology, birefringence, and small-angle neutron scattering in a charged micellar system: Evidence of a shear-induced phase transition. *Phys. Rev. E*, *56*, 1869–1878.

[31] Cassagnau, P. (2008). Melt rheology of organoclay and fumed silica nanocomposites. *Polymers with aligned carbon nanotubes: Active composite materials*, *49*(9), 2183–2196.

[32] Chaikin P. M., & Lubensky T. C. (2001). Principles of condensed matter physics. *MRS Bulletin*, *26*(11), 940–941.

[33] Chevalier Y., Z. (1990). The structure of micelles and microemulsions. *Reports on Progress in Physics*, *53*, 279–371.

[34] Chong, J. S. (2007). Rheology of colloidal suspension. *Journal of applied polymer science*, *15*(1971), 2007–2021.

[35] Čopar, S., Tkalec, U., Muševič, I., & Žumer, S. (2015). Knot theory realizations in nematic colloids. *Proceedings of the National Academy of Sciences*, *112*(6), 1675–1680.

[36] Cordobes, F., Franco, J., & Gallegos, C. (2005). Rheology of the lamellar liquid-crystalline phase in polyethoxylated alcohol/water/heptane systems. *Grasas y Aceites*, *56*.

[37] Course (1930). Viscoelasticity. *Review of viscoelastciity*, (pp. 283–342).

[38] Croze, O. A., & Cates, M. E. (2005). Nonadditivity of polymeric and charged surface interactions, consequences for doped lamellar phases. *Langmuir*, *21*(12), 5627–5638.

[39] Cui, M., & Kelly, J. R. (1999). Temperature dependence of visco-elastic properties of 5cb. *Molecular Crystals and Liquid Crystals Science and Technology. Section A. Molecular Crystals and Liquid Crystals*, *331*(1), 49–57.

[40] Cummins, H. Z. (1994). Relaxational dynamics in supercooled liquids: experimental tests of the mode coupling theory. *Physica A: Statistical Mechanics and its Applications*, *204*(1), 169 – 201.

[41] Daniel Bourgoin, W. (1980). Rheology of the lecithin-water system in its lamellar phase. *Rheologica Acta*, *19*, 226–238.

[42] de Andrade Lima L. R. P., & Rey A. D. (2006). Superposition principles for small amplitude oscillatory shearing of nematic mesophases. *Rheologica Acta*, *45*(5), 591–600.

[43] de Schepper I. M., Smorenburg, H. E., & Cohen E. G. D. (1993). Viscoelasticity in dense hard sphere colloids. *Phys. Rev. Lett.*, *70*, 2178–2181.

[44] Denis, A. (2018). Introduction to liquid crystals. *Journal of Molecular Liquids*, *1*(September), 1–32.

[45] Denn Morton M., M. (2014). Rheology of non-brownian suspensions. *Annual Review of Chemical and Biomolecular Engineering*, *5*(1), 203–228.

[46] Dhez, O., Nallet, F., & Diat, O. (2001). Influence of screw dislocations on the orientation of a sheared lamellar phase. *Europhys. Lett.*, *55*(6), 821–826.

[47] Dickinson, E. (1992). *An Introduction to Food Colloids*. Oxford University Press.

[48] Dickinson Eric, C. (2007). Heat set whey protein emulsion gels: role of active and inactive fille rparticles. *Journal of dispersion Science and Technology*, *2691*.

[49] Dong-Hwan Kim, D., Alexander Jahn (2015). Lyotropic liquid crystal systems in drug delivery: a review. *Journal of Pharmaceutical Investigation*, *45*, 1–11.

[50] Dong Wook Chae, B. (2007). Thermal and rheological properties of highly concentrated pet composites with ferrite nanoparticles. *Composites Science and Technology*, *67*(7), 1348 – 1352.

[51] Duke, R., & Chapoy, L. (1976). The rheology and structure of lecithin in concentrated solution and the liquid crystalline state. *Rheologica Acta*, *15*, 548–557.

[52] Einstein, A. (1906). Bestimmung der molekuldimension. *Ann. Phys. (Leipzig)*, *19*, 289–306.

[53] Ericksen, J. (1962). Hydrostatic Theory of Liquid Crystals. *Arch. Rational Mech. Anal.*, *9*, 371–378.

[54] F. Comelles, J. (1994). Influence of the polar phase in the formulation of cosmetics. *International journal of cosmetic science*, *16*, 121–136.

[55] Faroughi Salah Aldin, H. (2014). Crowding-based rheological model for suspensions of rigid bimodal-sized particles with interfering size ratios. *Phys. Rev. E*, *90*, 052303.

[56] Ferry, D., John (1948). Viscoelastic Properties of Polymer Solutions 1. *Journal of Research of National Bureau of standards*, *41*, 53–62.

[57] Figueiredo Neto, A., & Salinas Silvio R. A. (2005). *The Physics of Lyotropic Liquid Crystals: Phase Transitions and Structural Properties*. Oxford publishing.

[58] Frank, F. C. (1958). On the theory of liquid crystals. *Faraday Society*, *25*, 19–28.

[59] Fukuda Jun-ichi, Y., Yoneya Makoto (2004). Nematic liquid crystal around a spherical particle: Investigation of the defect structure and its stability using adaptive mesh refinement. *The European Physical Journal E*, *13*(1), 87–98.

[60] Gennes P G De, L. (1982). Dynamics of entangled polymer. *Annual review of physical chemistry*, *9*, 49–61.

[61] Gooch, J. W. (Ed.) (2007). *Cauchy's dispersion formula*, (pp. 167–167). Springer New York.

[62] Gotze, W., & Sjogren, L. (1992). Relaxation processes in supercooled liquids. *Reports on Progress in Physics*, *55*(3), 241–376.

[63] Gradzielski, M., Hoffmann, H., Panitz, J.-C., & Wokaun, A. (1995). Investigations on l2 phase and cubic phase in the system aot/1 - octanol/water. *Journal of Colloid and Interface Science*, *169*(1), 103 – 118.

[64] Gregory N. Smith, D., Samuel D. Finlayson, & Julian Eastoe (2016). The internal structure of poly(methyl methacrylate) latexes in nonpolar solvents. *Journal of Colloid and Interface Science*, *479*, 234 – 243.

[65] Gregory N. Smith, J. (2016). The internal structure of poly(methyl methacrylate) latexes in nonpolar solvents. *Journal of Colloid and Interface Science*, *479*, 234 – 243.

[66] Gu Yuedong, & Abbott Nicholas L. (2000). Observation of saturn-ring defects around solid microspheres in nematic liquid crystals. *Phys. Rev. Lett.*, *85*, 4719–4722.

[67] Guzmán, O., Kim, E. B., Grollau, S., Abbott, N. L., & de Pablo, J. J. (2003). Defect structure around two colloids in a liquid crystal. *Phys. Rev. Lett.*, *91*, 235507.

[68] H. Rehage, & H. Hoffmann (1991). Viscoelastic surfactant solutions: model systems for rheological research. *Molecular Physics*, *74*(5), 933–973.

[69] Han, C. (2012). *Multiphase Flow in Polymer Processing*. Elsevier.

[70] Hausnerova, B., Honkova, N., Kitano, T., & Saha, P. (2009). Superposed flow properties of ceramic powder-filled polymer melts. *Polymer Composites*, *30*(8), 1027–1034.

[71] Herschel W. H., B. (1926). Konsistenzmessungen von Gummi-Benzollösungen. *Kolloid Z.*, *39*, 291–300.

[72] Hirsch, M. R. (1982). A Comparison of Four Streamflow Record Extension Techniques. *Water resources research*, *18*(4), 1081–1088.

[73] Hollingsworth, A., Russel, W., van kats, C., & van Blaaderen, A. (2006). Preparation of phsa-pmma stabilizer for model hard sphere systems. *Material science*.

[74] Honek Tomas, S., Hausnerova Berenika (2005). Relative Viscosity Models and Their Application to Capillary Flow Data of Highly Filled Hard-Metal Carbide Powder Compounds. *Polymer composites*.

[75] Hunter, J. R. (2000). *Foundations of colloidal science*. Oxford publishing.

[76] I. M., K. (1959). A Mechanism for Non-Newtonian Flow in Suspensions of Rigid Spheres. *Journal of Rheology*, *137*(1959).

[77] Čopar, S., & Žumer, S. (2011). Nematic braids: Topological invariants and rewiring of disclinations. *Phys. Rev. Lett.*, *106*, 177801.

[78] Škarabot, M., Ravnik, M., Babič, D., Osterman, N., Poberaj, I., Žumer, S., Muševič, I., Nych, A., Ognysta, U., & Nazarenko, V. (2006). Laser trapping of low refractive index colloids in a nematic liquid crystal. *Phys. Rev. E*, *73*, 021705.

[79] Škarabot, M., Ravnik, M., Žumer, S., Tkalec, U., Poberaj, I., Babič, D., Osterman, N., & Muševič, I. (2007). Two-dimensional dipolar nematic colloidal crystals. *Phys. Rev. E*, *76*, 051406.

[80] Igor, M., & Škarabot Miha (2008). Self-assembly of nematic colloids. *Soft Matter*, *4*, 195–199.

[81] Itri R., A. (1993). Micellar-shape anisometry near isotropic-liquid-crystal phase transitions. *Physical Review E*, *47*, 2551–2557.

[82] J. Fukuda, & H. Yokoyama (2001). Director configuration and dynamics of a nematic liquid crystal around a two-dimensional spherical particle: Numerical analysis using adaptive grids. *Eur. Phys. J. E*, *4*(3), 389–396.

[83] J. Kedzierski, E., M. Andrzej (2011). Composite method for measurement of splay, twist and bend nematic elastic constants by use of single special in-plane-switched cell. *Molecular Crystals and Liquid Crystals*, *544*(1), 57–68.

[84] J. Mewis, A. (1976). Rheology of concentrated dispersions. *Advances in Colloid and Interface Science*, *6*(3), 173 – 200.

[85] James Christopher J., H. (1981). Electron and optical microscopy study of the lamellar mesophase region of the water/sodium octanoate/decanol ternary system. *J. Chem. Soc., Faraday Trans. 1*, *77*, 2857–2865.

[86] Jean-François, B. (1997). Transient rheology of wormlike micelles. *Langmuir*, *13*.

[87] Jähnig, F., & Schmidt, H. (1972). Hydrodynamics of liquid crystals. *Annals of Physics*, *71*(1), 129 – 166.

[88] John M. Dealy, R., Daniel J. Read (2018). *Structure and Rheology of Molten Polymers From Structure to Flow Behavior and Back Again*. Hanser Publication.

[89] Škarabot, M., Ravnik, M., Zumer, S., Tkalec, U., Poberaj, I., Babic, D., Osterman, N., & Musevic, I. (2008). Interactions of quadrupolar nematic colloids. *Physical review. E, Statistical, nonlinear, and soft matter physics*, *77*, 031705.

[90] Katyan, N., A Wood, T., & Schofield, A. (2020). Defect mediated gel formation in filled lyotropic nematic liquid crystals. *In preparation*.

[91] Katyan, N., A Wood, T., & Schofield, A. (2020). Effect of colloidal charge on microstructure and rheology in micellar nematic solutions. *In preparation*.

[92] Katyan, N., & Annette Wood, T. (2019). Dynamic response of glassy dispersions in a nematic liquid crystal. *Submitted to PRL*.

[93] Kilpatrick Peter K., Khan Saad A., & Tayal Akash and Blackburn John C. (1994). *Rheological Study of Polycrystalline Lyotropic Mesophases in the Cesium Tetradecanoate—Water System*, chap. 15, (pp. 229–238). ACS Publications.

[94] Kotar, J., Vilfan, M., Osterman, N., Babič, D. c. v., Čopič, M., & Poberaj, I. (2006). Interparticle potential and drag coefficient in nematic colloids. *Phys. Rev. Lett.*, *96*, 207801.

[95] Koumakis N, P., Schofield A B (2008). Effects of shear induced crystallization on the rheology and ageing of hard sphere glasses. *Soft Matter*, (pp. 2008–2018).

[96] Kroin T., Palangana A. J., & Figueiredo Neto A. M. (1989). Determination of the bend elastic constant and the anisotropy of diamagnetic susceptibility of lyotropic nematic calamitic liquid crystals. *Phys. Rev. A*, *39*, 5373–5377.

[97] Kuksenok O. V., S., Ruhwandl R. W., & Terentjev E. M. (1996). Director structure around a colloid particle suspended in a nematic liquid crystal. *Phys. Rev. E*, *54*, 5198–5203.

[98] Kuntz Daniel M., & Walker Lynn M. (2008). Nematic phases observed in amphiphilic polyelectrolyte–surfactant aggregate solutions. *Soft Matter*, *4*, 286–293.

[99] L Bohlin, K. (1978). Flow properties of lamellar liquid crystalline lipid-water systems. *Journal of Colloid and Interface Science*, *67*(2), 272 – 283.

[100] Larson, R. G., Winey, K. I., Patel, S. S., Watanabe, H., & Bruinsma, R. (1993). The rheology of layered liquids: lamellar block copolymers and smectic liquid crystals. *Rheologica Acta*, *32*(3), 245–253.

[101] Lautrup, B. (2011). *Physics of Continuous Matter: Exotic and Everyday Phenomena in the Macroscopic World*. CRC Press.

[102] Lazo Israel, L. (2013). Liquid-crystal-enabled electrophoresis of spheres in a nematic medium with negative dielectric anisotropy. *Philosophical Transactions of the Royal Society A: Mathematical, Physical and Engineering Sciences*, *371*(1988), 20120255.

[103] Leon Aurelien, B., & Kellay Hamid (2000). Coupling between flow and structure for a lamellar surfactant phase. *Phys. Rev. Lett.*, *84*, 1335–1338.

[104] Leslie, F. (1979). Theory of flow phenomena in liquid crystals. *Advances in Liquid Crystals*, *4*, 1 – 81.

[105] Leslie, F. M. (1968). Some constitutive equations for liquid crystals. *Archive for Rational Mechanics and Analysis*, *28*(4), 265–283.

[106] Lev B., Osterman N., & Musevic I. (2006). Anisotropic laser trapping in nematic colloidal dispersion. *Eur. Phys. J. E*.

[107] Lev B. I., & Tomchuk P. M. (1999). Interaction of foreign macrodroplets in a nematic liquid crystal and induced supermolecular structures. *Phys. Rev. E*, *59*, 591–602.

[108] Lima, L., & Rey, A. (2004). Linear viscoelasticity of leslie-ericksen liquid crystal polymers. *AIChE Annual Meeting, Conference Proceedings*, (pp. 6577–6583).

[109] Lionberger, R., & Russel, W. (1994). High frequency modulus of hard sphere colloids. *Journal of Rheology*, *38*(6), 1885–1908.

[110] Lodge, A. S. (1964). *Elastic liquids: an introductory vector treatment of finite-strain polymer rheology*. Academy Press.

[111] Lubensky, T. C., Pettey, D., Currier, N., & Stark, H. (1998). Topological defects and interactions in nematic emulsions. *Phys. Rev. E*, *57*, 610–625.

[112] Luckham, P. (1999). Effect of particle size distribution on the rheology of dispersed systems. *Journal of Colloid and Interface Science*, *220*(2), 347 – 356.

[113] M. Carmen, C. (2009). Evolution of the microstructure and rheology of o/w emulsions during the emulsification process. *The canadian journal of chemical engineering*.

[114] M. Hiroyuki, & N Hiizu (1988). On the stability of topologically non-trivial point defects. *Journal of the Physical Society of Japan*, *57*(4), 1281–1286.

[115] M. Rubinstein, R. (2003). *Polymer Physics*. Oxford University Press, New York.

[116] Macosko, C. W. (1994). *Rheology: Principles, Measurements, and Applications*. Wiley-VCH.

[117] Maier Wilhelm , A. (1959). Teine einfache molekular-statistische theorie der nematischen kristallinflüssigen phase. *Zeitschrift für Naturforschung A.*, *14*, 882–899.

[118] Majesté, F. (2010). On the use of the model proposed by Leonov for the explanation of a secondary plateau of the loss modulus in heterogeneous polymer – filler systems with agglomerates. *Rheol Acta*, *49*, 513–527.

[119] Masao Doi, S. (1988). *The Theory of Polymer Dynamics*. Oxford University Press, New York.

[120] Mason, T. (1999). New fundamental concepts in emulsion rheology. *Current Opinion in Colloid and Interface Science*, *4*(3), 231 – 238.

[121] Mason, T. G., Lacasse, M.-D., Grest, G. S., Levine, D., Bibette, J., & Weitz, D. A. (1997). Osmotic pressure and viscoelastic shear moduli of concentrated emulsions. *Phys. Rev. E*, *56*, 3150–3166.

[122] Mason T G, W. (1995). Linear Viscoelasticity of Colloidal Hard Sphere Suspensions near the Glass Transition. *Physical Review Letters*, *75*.

[123] McKay, K., Miller, W., Puig, J., & Franses, E. (1991). Steady and dynamic shear rheology of dispersions of lyotropic liquid crystals. *Journal of Dispersion Science and Technology*, *12*(1), 37–58.

[124] Meeker S. P., T., Poon W. C. K. (2000). Colloid – liquid-crystal composites : An unusual soft solid. *Physical Review E*, *61*, 6083–6086.

[125] Mermin, N. D. (1979). The topological theory of defects in ordered media. *Rev. Mod. Phys.*, *51*, 591–648.

[126] Min, G. (1996). *Principles of Three-Dimensional Imaging in Confocal Microscopes*. World Scientific.

[127] Miner, P. E. (1993). *Chapter 9, Emulsion Rheology Creams and Lotions*. New York publishing house.

[128] MIT (2013). Dynamic Light Scattering : An Introduction in 30 Minutes. *Mit open coursewarre*, (pp. 1–8).

[129] M.J. Rivera-Gastelum, V., O. Robles-Vazquez (1993). Effect of polystyrene block on the rheological and structural properties of high-styrene-content sbrs. *Materials Letters*, *17*(1), 84 – 90.

[130] Montalvo Gemma, R., Valiente Mercedes (1996). Rheological properties of the l phase and the hexagonal, lamellar, and cubic liquid crystals of the ctab/benzyl alcohol/water system. *Langmuir*, *12*(21), 5202–5208.

[131] Muševič, I., Škarabot, M., Babič, D., Osterman, N., Poberaj, I., Nazarenko, V., & Nych, A. (2004). Laser trapping of small colloidal particles in a nematic liquid crystal: Clouds and ghosts. *Phys. Rev. Lett.*, *93*, 187801.

[132] N. Kruszelnicki, W. (2012). Measurement of elastic constants of nematic liquid crystals with use of hybrid in-plane-switched cell. *Opto-Electronics Review*, *20*(3), 255–259.

[133] Németh, Z., Halász, L., Pálinkás, J., Bóta, A., & Horányi, T. (1998). Rheological behaviour of a lamellar liquid crystalline surfactant-water system. *Colloids and Surfaces A: Physicochemical and Engineering Aspects*, *145*, 107–119.

[134] Neumann Bernd, V. (2004). Stability of Various Silicone Oil / Water Emulsion Films as a Function of Surfactant and Salt Concentration. *Langmuir*, *20*, 4336–4344.

[135] Ognysta U., N., & Babič, D. (2008). 2d interactions and binary crystals of dipolar and quadrupolar nematic colloids. *Phys. Rev. Lett.*, *100*, 217803.

[136] Oldham, K. B. (2008). A gouy–chapman–stern model of the double layer at a (metal)/(ionic liquid) interface. *Journal of Electroanalytical Chemistry*, *613*(2), 131 – 138.

[137] Olivier Diat, & Didier Roux (1993). Preparation of monodisperse multilayer vesicles of controlled size and high encapsulation ratio. *J. Phys. II France*, *3*(1), 9–14.

[138] Oseen, C. W. (1933). The theory of liquid crystals. *Trans. Faraday Soc.*, *29*, 883–899.

[139] Osterman Natan, Kotar Jurij, Terentjev Eugene M., & Cicuta Pietro (2010). Relaxation kinetics of stretched disclination lines in a nematic liquid crystal. *Phys. Rev. E*, *81*, 061701.

[140] Ostwald De, W. (1959). Viscometry and plastometry. *J. Gil Color Chern. Assoc*, *6*.

[141] Ostwald Wo., A. (1926). Ueber die viskosität kolloider lösungen im struktur-, laminar- und turbulenzgebiet. *Kolloid-Zeitschrift*, *38*(3), 261–280.

[142] P. Oswald, M. (1988). Rheology an structural defects in a lyotropic lamellar phase. *Journal of Colloid and Interface Science*, *126*(1), 45 – 53.

[143] P. Philippe, F., & Mondain-Monval Olivier (1999). Suspension of spherical particles in nematic solutions of disks and rods. *Phys. Rev. E*, *59*, 4384–4387.

[144] Parkinson, C. (1970). The influence of particle-size distribution on the apparent viscosity of non-newtonian dispersed systems. *Journal of Colloid and Interface Science*, *33*(1), 150 – 160.

[145] Pascal Panizza, Pascal Archambault, & Didier Roux (1995). Effects of shear on the smectic a phase of thermotropic liquid crystals. *J. Phys. II France*, *5*(2), 303–311.

[146] Peláez-Fernández, M., Moncho-Jordá, A., & Callejas-Fernández, J. (2010). Structure of charged colloid-polymer mixtures. *EPL (Europhysics Letters)*, *90*(4), 46005.

[147] Peng .B, A. (2012). Particles by Dispersion Polymerization. *Material physics review*.

[148] Peter, S. (2006). *Soft Glassy Rheology*, (pp. 161–192). Springer.

[149] P.G. de Gennes, J. (1993). *The Physics of Liquid Crystals, 2nd Edition, International Series of Monographs on Physics*. Oxford Science.

[150] Pinto, A. V. A., & Amaral, L. Q. (1990). Bend and splay elastic constants in two nematic lyomesophases with sodium decyl sulfate and potassium laurate. *The Journal of Physical Chemistry*, *94*(7), 3186–3188.

[151] Pishvaei, M., Graillat, C., Cassagnau, P., & McKenna, T. (2006). Modelling the zero shear viscosity of bimodal high solid content latex: Calculation of the maximum packing fraction. *Chemical Engineering Science*, *61*(17), 5768 – 5780.

[152] Pishvaei, M., Graillat, C., McKenna, T., & Cassagnau, P. (2005). Rheological behaviour of polystyrene latex near the maximum packing fraction of particles. *Polymer*, *46*(4), 1235 – 1244.

[153] Poslinski A. J., F. (1994). Rheological behavior of filled polymeric systems ii . the effect of a bimodal size distribution of particulates. *Journal of Rheology*, *32*.

[154] Poslinski A.J., G. (1988). Rheological behavior of filled polymeric systems i. yield stress and shear-thinning effects. *Journal of Rheology*, *32*(7), 703–735.

[155] Poulin P., W., Cabuil V. (1997). Direct measurement of colloidal forces in an anisotropic solvent. *Phys. Rev. Lett.*, *79*, 4862–4865.

[156] Raghavan Srinivasa R., Riley Michael W., Fedkiw Peter S., & Khan Saad A. (1998). Composite polymer electrolytes based on poly(ethylene glycol) and hydrophobic fumed silica, dynamic rheology and microstructure. *Chemistry of Materials*, *10*(1), 244–251.

[157] Raghunathan, V. A., Richetti, P., & Roux, D. (1996). Dispersion of latex particles in a nematic solution. 2. phase diagram and elastic properties. *Langmuir*, *12*(16), 3789–3792.

[158] Ramaswamy, S., Nityananda, R., Raghunathan, V. A., & Prost, J. (1996). Power-law forces between particles in a nematic. *Molecular Crystals and Liquid Crystals Science and Technology. Section A. Molecular Crystals and Liquid Crystals*, *288*(1), 175–180.

[159] Ramos, L., Zapotocky, M., Lubensky, T. C., & Weitz, D. A. (2002). Rheology of defect networks in cholesteric liquid crystals. *Phys. Rev. E*, *66*, 031711.

[160] Raszewski, Z., Debrowski, R., Morawiak, P., & Ogrodnik, K. (2010). Electrically tunable liquid crystal filters. *Molecular Crystals and Liquid Crystals*, *525*(1), 112–127.

[161] Ravnik, M. (2011). Colloidal structures in confined nematic liquid crystals. *Liquid Crystals Today*, *20*(3), 77–84.

[162] Reiner, M. (1949). *Deformation and Flow: An Elementary Introduction to Theoretical Rheology*. H.K. Lewis and Co (1949).

[163] Riley, K. F., Hobson, M. P., & Bence, S. J. (2006). *Series solutions of ordinary differential equations*, (p. 531–553). Cambridge University Press, 3 ed.

[164] Robert J., H. (1988). *Zeta Potential in Colloid Science: Principles and Applications*. Academic Press.

[165] Roscoe, R. (2002). The viscosity of suspensions of rigid sphere. *British Journal of Applied Physics*, *3*, 267.

[166] Rosevear, F. B. (1954). The microscopy of the liquid crystalline neat and middle phases of soaps and synthetic detergents. *Journal of the American Oil Chemists' Society*, *31*(12), 628–639.

[167] Ruhwandl R. W., T. (1997). Long-range forces and aggregation of colloid particles in a nematic liquid crystal. *Phys. Rev. E*, *55*, 2958–2961.

[168] Rutgers, I. R. (1962). Relative viscosity of suspensions of rigid spheres in newtonian liquids. *Rheologica Acta*, *2*(3), 202–210.

[169] Ruth A. Yost, J. (1992). Microstructure of whey protein isolate gels containing emulsified butterfat droplets. *Journal of food Science*, *57*, 892–897.

[170] S. Hofmann, H., A. Rauscher (1991). Shear induced micellar structures. *Springer*, (pp. 153–164).

[171] Saiki Yasushi, H., Prestidge Clive A. (2007). Effects of droplet deformability on emulsion rheology. *Colloids and Surfaces A: Physicochemical and Engineering Aspects*, *299*, 65–72.

[172] Saini, D., Shenoy, A., & Nadkarni, V. (1986). Melt rheology of highly loaded ferrite-filled polymer composites. *Polymer Composites*, *7*, 193 – 200.

[173] S.Chandrasekhar (1992). *Liquid Crystal*. Cambridge, U.K.: Cambridge University Press.

[174] Shenoy, A. (1999). *Rheology of Filled Polymer Systems*. Kluwer Academic Publishers.

[175] Sherman, P. (1963). *Rheology of emulsions.*. Oxford: London: New York: Paris: Pergamon Press.

[176] Shikata, T., & Pearson, D. S. (1994). Viscoelastic behavior of concentrated spherical suspensions. *Journal of Rheology*, *38*(3), 601–616.

[177] Siddharth, K., & Prachi, T. (2016). Rheology of colloidal particles in lyotropic hexagonal liquid crystals: the role of particle loading, shape, and phase transition kinetics. *Rheologica Acta*, *55*(1), 23–36.

[178] S.J Candau, & R Oda (2001). Linear viscoelasticity of salt-free wormlike micellar solutions. *Colloids and Surfaces A: Physicochemical and Engineering Aspects*, *183-185*, 5 – 14.

[179] Skarabot M., Tkalec U., & Musevic I. (2007). Transport and crystallization of colloidal particles in a thin nematic cell. *Eur. Phys. J. E*, *24*(1), 99–107.

[180] Smalyukh, I. I., Lavrentovich, O. D., Kuzmin, A. N., Kachynski, A. V., & Prasad, P. N. (2005). Elasticity-mediated self-organization and colloidal interactions of solid spheres with tangential anchoring in a nematic liquid crystal. *Phys. Rev. Lett.*, *95*, 157801.

[181] Spenley N. A., Cates M. E., & McLeish T. C. B. (1993). Nonlinear rheology of wormlike micelles. *Phys. Rev. Lett.*, *71*, 939–942.

[182] Stickel Jonathan J, & Powell Robert L (2005). Fluid mechanics and rheology of dense suspensions. *Annu. Rev. Fluid Mech*, *37*, 129–149.

[183] Sun, Z.-H. (2013). Congruences concerning legendre polynomials ii. *Journal of Number Theory*, *133*, 1950 – 1976.

[184] Tadros, T. F. (2013). *Emulsion Formation, Stability, and Rheology*. Wiley.

[185] Thiele Thomas , & Schmidt Claudia (2001). Rheology and nuclear magnetic resonance measurements under shear of sodium dodecyl sulfate/decanol/water nematics. *Journal of Rheology*, *45*(1), 29–48.

[186] Torza S, C. (1972). Particle Motions in Sheared Suspensions xxvI! Transient and Steady Deformation and Burst of Liquid Drops. *Journal of Colloid Interface Science.*, *38*.

[187] Toyoko Imae, S., Ritsu Kamiya (1985). Formation of spherical and rod-like micelles of cetyltrimethylammonium bromide in aqueous nabr solutions. *Journal of Colloid and Interface Science*, *108*(1), 215 – 225.

[188] Trappe, V., Prasad, V., Cipelletti, L., Segre, P. N., & Weitz, D. A. (2001). Jamming phase diagram for attractive particles. *Nature.*, *411*(6839), 772–775.

[189] Treloar, L. R. (1940). Elastic behavior and plastic flow in rubber . *Transaction of the Faraday Society*, *67*, 538–549.

[190] Tsai S C, P., Botts D (1994). Effects of particle properties on the rheology of concentrated noncolloidal suspensions. *Journal of Rheology*, *36*(1992).

[191] V. A. Raghunathan, A. (1996). Colloidal dispersions in a liquid crystalline medium. *Molecular Crystals and Liquid Crystals Science and Technology. Section A. Molecular Crystals and Liquid Crystals*, *288*(1), 181–187.

[192] Van, M. (1994). Glass transition in colloidal hard spheres: Measurement and mode-coupling-theory analysis of the coherent intermediate scattering function . *Physical Review E*, *49*(5), 4206–4220.

[193] Volovik, G., & Lavrentovich, O. (1983). Topological dynamics of defects: Boojums in nematic drops. *J. Exp. Theor. Phys.*, *85*.

[194] Wagner, N. J., Krause, R., Rennie, A. R., D'Aguanno, B., & Goodwin, J. (1991). The microstructure of polydisperse, charged colloidal suspensions by light and neutron scattering. *The Journal of Chemical Physics*, *95*(1), 494–508.

[195] Walker, L. M. (2001). Rheology and structure of worm-like micelles.

[196] Welss, N. O. (1985). A review of: "computational methods for fluid flow". *Geophysical & Astrophysical Fluid Dynamics*, *31*(3-4), 346–348.

[197] Wilson, T. (1994). *Confocal Microscopy*, (pp. 219–232). Boston, MA: Springer US.

[198] Wolfgang, O. (1925). Ueber die geschwindigkeitsfunktion der viskosität disperser systeme. i. *Kolloid-Zeitschrift*, *36*(2), 99–117.

[199] Won You-Yeon, D., & Bates Frank S. (1999). Giant wormlike rubber micelles. *Science*, *283*(5404), 960–963.

[200] Wood, T. A., Lintuvuori, J. S., Schofield, A. B., Marenduzzo, D., & Poon, W. C. K. (2011). A self-quenched defect glass in a colloid-nematic liquid crystal composite. *Science*, *334*(6052), 79–83.

[201] Woolston, P., & van Duijneveldt, J. S. (2015). Isotropic–nematic phase transition in aqueous sepiolite suspensions. *Journal of Colloid and Interface Science*, *437*, 65 – 70.

[202] Woolston, P., & van Duijneveldt, J. S. (2015). Three-phase coexistence in colloidal rod–plate mixtures. *Langmuir*, *31*(34), 9290–9295.

[203] Yang, J. (2002). Viscoelastic wormlike micelles and their applications. *Current Opinion in Colloid and Interface Science*, *7*(5), 276 – 281.

[204] Zdeněk, M. (1999). *Principles of Continuum Mechanics*. Birkhäuser.

[205] Zipfel Johannes, R. (1999). Influence of shear on lyotropic lamellar phases with different membrane defects. *The Journal of Physical Chemistry B*, *103*(15), 2841–2849.

[206] Zocher, H. (1933). The effect of a magnetic field on the nematic state. *Trans. Faraday Soc.*, *29*, 945–957.